Nanofluids for Solar Absorption Refrigeration Systems

Aimen Rashad Noor Zeiny

Submitted in accordance with the requirements for the degree of

Doctor of Philosophy

The University of Leeds

School of Chemical and Process Engineering

October 2018

The candidate confirms that the work submitted is his own, except where work which has formed part of jointly-authored publications has been included. The contribution of the candidate and the other authors to this work has been explicitly indicated below. The candidate confirms that appropriate credit has been given within the thesis where reference has been made to the work of others.

This copy has been supplied on the understanding that it is copyright material and that no quotation from the thesis may be published without proper acknowledgement.

The right of Aimen Rashad Noor Zeiny to be identified as Author of this work has been asserted by him in accordance with the Copyright, Designs and Patents Act 1988.

© 2018 The University of Leeds and Aimen Rashad Noor Zeiny.

List of Publications

- **Aimen Zeiny**, Haichuan Jin, Lizhan Bai, Guiping Lin, Dongsheng Wen, “A comparative study of direct absorption nanofluids for solar thermal applications”, Solar Energy 161 (2018) 74–82.

  The candidate designed and performed the experiments and led the article drafting. Haichuan Jin, Lizhan Bai and Guiping Lin helped with the discussion. Dongsheng Wen supervised the work and gave suggestions for interpreting the results and finalising the article.

- **Aimen Zeiny**, Haichuan Jin, Guiping Lin, Pengxiang Song, Dongsheng Wen, “Solar evaporation via nanofluids: A comparative study”, Renewable Energy 122 (2018) 443-454.

  The candidate designed and performed the experiments and led the article drafting. Haichuan Jin, Guiping Lin and Pengxiang Song helped with the discussion. Dongsheng Wen supervised the work and gave suggestions for interpreting the results and finalising the article.

Acknowledgements

First and foremost, my profound and sincere gratitude goes to my supervisor, Prof. Dongsheng Wen, the humane, humble, wise and knowledgeable man. Thank you very much for your endless guidance and moral support. Your continuous encouragement in forging the research direction has led to achieving its fruits. Also, I would like to thank my co-supervisors, Dr Alan Burns and Dr Ali Hassanpour for their support during the research journey.

I am deeply grateful to my sponsor, the University of Kufa/Iraqi Ministry of Higher Education and Scientific Research for providing me with this scholarship, making me able to study in the University of Leeds, the very prestigious university.

I also would like to thank everyone who helped and support me during the PhD journey especially Dr Lizhan Bai, Dr Susanne Patel, Dr Ehsan Nourafkan, and Dr Ghulam Raza, and special thanks to my colleagues; Zhongliang Hu, Haichuan Jin, and Muhammad Amjad. Discussions and debates with you, guys, have broadened my horizon, and joking and laughing have built sweet memories that never ever can be forgotten.

Above all, my eternal gratitude goes to my parents. Thank you very much for your endless support and encouragement. Also, a big thank you to my wife for her understanding and patience during this journey. Finally, I have to say thank you to my lovely son, Fadl, and sweet daughter, Tabarak, for filling my life with happiness.

Aimen

July 2018

Abstract

Vapour absorption refrigeration systems (VARSs), which utilise eco-friendly refrigerants (water), can work based on low-grade thermal energy, such as the solar energy. Using solar energy can relief the high electrical load on many national grids around the world as the peak load almost coincides with the high solar intensities time during summer. However, high initial cost, big specific size and low coefficient of performance are the main challenges that face the VARSs. Therefore, improving the efficiencies of the components of a solar refrigeration system, such as the solar collector, generator and absorber, is crucial to improve the overall efficiency of that system and to reduce its size and the cost.

To improve the efficiency of a solar VARS, nanofluids are proposed in this work through direct and indirect ways. The direct way is seeding functional nanoparticles in the aqueous solution of a VARS. The expectations are that refrigerant (steam) can be generated efficiently via direct volumetric absorption of the solar energy at the generator and can be absorbed effectively via the Brownian motion of the nanoparticles at the absorber. While, the indirect way is; using aqueous nanofluids in direct solar collectors can harvest the solar energy in an efficient way, saving it in a storage tank. This stored energy is used later to generate the steam in the generator of the VARS.

This work aims to investigate fundamentally the applicability of utilising nanofluids for solar absorption refrigeration systems through performing three main studies:

Firstly, a comparative study of gold, copper oxide, gold and copper oxide hybrids, and carbon black nanofluids has been conducted to investigate the photo-thermal conversion efficiency. The results have shown that gold nanofluids are not feasible for solar application due to the high cost and low performance comparing to the carbon black nanofluids. Moreover, this study has demonstrated that blending different nanofluids of different narrow spectral absorption peaks can really broaden the effective spectral absorption

peak but reduces its value due to the accompanied dilution of the blended nanofluids as the overall volume unavoidably increases.

Secondly, a comparative study of solar steam generation among gold nanofluids, carbon black nanofluids and a thin carbon-based porous medium has been conducted. The results have also shown the infeasibility of using gold nanofluids comparing with the carbon black nanofluids due to the high cost and low absorptivity. Furthermore, this study has shown the superiority of using a thin, carbon-based porous medium in producing steam due to its capability to absorb most the solar energy in micro-sized thickness. While, very high nanoparticles concentration is required to trap and absorb the solar energy in such a thin layer, which consequently leads to an instability, high viscosity and high-cost issues.

Finally, a study of the steam absorption by and generation from aqueous lithium bromide solutions seeded with carbon black and carbon nanotubes has been conducted. The results have demonstrated that a very low concentration of carbon black nanoparticles can reduce the transparency of the solutions to zero. However, seeding nanoparticles in the solutions has shown the negligible effect on the steam absorption rate, which demonstrated that the Brownian motion of the nanoparticles has a negligible effect on the steam absorption.

Although the experiments conducted in this project showed negligible enhancement in the steam absorption, obvious enhancements in the photo-thermal conversion efficiency and steam generation were achieved by using nanofluids. Recommendations are suggested for future work to study other affecting aspects of seeding nanoparticles in aqueous solutions.

Keywords: Nanoparticles, Nanofluids, Solar Energy, Absorption Refrigeration.

Table of Contents

Chapter 1 INTRODUCTION ..... - 1 -

1.1 Refrigeration ..... - 1 -

1.1.1 Vapour-compression refrigeration systems (VCRSs) ..... - 1 -

1.1.2 Vapour-absorption refrigeration systems (VARSs) ..... - 2 -

1.1.3 Water-lithium bromide against ammonia-water based VARSs ..... - 4 -

1.1.4 Impact of refrigeration systems on energy consumption and environment ..... - 5 -

1.2 Global Concerns ..... - 7 -

1.3 Research Motivation ..... - 9 -

1.4 Research Objectives ..... - 17 -

1.5 Thesis Outline ..... - 18 -

Chapter 2 LITERATURE REVIEW ..... - 20 -

2.1 Solar Refrigeration ..... - 20 -

2.2 Efforts to Develop New VARSs ..... - 26 -

2.3 Direct Absorption Solar Collectors (DASCs) ..... - 39 -

2.4 Solar-Assisted Steam Generation ..... - 44 -

2.5 Chapter Summary ..... - 54 -

Chapter 3 PHOTO-THERMAL CONVERSION EFFICIENCY OF DIFFERENT NANOFLUIDS ..... - 57 -

3.1 Introduction ..... - 57 -

3.2 Theoretical Part ..... - 58 -

3.3 Experimental Part ..... - 62 -

3.3.1 Gold nanofluids preparation ..... - 62 -

3.3.2 Carbon black and copper oxide nanofluids preparation ..... - 62 -

3.3.3 Nanofluids characterisation ..... - 70 -

3.3.4 Photo-thermal conversion ..... - 75 -

3.3.5 Results and discussion ..... - 79 -

3.4 Chapter Summary ..... - 92 -

Chapter 4 NANOPARTICLE-ASSISTED SOLAR EVAPORATION ..... - 93 -

4.1 Introduction ..... - 93 -

4.2 Nanofluids Preparation and Characterisations ..... - 95 -

4.3 Solar Evaporation Experimental Setup ..... - 95 -

4.4 Results and Discussion ..... - 97 -

4.4.1 Experiments with 35 ml samples ..... - 97 -
4.4.2 Experiments with 4 ml samples ..... - 106 -
4.4.3 Experiments with a porous medium ..... - 114 -
4.5 Chapter Summary ..... - 120 -
Chapter 5 H_2O-LiBr NANOSOLUTIONS ..... - 122 -
5.1 Introduction ..... - 122 -
5.2 Nanosolutions Preparation and Characterisations ..... - 123 -
5.3 Steam Absorption and Generation Experimental Setup ..... - 125 -
5.4 Results and Discussions ..... - 127 -
5.4.1 Transmittance ..... - 127 -
5.4.2 Viscosity ..... - 128 -
5.4.3 Thermal conductivity ..... - 129 -
5.4.4 Steam absorption ..... - 131 -
5.4.5 Steam generation ..... - 139 -
5.5 Chapter Summary ..... - 142 -
Chapter 6 CONCLUSION AND FUTURE WORK ..... - 144 -
6.1 Conclusions ..... - 144 -
6.2 Future Work ..... - 150 -
List of References ..... - 153 -

List of Tables

Table 4.1 Temperature distribution within different concentrations of gold nanofluids. The samples are subjected to 10 kW/m^2 radiation for the first 15 min (heating-up process), after that samples go through a cooling-down process (No radiation)…. - 99 -

Table 4.2 The effect of the incident light intensity on the temperature distribution during heating-up (symbols for the experimental data and the lines are trend lines) and cooling-down of a nanofluid at different time steps. ..... - 105 -

Table 4.3 Properties of the GDL type ELAT. ..... - 115 -

Table 5.1 Performance of Nanosolutions in Falling Film Experiments .. - 132 -

List of Figures

Figure 1.1 Schematic diagram of a VCRS. ..... - 2 -

Figure 1.2 Schematic diagram of a VARS. ..... - 3 -

Figure 1.3 Estimated global share of net electricity generation by different energy sources [11]. ..... - 6 -

Figure 1.4 Global Greenhouse Gases Emissions [18]. ..... - 9 -

Figure 1.5 Estimated availability of different energy resources compared to the estimated annual energy consumption by humans [19]. ..... - 11 -

Figure 1.6 The global solar flux on the earth surface [19]. ..... - 12 -

Figure 1.7 Conventional solar-driven VARS for air conditioning application [21]. ..... - 12 -

Figure 1.8 A cut in H_2O-LiBr VARS [22]. ..... - 13 -

Figure 1.9 In direct system, where the nanofluid does not participate in the refrigeration cycle. ..... - 15 -

Figure 1.10 Direct system, where the nanoparticles in H_2O-LiBr solution. ..... - 16 -

Figure 2.1 Performance and cost of various solar refrigeration systems [33]. ..... - 24 -

Figure 2.2 Representative temperature and concentration profiles on a section of a falling film of H_2O-LiBr solution on a horizontal pipe. [38]. ..... - 25 -

Figure 2.3 Pictures of the surface of an aqueous LiBr solution: (a) without surfactant and (b) with surfactant at 400 ppm [56]**. ..... - 31 -**

Figure 2.4 Thermograms of the moving surface layer of the aqueous LiBr solution with surfactant at (a) 1 s, (b) 10 s, (c) 60 s and (d) 120 s [56]. ..... - 31 -

Figure 2.5 Effective absorption ratio with a falling film nanosolutions [60]. ..... - 35 -

Figure 2.6 Illustration of the falling film modes (dripping, jet-column and sheet modes) [63]. ..... - 36 -

Figure 2.7 The spectral extinction coefficient. (A) 2 nm gold nanofluids. The brownish-red colour appears in the photograph is due to the light absorption across the entire visible spectrum. (B) 1 μm silica colloid. The colour appears white since the visible light spectrum is scattered from the particles back toward the observer. [65]. ..... - 39 -

Figure 2.8 Schematic diagram for a suggested mechanism of solar steam generation via nanoparticles [91]. ..... - 46 -

Figure 2.9 Minimum irradiance to generate vapour bubbles in different nanofluids at different concentrations [93] ..... - 48 -

Figure 2.10 Temperature difference between a Au nanoparticle and surrounding water. The nanoparticle is in the centre of the cube and subjected to 220 Suns radiation [88]. ..... - 49 -

Figure 2.11 Condensation of solar-generated steam [98]..... - 51 -

Figure 3.1 Transparency of de-ionised water and 50 wt.% aqueous lithium bromide solution. ..... - 58 -

Figure 3.2 Light attenuation in absorbing medium. ..... - 59 -

Figure 3.3 Percentage of the absorbed light intensity as a function of nanofluid's depth at different extinction coefficients..... - 61 -

Figure 3.4 The rate change of the absorbed light intensity as a function of nanofluid's depth at different incident light intensities. ..... - 61 -

Figure 3.5 Cu particles separation after 15 min even high sonication energy density (1.5313 x 10^9 J/m^3) was consumed. ..... - 63 -

Figure 3.6 Tween®80 structure. ..... - 65 -

Figure 3.7 Aqueous CB nanofluid after mixing..... - 66 -

Figure 3.8 Particles' average size as a function of sonication energy per unit volume of the nanofluid..... - 67 -

Figure 3.9 Aqueous suspensions of 100 mg/l CB at different GA concentrations. #1, #2, #3 and #4 are 1.5%, 1%, 0.5% and 0.1% GA respectively. (A) just after preparation, (B) a week after and (C) 4 weeks after preparation. ..... - 69 -

Figure 3.10 A photo of the nanofluids: Au nanofluid on right, Cu nanofluid in middle, and CB nanofluid on left. ..... - 71 -

Figure 3.11 Size distribution of Au nanoparticles by (A) intensity and (B) number. ..... - 72 -

Figure 3.12 Size distribution of Cu nanoparticles by (A) intensity and (B) number. ..... - 73 -

Figure 3.13 Size distribution of CB nanoparticles by (A) intensity and (B) number..... - 73 -

Figure 3.14 TEM graphs of (A) Au, (B) Cu and (C) CB nanofluids.... - 74 -

Figure 3.15 Spectral absorbance of different concentrations of nanofluids. The insets show the linear relationship between absorbance and concentration. (A) Au, (B) Cu, (C) CB nanofluids. ..... - 76 -

Figure 3.16 Experimental setup for the photo-thermal conversion tests..... - 77 -

Figure 3.17 Average temperature rise of a water sample using 5 thermocouples at different positions on the base of the Petri dish..... - 78 -

Figure 3.18 Repeatability test of the photo-thermal conversion. ..... - 79 -

Figure 3.19 Temperature rise and photo-thermal conversion efficiency variation with time (A) for Au nanofluids and water, (B) for Cu nanofluids and water, and (C) CB nanofluids and water (solid lines represent PTEs and symbol-lines represent temperature rise). ..... - 81 -

Figure 3.20 Temperature rise of a nanofluid as a function of its concentration at different time steps. The symbols represent the experimental data and lines represent the trend lines. The inset shows the photo-thermal conversion efficiency as a function of the concentration of (A) Au nanofluids, (B) Cu nanofluids, (C) CB nanofluids. ..... - 82 -

Figure 3.21 Photo-thermal conversion efficiency enhancement for: (A) Au, (B) Cu nanofluids. ..... - 83 -

Figure 3.22 The absorbance spectrum of Au, Cu and a blend of 1:1 nanofluids. ..... - 85 -

Figure 3.23 Temperature rise variation with time of Au and Cu nanofluids and their hybrids. ..... - 86 -

Figure 3.24 Photo-thermal conversion efficiency enhancement of CB nanofluids. ..... - 87 -

Figure 3.25 Specific absorption rate and cost of a unit heat per unit time for: (A) Au, (B) Cu, (C) CB nanofluids. ..... - 89 -

Figure 3.26 Spectral irradiance of the solar energy at the sea level (AM 1.5). ..... - 90 -

Figure 3.27 A comparison between the maximum enhancement (Theoretical) and PTE enhancement (experimental) for: (A) Au, (B) Cu, and (C) CB nanofluids. ..... - 91 -

Figure 4.1 Solar evaporation experimental setup. ..... - 96 -

Figure 4.2 Mass change with time of different concentrations of gold nanofluids subjected to 10 kW/m^2. ..... - 98 -

Figure 4.3 Percentage of the absorbed energy as a function of the light path at different extinction coefficients. Light path is 40 mm (A) and 5 mm (B). ..... - 103 -

Figure 4.4 The rate change of the absorbed energy with respect to nanofluid's depth at different incident light intensities. ..... - 104 -

Figure 4.5 Temperature and mass change with time for (A) gold and (B) carbon black nanofluids subjected to 10 kW/m^2 irradiance. - 106 -

Figure 4.6 Evaporation rates for gold and carbon black nanofluids as a function of time (upper row) and temperature (lower row). Heating-up process is under 10 kW/m^2 irradiance. ..... - 108 -

Figure 4.7 The dynamic cost of producing 1 g/s vapour using (A) gold and (B) carbon black nanofluids subjected to 10 kW/m^2. - 110 -

Figure 4.8 Total latent and sensible heat for (A) gold and (B) carbon black nanofluids subjected to 10 kW/m^2 irradiance. ..... - 111 -

Figure 4.9 The ratio of latent to sensible heat of Au and CB nanofluids. Time= 600 s and I=10 kW/m^2. ..... - 112 -

Figure 4.10 Evaporation efficiency as a function of time at different nanofluid's concentration for (A) gold and (B) carbon black nanofluids subjected to 10 kW/m^2 irradiance. ..... - 113 -

Figure 4.11 Photo-thermal conversion efficiency as a function of time at different nanofluid's concentration for (A) gold and (B) carbon black nanofluids subjected to 10 kW/m^2 irradiance. ... - 114 -

Figure 4.12 Spectral absorbance of the GDL. ..... - 116 -

Figure 4.13 The GDL, hydrophilic tissue and PIB system. (A) a top view and (B) a bottom view. ..... - 117 -

Figure 4.14 A comparison of steam generation via gold nanofluids, GDL and GDL+PIB..... - 118 -

Figure 4.15 Solar evaporation via GDL+PIB under different light intensities. ..... - 119 -

Figure 4.16 Solar evaporation rate and efficiency of GDL+PIB under different incident solar intensities. ..... - 119 -

Figure 5.1 Steam absorption experimental setup..... - 126 -

Figure 5.2 A comparison of the spectral transmittance of aqueous lithium bromide solutions without and with different nanoparticles. ..... - 127 -

Figure 5.3: Viscosity of (A) different concentrations of aqueous lithium bromide solutions, (B) of different concentrations of GA, (C) of different concentrations of CB and (D) of different concentrations of MWCNTs to 60 wt.% aqueous lithium bromide solution. ..... - 129 -

Figure 5.4 Thermal conductivity of: (A) different concentrations of aqueous lithium bromide solution, (B) different concentrations of GA, (C) different concentrations of CB and (D) different concentrations of MWCNTs in 60 wt.% aqueous lithium bromide solution. ..... - 130 -

Figure 5.5 Steam absorption of different additives to 60 wt.% aqueous lithium bromide solution. (A) Tween® 80, (B) Gum-Arab, (C) Carbon black and (D) Multi-wall carbon nanotubes. - 131 -

Figure 5.6 Schematic of homogeneously distributed particles in a cube of one litre. ..... - 136 -

Figure 5.7 The inter-distance between two adjacent particles as a function of (A) the particle's diameter at constant colloid concentration and (B) as a function of the colloid concentration at constant particle's diameter. ..... - 138 -

Figure 5.8 Temperature and mass change of nanosolutions at 0 wt.% and 0.005 wt.% CB. Light intensity is 850 W/m^2. .....- 139 -

Figure 5.9 Photo-thermal conversion of different CB concentrations in 50 wt.% aqueous lithium bromide solution under 10 Suns irradiance. (A) Temperature rise of the nanosolutions, (B) mass reduction of the nanosolutions and (C) steam generation rate as function of time. .....- 141 -

Figure 6.1 Nanoparticles' effect on the size of LiBr crytals.....- 152 -

Abbreviations

Abbreviation	Full meaning
2E1H	2-ethyl-1hexanol
A	Absorber
AAS	Atomic Absorption Spectrometer
BRIC	Brazil, Russia, India and China
CB	Carbon Black
CFCs	Chlorofluorocarbons
CNT	Carbon Nano-Tubes
COP	Coefficient of Performance
DI water	De-ionised water
DLS	Dynamic Light Scattering
G	Generator
GA	Gum Arab
GCC	Gulf Cooperation Council
GDL	Gas Diffusion Layer
GHG	Greenhouse Gas
H_2O-LiBr	Water-Lithium Bromide Solution
HCFCs	Hydro-Chlorofluorocarbons
HFCs	Hydro-fluorocarbons
LiBr	Lithium Bromide
MHX	2-methyl-1-hexanol
MWCNTs	Multi-Wall Carbon Nano-Tubes
NH_3-H_2O	Ammonia-Water pair
P	Pump
PHPP	3-phenyl-1-propanol
PIB	Polystyrene Insulation Board
ppm	Part per million

PTE	Photo-Thermal Efficiency
SAR	Specific Absorption Rate (kW/g)
SHX	Solution Heat Exchanger
TEM	Transmission Electron Microscope
TMHX	3,5,5-trimethyl-1-hexanol
TR	Ton of Refrigeration ≈ 3.5 kW
VARSs	Vapour-Absorption Refrigeration Systems
VCRSs	Vapour-Compression Refrigeration Systems

Symbol	Full meaning
$\Delta \boldsymbol{T}$	Temperature difference (K)
$\Delta \boldsymbol{t}$	Time step (s)
k	Thermal conductivity (W/m K)
$\dot{m}$	Evaporation rate (g/s)
$\boldsymbol{A}$	Area (m^2)
$\boldsymbol{C}$	Sample's concentration (mg/l)
$\boldsymbol{I}$	Radiation intensity (W/m^2)
$\boldsymbol{V}$	Sample's volume (ml)
$\boldsymbol{c}$	Specific heat capacity (J/kg K)
$\boldsymbol{m}$	Mass (kg)
$\boldsymbol{\alpha}$	Extinction coefficient
$\boldsymbol{\lambda}$	Wavelength (nm)

Subscript	Full meaning
$\boldsymbol{abs}$	Absorbed
$\boldsymbol{nf}$	Nanofluid
$\boldsymbol{np}$	Nanoparticle
$\boldsymbol{o}$	Origin
$\boldsymbol{w}$	Water

Chapter 1

INTRODUCTION

1.1 Refrigeration

Refrigeration technologies play an important role in the modern life. They are commonly used in chilling, freezing and air conditioning applications. They are crucial to many industry applications such as food and pharmaceutical and they are important to produce comfortable environments for people in residential, shopping and working places. According to the Oxford and Cambridge dictionaries, refrigeration is the process of keeping something cold. In engineering, refrigeration is the process of transferring heat from low-temperature to high-temperature spaces to produce cooling action [1]. This heat transfer needs a working fluid (refrigerant) and a thermodynamic input in a form of mechanical work as in vapour-compression refrigeration systems (VCRSs), or in a form of heat as in vapour-absorption refrigeration systems (VARSs) [2], [3]. A brief description of both VCRSs and VARSs is presented in the following sub-sections.

1.1.1 Vapour-compression refrigeration systems (VCRSs)

Figure 1.1 shows a schematic diagram of a typical vapour-compression refrigeration system. This system mainly consists of an evaporator where the refrigerant evaporates taking heat from the surrounding and producing the cooling effect, a compressor which compresses the refrigerant vapour from

the evaporator pressure to the condenser pressure, a condenser where the refrigerant vapour condenses and cools down by rejecting heat to a surrounding, and an expansion valve where the refrigerant condensate expands to the evaporator pressure [1]. This type of refrigeration systems is a high electrical power demanding system. Most of the electrical power is consumed by the compressor.

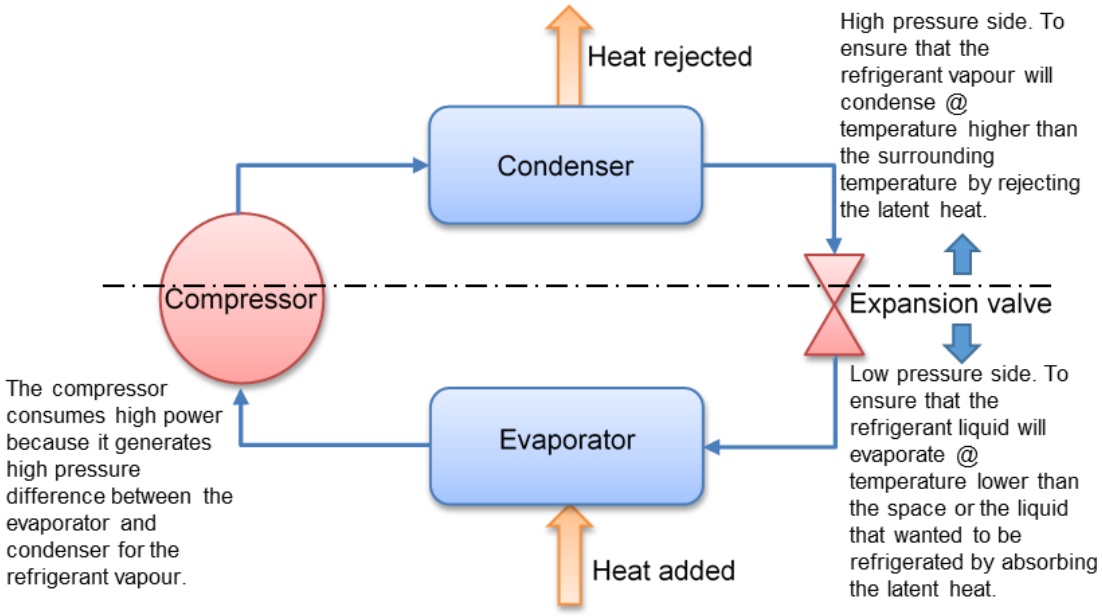

Figure 1.1 Schematic diagram of a VCRS.

1.1.2 Vapour-absorption refrigeration systems (VARSs)

Figure 1.2 shows a schematic diagram of a typical VARS. This system is similar to the VCRS except the compression process. Where in VCRS, a compressor is used to compress the refrigerant vapour from the evaporator pressure to the condenser pressure, while in the VARS, a complex of an absorber, a generator, a heat exchanger and a low power consuming pump is used instead of the compressor, where a solution system of an absorbent and a refrigerant is circulated in the complex. The absorbent is the lithium

bromide (LiBr) in water-lithium bromide (H_2O-LiBr) based VARSs and water (H_2O) in the ammonia-water (NH_3-H_2O) based VARSs, while the refrigerants are H_2O and NH_3 respectively.

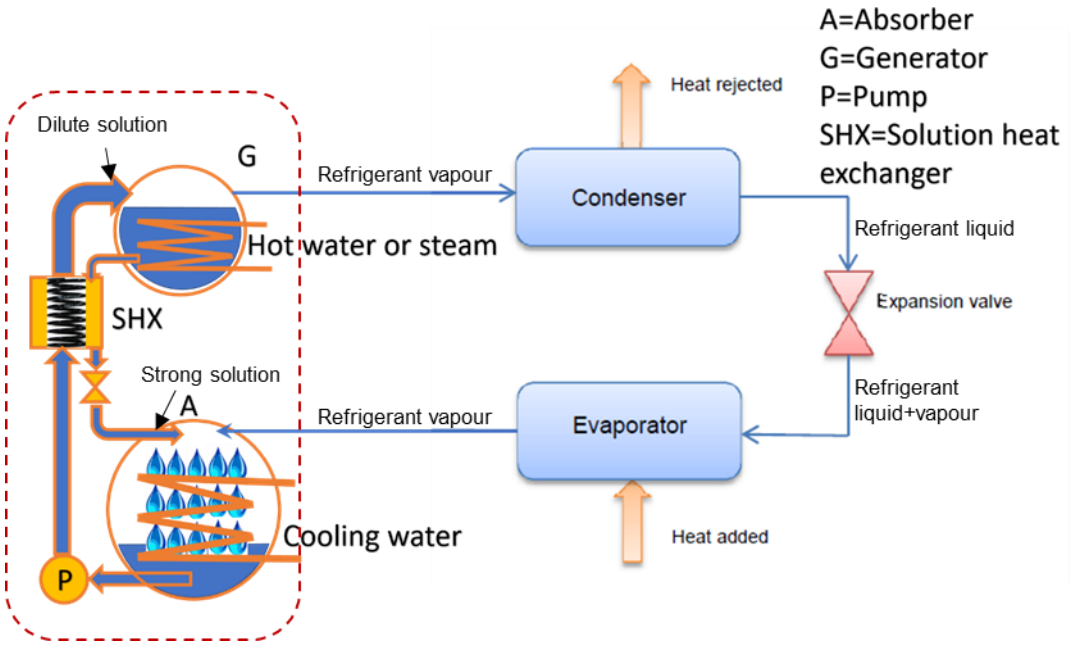

Figure 1.2 Schematic diagram of a VARS.

In the absorber (A), the refrigerant vapour, which is generated in the evaporator, is absorbed by a strong solution (rich in absorbent) coming from the generator (G) through the solution heat exchanger (SHX) and sprayed on a cooling coil to dissipate the heat of absorption to a surrounding. This process is important because the refrigerant vapour is converted to liquid before the compression process; therefore, a low power consumption pump (P) can be used (sometimes, a bubble pump can be used instead of the conventional electro-mechanical pump) to pump the diluted solution from the absorber to the generator passing through the SHX. In the generator (G), the refrigerant vapour is released thermally via boiling the diluted solution in the pool type

generator or via evaporation in the falling film type generator. The required heat is supplied through a hot water or steam. Low-grade heat from exhaust gases or solar energy can be used in this process instead of high-grade heat from electrical power or fuel combustion. [1]–[3].

1.1.3 Water-lithium bromide against ammonia-water based VARSs

H_2O-LiBr based VARSs have advantages over NH_3-H_2O based VARSs such as: the H_2O-LiBr binary solution is non-toxic while NH_3 is very toxic. LiBr is non-volatile substance; therefore, there is no need for a rectifier. While it is common to have water vapour mixed with the released refrigerant (NH_3) after the generator. Hence, an additional component, namely a rectifier, is required to minimize the water vapour concentration in the released NH_3 at the inlet of the condenser. This additional component increases the system complexity and cost and reduces the COP comparing to the H_2O-LiBr based VARSs [4], [5].

However, H_2O-LiBr based VARSs have some disadvantages such as they cannot be used in applications requiring temperatures below 0 ^oC. Therefore, they are preferably to be used for air-conditioning systems. Also, crystallization is a coherent phenomenon if the concentration of the LiBr becomes relatively high as the crystallization is directly proportional to concentration and inversely to temperature.

VARSs based on H_2O-LiBr working in the temperature range of 70-90 ^oC of the generator produce coefficient of performance (COP) of 0.6-0.8. Such low generation temperature can be easily supplied by flat plate solar collectors or evacuated tube solar collectors [4]. Using thermal solar collectors to drive VARSs is better than using photovoltaic cells because the former have high efficiencies (20% - 80%), while the latter have low efficiencies (15% - 18%) [4].

1.1.4 Impact of refrigeration systems on energy consumption and environment

Cooling processes are crucial for many industrial and residential applications. The electrical power demand is continuously increasing around the world and using the cooling systems is one of the major factors that cause this increase especially in the four major emerging economies; Brazil, Russia, India and China (BRIC) and in the wealthy oil nations of the Gulf Cooperation Council (GCC) [6], [7]. For example, the sales of air conditioning systems have approximately doubled between 2009 and 2013 in China, where 64 million units were sold in 2013. This figure was more than 8 times greater than the figure of the units sold in the USA [8]. 30% - 50% of the total electrical energy consumed during summer in many countries such as Australia is due to the electric air-conditioning systems [8], [9]. Lam et al. [10] estimated the average electricity consumption for Hong Kong due to the use of electric air-conditioning systems in 2009-2038, 2039-2068, and 2069-2100 would be 5.7%, 12.8%, and 18.4% respectively higher than the consumption in 1979-2008. Therefore, electric air-conditioning systems are one of the main

contributors to the global warming phenomenon in two different ways. The first is that these systems participate in increasing the CO_2 and other pollutants emissions because of their high demands for electricity, and combustion is the most common and cheap technology for electricity generation, which accounts about 67% of electricity generation around the world as shown in Figure 1.3 [1].

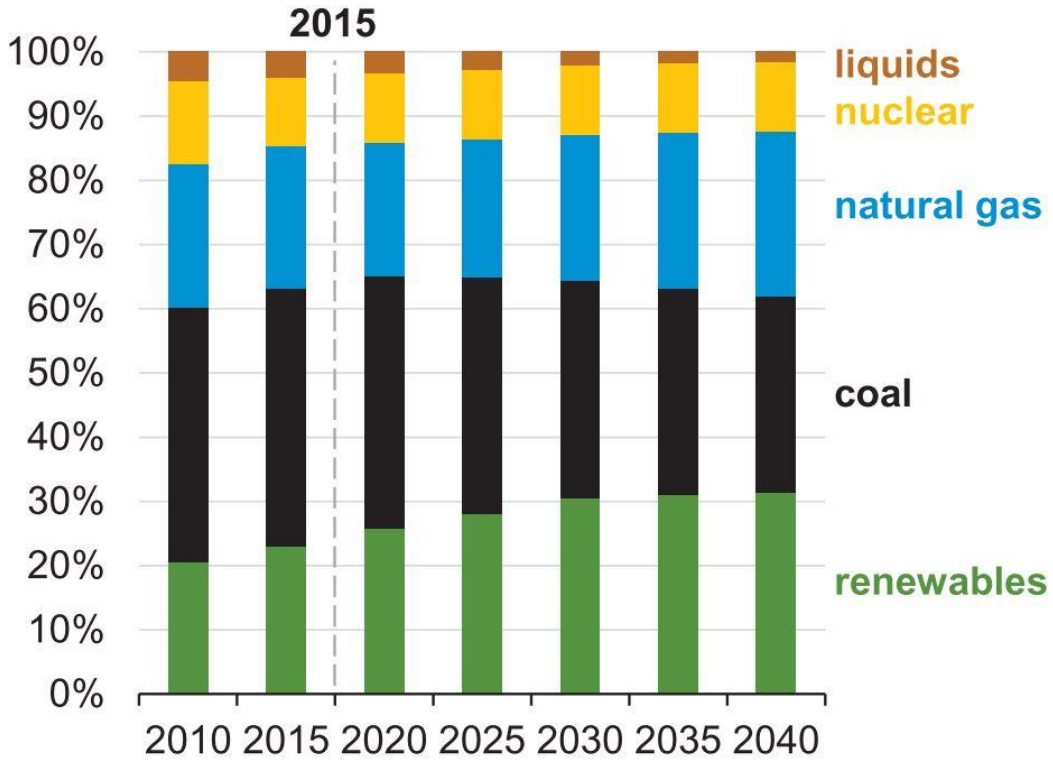

Figure 1.3 Estimated global share of net electricity generation by different energy sources [11].

The second way is due to the refrigerant leakage, which could be classified as [12]:

- Refrigerants having a strong destructive effect on the ozone layer with a significant contribution to the global warming phenomenon –

chlorofluorocarbons, CFCs. According to Montreal Protocol 1987, signatories agreed to phase out CFCs production in 1995 [1].

- Refrigerants having a reduced destructive effect on the ozone layer with a moderate contribution into the global warming phenomenon – hydro-chlorofluorocarbons, HCFCs. According to revised Montreal Protocol, the HCFCs will be eliminated by 2030 [1].
- Refrigerants having a harmless effect on the ozone layer with less contribution to the global warming phenomenon – hydro-fluorocarbons, HFCs.
- Refrigerants having a harmless effect on the ozone layer with very less or even no contribution to the global warming phenomenon – NH_3 (R717) and H_2O (R718).

Using water (R718) as a refrigerant in refrigeration systems is very attractive since it is cheap, available, non-toxic and eco-friendly.

1.2 Global Concerns

Renewable and cleaner energy conversion technologies have drawn intense interest. This interest is to overcome three main global problems: continuous increase in power demand, unavoidable fossil fuel depletion and pollution issues, which are the results of continuous economic development and population increase of the globe [11]. The Population Division of the United Nations estimates the world's population would be 8.3 billion in 2030 and 8.9 billion in 2050 comparing to 7.4 billion for 2015 [13]. Also, the data published by both the United Nations and the U.S. Energy Information Administration (EIA) shows a continuous increase in the world's energy consumption and the

estimated projection of the world's energy consumption in 2040 is twice (i.e., ~700 x 10^{15} Btu) the consumption in 1990 (i.e., ~350 x 10^{15} Btu) [11], [14], [15]. Furthermore, the fossil fuels remain the largest source of energy (e.g., fossil fuels represent 83.33% of the world marketed energy in 2015) [11]. Moreover, the world's electricity generation remains increasing at a high rate with a contribution of ~12.63% of the total energy consumption in 2015 [11].

Combustion is the most common and cheap technology used to convert fuels into useful energy. Combustion is used in a daily manner in different activities such as transportation, electricity generation, manufacturing, heating, cooking, etc. However, the overuse of combustion of fossil fuels has led to a global issue, i.e., climate change. Weather patterns change, sea level rise and extreme weather events are the significant impacts of the climate change. As shown in Figure 1.4, the anthropogenic emissions of Carbon dioxide (CO_2) from burning fossil fuel is the dominant greenhouse gas (GHG), which is the reason behind why the energy consumption is always at the centre of the climate change debate [16]. GHG emissions are responsible to the global warming and climate change phenomena and they are now at the highest level [17]. Many countries adopted the Paris Agreement at 21st Conference of Parties in Paris (COP21) on November 30 through December 12, 2015, which entered into force on 4th November 2016. This agreement addresses climate change and provides a roadmap to reduce emissions and build climate resilience. Fortunately, affordable and scalable solutions, such as using renewable energy, can be adopted by countries to heal the climate [17].

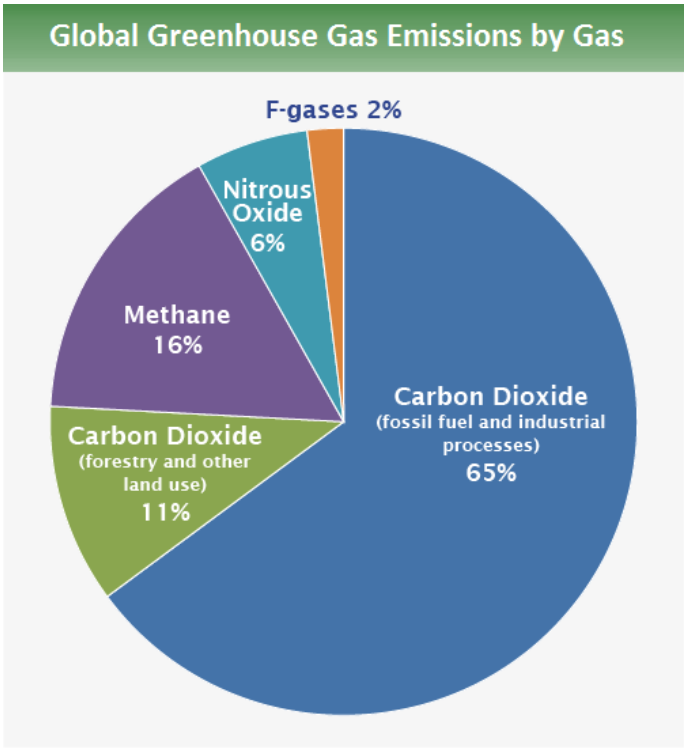

Figure 1.4 Global Greenhouse Gases Emissions [18].

1.3 Research Motivation

Four main reasons have raised the motivation to conduct this research and they are:

1- Electric air-conditioning systems are one of the main contributors to the global warming and climate change phenomena causing extreme weather patterns such as hotter summers and colder winters around the world. This, in turn, increases the demand for electric air-conditioning systems leading to a complex issue. This, in addition to the day-to-day rise in the human population and trying of emerging nations to cope the developed nations such as G6, leads to purchase cooling systems in huge volumes not just for luxury but to overcome

the high temperatures. Therefore, developing efficient cooling systems powered by renewable energy sources is a key solution to solve this issue.

2- The fact that solar energy, as one of the clean energy resources, is the largest and the inexhaustible resource on the earth (Figure 1.5) has stimulated the scientists to develop technologies, which can harvest and convert this energy into heat, mechanical, and/or electrical energy. Furthermore, an excellent opportunity is available to drive cooling systems thermally by exploiting solar technologies since the peak cooling demand is associated with high solar radiation in summer. Solar energy technologies are worth especially in places which are replete with year-round sunshine. Figure 1.6 shows the world's map of the annual solar flux (kW/m^2/year) with good to excellent availability between 45^o North and 45^o South [19]. This fact increases the opportunity to develop solar-powered air-conditioning systems to face the searing temperatures. Such technology can be utilized in many sectors such as resident, industry, healthcare, agriculture, sports, and supermarket, reducing the electrical power demand and saving the earth.

3- Cooling systems based on H_2O-LiBr based VARSs are a mature technology and well developed for a long time. They are eco-friendly as water is the refrigerant [20]. They can work on low and medium generator temperatures; therefore, flat plate solar collectors, vacuum tubes and even solar concentrators can be used to utilize the solar energy in the production of cooling (Figure 1.7) [5]. However, the main challenge that facing the H_2O-LiBr based VARSs is the high initial cost

due to the low COP and consequently the big size comparing with the VCRSs (see Figure 1.8). The low heat and mass transfer characteristics of the H_2O-LiBr solution are responsible for big absorber and generator, the intrinsic components of any absorption refrigeration system.

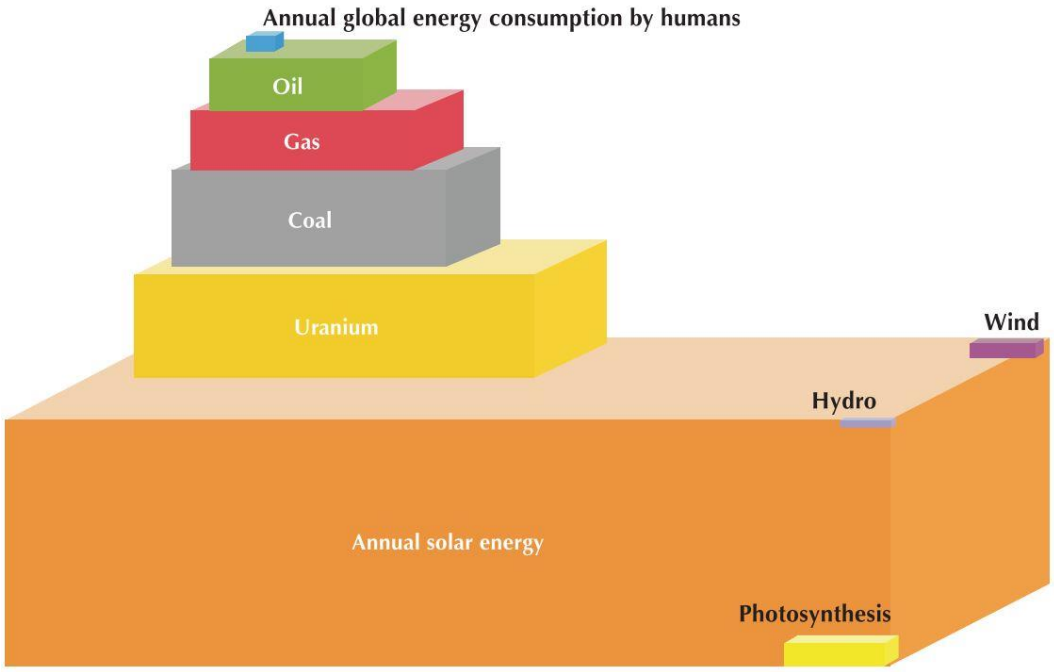

Figure 1.5 Estimated availability of different energy resources compared to the estimated annual energy consumption by humans [19].

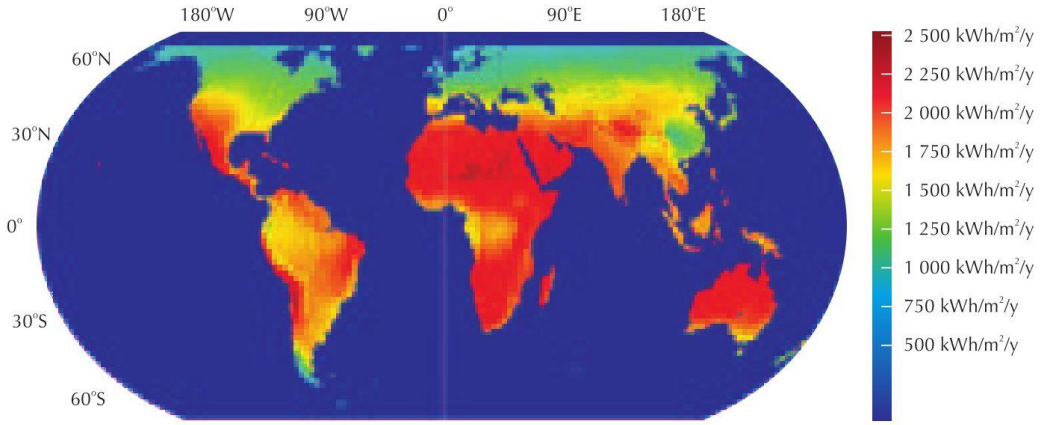

Figure 1.6 The global solar flux on the earth surface [19].

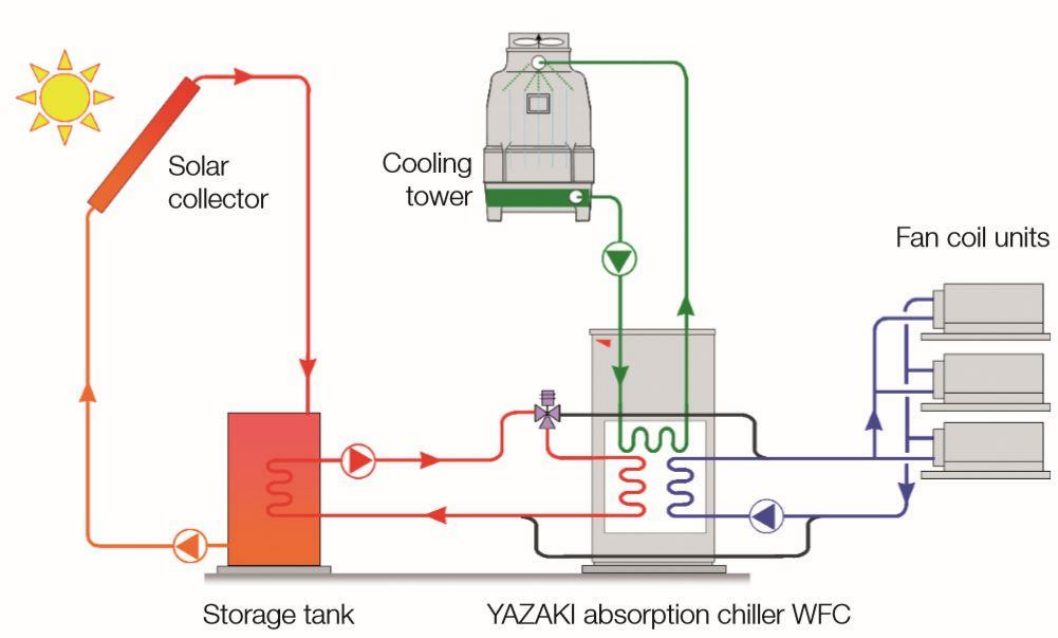

Figure 1.7 Conventional solar-driven VARS for air conditioning application [21].

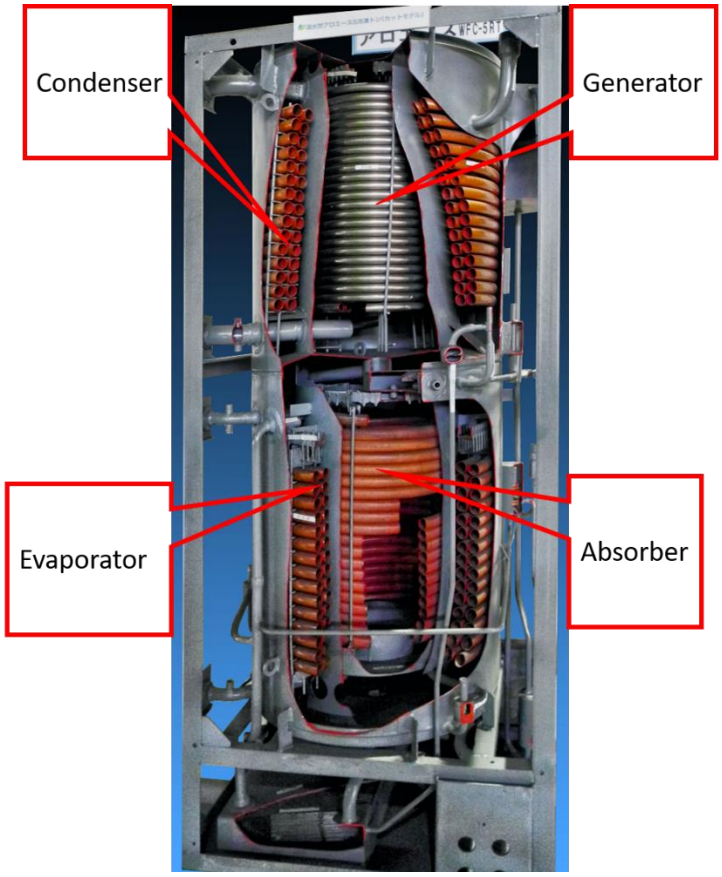

Figure 1.8 A cut in H_2O-LiBr VARS [22].

4- On the other hand, nanotechnology has received extraordinary interest for its fascinating potential to provide non-conventional alternatives in many applications such as medicine, pharmacy, cosmetics, food industry and energy transformation and conversion. The rapid development in synthesizing and characterizing methods has increased the capability of tuning the nanofluids' properties [23], [24].

It should be noted that the conventional solar VARSs (presented in Figure 1.7) are utilising conventional solar collectors (SCs) such as flat plate ones, which typically have absorbing plates with fluid running inside pipes. The efficiency of these conventional SCs is limited by not only how efficiently the solar

energy is captured by the absorbing plate, but also how effectively the absorbed energy is transferred to the running fluid [25].

In this work, we are proposing to use direct absorptive nanofluids to enhance solar energy harvest and to enhance the efficiency of VARSs. Properly engineered, these nanoparticles are expected to capture solar energy directly in a fluid phase that contribute to the performance of the generator and intensify the mass transfer process in the absorber. Here we are suggesting two possible scenarios to utilize the direct absorptive nanofluids in a solar-driven absorption refrigeration system:

1- Indirect system: A direct absorptive nanofluid is used in a solar collector system, where it harvests the solar energy directly via the suspended nanoparticles and transfers the heat to a storage tank. The required heat is supplied from the storage tank to the generator via a pump (P2) to increase the temperature of the solution film, which is pumped by the pump (P3) from the absorber, falling on the tubes bundle in the generator. Consequently, the refrigerant vapour will be desorbed at the design pressure and temperature. The refrigerant vapour passes through the condenser to complete the cycle as described in the subsections 1.1.1 and 1.1.2. In this way, the nanofluid does not participate in the refrigeration cycle, as shown in Figure 1.9 schematically, but to provide heat to the generator in an efficient way.

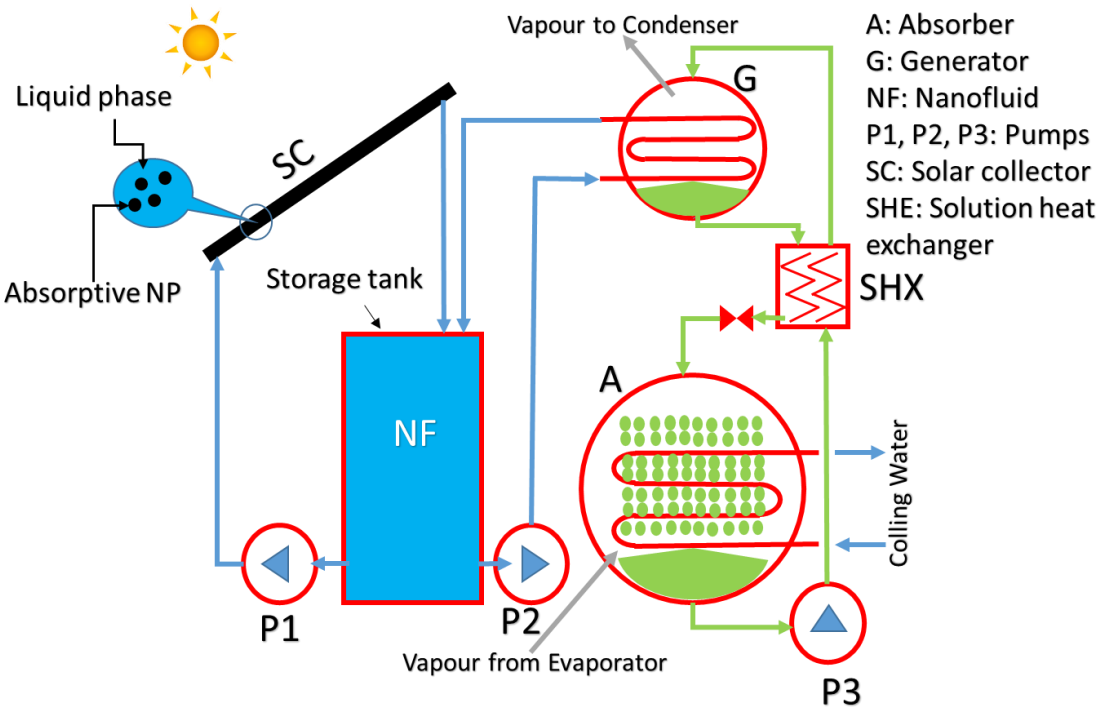

Figure 1.9 Indirect system, where the nanofluid does not participate in the refrigeration cycle.

2- Direct system: Nanoparticles are directly seeded in an aqueous lithium bromide solution to form a nanosolution that participate in the refrigeration cycle, as shown in Figure 1.10. In this way, the nanosolution is circulated through the absorber, the solution heat exchanger and the generator in sequence by a pump. In the absorber (A), nanoparticles are expected to promote the absorption process of the refrigerant vapour by the nanosolution film falling on the tubes bundle of the absorber via mass transfer intensification. In the solar collector (SC), the nanoparticles can harvest the thermal energy from the Sun directly, leading to increase the temperature of the nanosolution to the desirable temperature so that when the nanosolution is sprayed on the tubes bundle of the generator (G), the

refrigerant vaporizes at the generator pressure. The refrigerant vapour then passes through the condenser to complete the cycle described in the subsections 1.1.1 and 1.1.2.

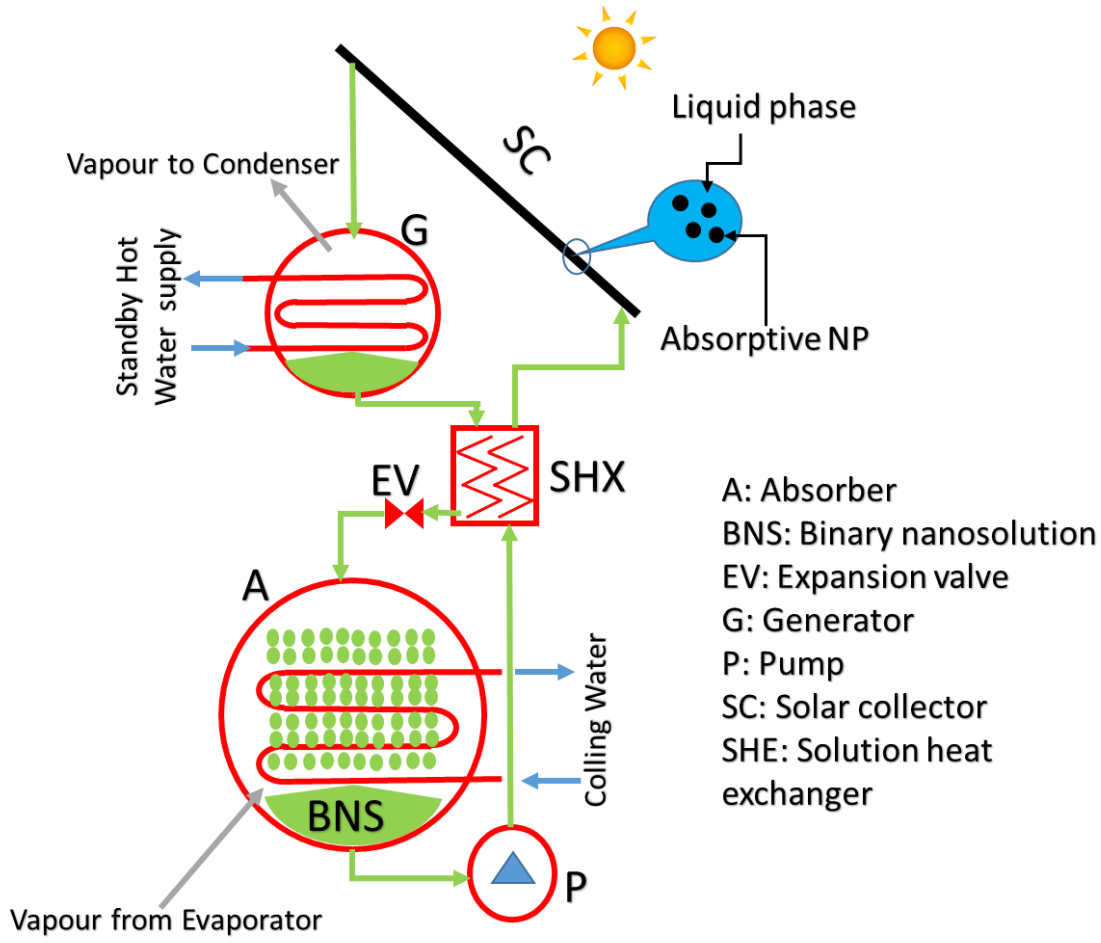

Figure 1.10 Direct system, where the nanoparticles in H_2O-LiBr solution.

There are many challenges associated with this novel concept, which ranges from nanofluids stability in a highly ionic medium to system integration. The performance of nanoparticles in a binary fluid has not been reported. Three major questions are identified and will be addressed in this work: i) what are

the good nanofluids candidate for capturing solar energy directly, ii) how efficiently can nanofluids separate the refrigerant; and iii) can nanoparticles promote the absorption process?

1.4 Research Objectives

Addressing the two scenarios of possible use of nanofluids for solar absorption refrigeration systems, this work aims to develop suitable nanofluids (i.e., nanoparticle dispersion in water or aqueous lithium bromide solution) and investigate their photo-thermal conversion and steam absorption behaviours. It is expected that properly engineered nanofluids could capture the solar energy more efficiently, improve the heat and mass transfer characteristics, and increase the efficiencies of the generator and absorber of a solar absorption refrigeration system. In particular, the nanosolution could directly convert the solar energy radiation into heat, providing the generator with the required driving energy to produce the refrigerant (steam), and could enhance the steam absorption in the absorber. Consequently, a well-engineered nanosolution could be a key factor to reduce the size of the solar absorption refrigeration systems.

To investigate this novel hypothesis fundamentally, specific research objectives are as follows:

- Engineer and characterise different aqueous nanofluids and nanosolutions, including the stability in high ionic conditions.
- Investigate the photo-thermal conversion characteristics of different nanofluids under normal and focused solar radiation.

- Investigate the steam generation performance of formed nanofluids, and assess their potential application in the generator
- Investigate the steam absorption performance of the nanosolutions and evaluate their potential application in the absorber.
- Analyse the potential performance of direct absorptive nanofluids in the VARSs.

1.5 Thesis Outline

This thesis is divided into six chapters. The first chapter presents the importance of this research work through reviewing the background of the most common refrigeration systems, i.e., the VCRSs and VARSs, the differences between both systems, the impact of the VCRSs on the global warming, the global concerns regarding the energy and pollution issues, the potential of using solar-assisted VARSs to relief the peak demand of electrical power on national grids, the main challenges that face the solar VARSs, and the potential of using nanofluids to overcome these challenges. Furthermore, research objectives are suggested to investigate the novel hypothesis of seeding functional nanoparticles in the aqueous lithium bromide solution.

In the second chapter, an overview of the historical development of the solar refrigeration and the efforts of developing new VARSs are presented. Moreover, the literature related to the direct absorption solar collection and solar-assisted steam generation are reviewed critically. A novel idea of seeding functional nanoparticles in a binary solution (H_2O-LiBr) is concluded to harvest and convert the solar energy into heat efficiently in the generator to

produce the refrigerant (steam) and to enhance the refrigerant absorption in the absorber. Research questions are highlighted at the end of the chapter.

Chapter 3 addresses the photo-thermal conversion phenomenon via a nanofluid and it includes a comparative case study, which meant to investigate the photo-thermal conversion efficiency of different nanofluids at similar conditions in order to finally point out the most feasible nanofluid for the specific solar application.

Similarly, chapter 4 is to understand the solar-assisted steam generation process and to conduct a comparative study among different materials (nanofluids and porous medium) in order to figure out the feasible material to produce steam.

The fifth chapter contains the preparation procedure of the nanosolutions by seeding the feasible nanoparticles in the transparent aqueous lithium bromide solutions. The effects of seeding nanoparticles are investigated on some properties of the nanosolutions such as the transmittance, thermal conductivity and viscosity. Furthermore, the photo-thermal conversion and steam generation are experimentally investigated. Also, the negligible effect of the Brownian motion of the nanoparticles is demonstrated in this chapter.

In the final chapter, the conclusions and the recommendations are presented.

Chapter 2

LITERATURE REVIEW

In this chapter, an overview of the historical development of the VARSs and the early efforts of utilising the solar energy in driving these VARSs is presented. The trends of developing new VARSs are also introduced with focusing on the heat and mass transfer additives (surfactants and nanoparticles) and their controversial effects. Moreover, the literature of direct absorption solar collectors (DASCs) and solar-assisted steam generation is reviewed and analysed comprehensively. Finally, research questions need to be answered are presented.

2.1 Solar Refrigeration

Refrigeration is an old invention. In 1850, Edmond Carre developed an absorption refrigeration machine using water and sulphuric acid pair. After that, in 1859, Ferdinand Carre successfully showed that ammonia and water can be used to produce refrigeration and in 1860 he patented the first American commercial absorption unit [26]. Furthermore, solar refrigeration is actually not a recent invention. Augustin Mouchot successfully produced ice blocks at Expo 1878 Paris. He built a large parabolic solar collector using mirrors to focus the solar radiation onto a boiler built from black copper to generate steam, which in turn drove a thermal-powered refrigeration device [27].

Absorption refrigeration systems depend on absorbents, which are materials that can attract and hold gases or liquids. The liquid refrigerant evaporates at low pressure and temperature in the evaporator by absorbing the latent heat from the fluid that is needed to be refrigerated. If there is no sufficient mean that can provide continuous suction of the refrigerant vapour, the refrigerant vapour pressure increases until it reaches the saturation pressure ceasing the cooling effect. Instead of connecting the evaporator to the suction side of a compressor in the VCRSs, it is connected to an absorber, which contains a strong solution of absorbent dissolved in a refrigerant, in VARSs. The most common solutions are NH_3-H_2O (NH_3 is a refrigerant and H_2O is an absorbent) and H_2O-LiBr (H_2O is a refrigerant and LiBr is an absorbent). These systems are driven thermally to release the refrigerant from the absorbent in order to complete a closed cycle for refrigerant and absorbent. Heat is applied to the weak solution (weak in absorbent strong in refrigerant) in the generator at a convenient pressure for its subsequent condensation in a condenser. Therefore, there is no need of high shaft power to operate these systems and as a consequence, they can operate reliably and quietly utilizing low-grade heat sources such as waste heat and solar energy [4], [28].

Around 1945, Carrier Corporation pioneered the early lithium bromide absorption technology. This technology was very successful that stimulated other companies such as Trane and York International to begin manufacturing what are now called single-effect machines exploiting the gas as a heat source [29]. This business thrived in the USA until around 1975. The reduction in electricity prices and the belief of the depletion of the natural gas sources led

to governmental regulations preventing the use of gas in new constructions. The absorption refrigeration market was growing in Japan when it was collapsing in the USA. The technology was imported to Japan from the USA. between 1962 and 1964. The Japanese manufacturers soon began improving this technology and started domestic production. In the late 1980s, the VARSs market began its resurgence in the USA and the manufacturers licensed Japanese designs of the double-effect VARSs for construction in the USA. Since then, the VARSs market has expanded considerably [29].

Due to societal and scientific awareness regarding environmental degradation, great interest has again risen to develop this technology utilizing eco-friendly energy sources such as the solar energy. Many researchers have developed solar-assisted absorption refrigeration systems. Some studies are presented here.

Experimental work in Amman in 1992 to describe the performance of a 0.5 ton of refrigeration (TR), no storage, continuous, solar operated, locally manufactured lithium bromide absorption refrigeration system was performed by Hammad and Audi [30]. The peak actual coefficient of performance was 0.55. A flat plate collector of 3.6 m^2 and a parabolic concentrator of 0.15 m^2 aperture area and of 5 suns focusing ratio were used in series to feed the generator with hot water.

Hammad and Zurigat [31] described the performance of a 1.5 TR solar-operated, locally built-up lithium bromide absorption refrigeration system. The

system consisted of 14 m^2 flat plate solar collector and five shell and tube heat exchangers. The maximum coefficient of performance was 0.85.

Zinian and Ning [32] designed and constructed a 100 kW (28.5 TR) solar-powered absorption air-conditioning plant. 2160 heat-pipe evacuated tubular solar collector of the total aperture area of 540 m^2 was used in addition to lithium bromide absorption chiller, cooling tower, water storage tanks, circulating pumps, fan-coil units, auxiliary oil-burned boiler and control system. The cooling efficiency for the entire system was found to be around 20%.

Kim and Ferreira [33] reviewed different options of solar refrigeration. This review covered the solar electricity using photovoltaic panels and solar thermal using solar collectors to run mechanical vapour compression chillers, vapour absorption chillers and other refrigeration technologies. They found that the initial cost of a single-effect H_2O-LiBr absorption system was the lowest among the other solar refrigeration technologies, as shown in Figure 2.1. It is clear that the initial cost of a solar absorption chiller is 5 times higher than that of a compression chiller neglecting the cost of electricity production. It was concluded that the solar electric and thermo-mechanical systems were more expensive than the thermal absorption systems.

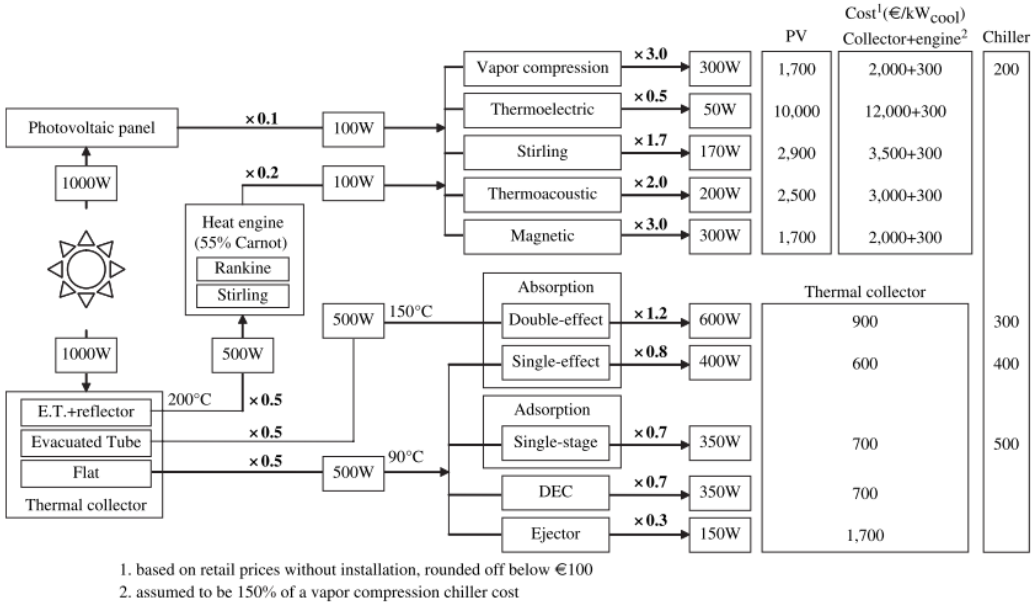

Figure 2.1 Performance and cost of various solar refrigeration systems [33].

The initial cost of a H_2O-LiBr absorption chiller is about twice as high as a comparable vapour compression chiller. This is due to the cost of heat exchangers required in absorption systems such as the absorber, generator and the solution heat exchanger. While the size and cost of the condensers and evaporators are roughly the same in both technologies [29], [33]. Furthermore, for the same cooling capacity, VARSs need larger cooling towers than the ones required for VCRSs since the COP of the former is lower than the later systems [29]. The absorber is the biggest and the costliest component in a VARS. This is due to the low performance of the absorption solution because of the low thermal conductivity and specific heat capacity and high viscosity and surface tension [34]. Where in a conventional shell and tubes absorber, the refrigerant vapour generated in the evaporator is absorbed by a strong absorption solution sprayed on the tubes bundle, which

in turn transfers and dissipates the heat of absorption as shown in Figure 2.2 [29], [35], [36]. Hydrodynamics of the absorption solution falling film – governed by the gravitational and shear forces – determine its thickness and velocity. Both the falling film thickness and velocity along with the tube's surface temperature are dominant factors that determine the heat and mass transfer within the absorber heat exchanger, where thicker films have higher heat transfer resistances, leading to higher interface temperatures and consequently lower rates of refrigerant absorption [35], [36].

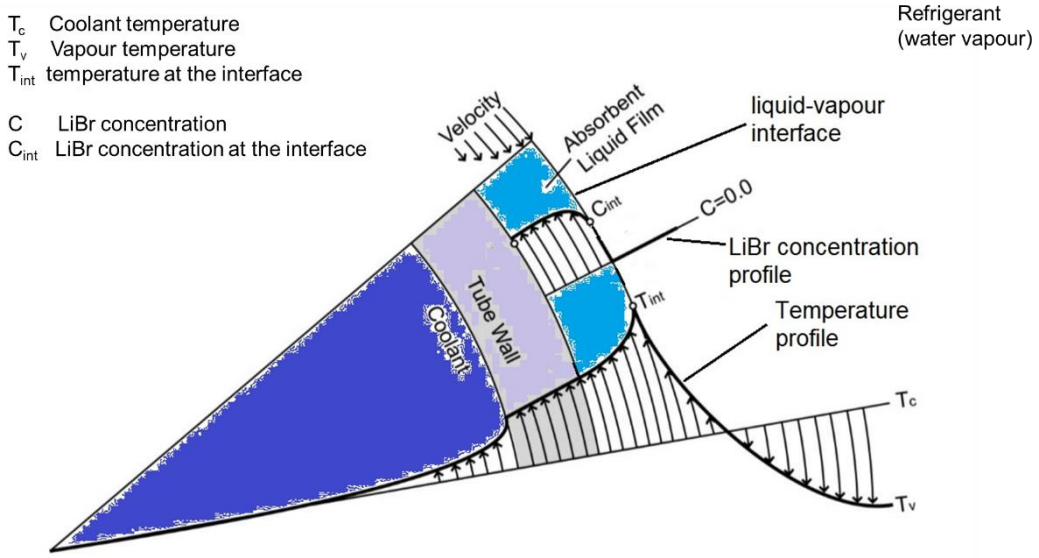

Figure 2.2 Representative temperature and concentration profiles on a section of a falling film of H_2O-LiBr solution on a horizontal pipe. [38].

Furthermore, producing the power required to run an absorption refrigeration system locally, of course, will increase the cost, size and complexity of the system. This is due to the need for power generators such as PV panels or solar collectors, energy storage such as batteries or storage tanks and

connections such as wiring and plumping [37]. As a result, the solar VARSs necessarily are bulky and complex and consequently are costly than the conventional VCRSs.

In general, H_2O-LiBr based VARSs are a mature technology, which can be operated by the solar energy via utilising solar collectors. However, the challenges that face this eco-friendly technology are the high initial cost (where the dominant part of this high cost is due to the high cost of the solar collectors and their auxiliary systems such as storage tanks and plumbing pipes), big overall specific size and weight, and low coefficient of performance (COP). Therefore, to reduce the initial cost and bulk size, enhancing the efficiencies of the intrinsic components (the absorber, generator and solar collector) of the solar VARSs is crucial and efforts have been conducted to develop new VARSs.

2.2 Efforts to Develop New VARSs

As shown in the previous section, the heat and mass transfer characteristics of an absorbent depend on the material type and the film thickness and velocity. Efforts have been done to improve these characteristics through developing new VARSs. Developing new VARSs can be classified into developing; new working fluids [39]–[43], compact heat and mass transfer exchangers, i.e., thinner films of absorbents [35], [36], [44], [45] and new additives [46]–[52]. Among various efforts to reduce the size of conventional absorbers, membrane-based and microchannel-based absorbers are

promising ones. Porous membranes were developed to mechanically control thin absorption films. These membranes were superhydrophobic to prevent the solution from entering the membrane, but allow the refrigerant vapour to access through them and finally be absorbed by the constrained solution. This design achieved a compact size and high-performance absorbers. Nasr Isfahani et al. [35], [36] built a compact size absorber utilising a plate-and-frame with microchannels (160 and 100 μm deep) and a gas permeable porous membrane (~1 μm pore), and experimentally examined the effects of the solution film thickness and the flow velocity on the absorption rate. The results demonstrated that the reduction in the film thickness and the increase in flow velocity enhanced the absorption rate. An absorption rate of 0.006 kg/m^2 s was achieved at a film thickness and flow velocity of 100 μm and 5 mm/s respectively, which was higher than the absorption rate of conventional tubes-and-shell absorbers (i.e. 0.0024 kg/m^2 s). Therefore, utilising superhydrophobic porous membranes could facilitate developments of compact sizes and waste heat or solar VARSs.

Utilising hydrophobic porous membranes stimulated Hong et al. [53] to propose a new design of a VARS for transportation applications instead of the conventional VCRS, and to conduct a parametric simulation for the performance of the proposed design. The suggestion of using a hydrophobic porous membrane was to build up a compact generator, and to constrain the aqueous LiBr solution mechanically, solving the problem of the unstable performance of conventional VARSs when a vehicle moves on hills or undergoes unexpected vibrations. The results showed that a cooling capacity

of 2.88 kW and a COP of 0.63 can be achieved. If this new design is applied to the transportation vehicles, it will participate effectively in solving the environmental damage in two ways: firstly, the use of eco-friendly refrigerant, i.e., water, instead of the harmful ones such as Freon, and secondly, using the waste heat of the exhaust gases to drive the VARS instead of the conventional high shaft power required by a conventional VCRS.

Although the use of hydrophobic membranes in microchannel-type heat exchangers looks effective to reduce the size of the absorber and the generator in a VARS, the most important limitation is the need to high pumping power to overcome the coherent high pressure drop, which affecting the system efficiency negatively, where the pressure drop is inversely proportional to the channel diameter to the power 4 according to Darcy-Weisbach equation.

Another way to improve the performance of the absorber and desorber is the use of heat and mass transfer additives, which are surfactants. Surfactants are materials that reduce the surface tension of the working fluids. For a long time, it was speculated that the surface tension of the absorption solution is a key factor influencing the absorption performance, i.e., the lower surface tension is, the higher absorption rate can be achieved. However, this point is controversial because it was found that negligible enhancement was achieved by using some surfactants [54].

Kulankara and Herold [54] experimentally studied the effect of four different alcoholic surfactants (volatile materials), namely 2-ethyl-1hexanol (2E1H), 3,5,5-trimethyl-1-hexanol (TMHX), 2-methyl-1-hexanol (MHX) and 3-phenyl-1-propanol (PHPP), on the surface tension of the aqueous LiBr solutions. They used the drop weight method for the surface tension measurements. It was found that the presence of additive vapour around the drops was more effective than the presence of the additive in the drops in reducing the surface tension. For example, they found that the surface tension of 100 ppm 2E1H in 60 wt.% aqueous LiBr solution was 90 mN/m in case of negligible presence of additive vapour around the drops, while the surface tension of the same sample was 44 mN/m in case of introducing the drops to rich additive vapour environment. They concluded that due to the low mass diffusivity of the surfactant in the solution, the surfactant concentration was governed by the adsorption characteristics of the solution drops. The existence of a surfactant in the gaseous phase around the liquid phase was more significant since the solution had a high affinity for adsorption and the surface tension is very sensitive to the surfactant concentration.

However, Cheng Wenlong et al. [55] concluded that no matter if the additive is in the aqueous LiBr solution or in the gaseous phase around the solution, but its amount at the interface determines the value of the surface tension. They measured the surface tension of 55 wt.% aqueous LiBr solution with 2-ethyl-1-hexanol (2E1H) and 1-octanol using the Wilhelmy plate method in open and closed systems. The surface tension of the aqueous LiBr solution was oscillating and increasing with time for the open system (exposed to air),

while it was steady and lower for the closed system. Their interpretation for this discrepancy was that in the open system case, the volatilisation rate of the additive from the surface layer (because its partial pressure in the solution is higher than in the air) was higher than the diffusivity rate from the bulk solution to the surface layer. Since the solution had a high affinity to absorb the moisture from the air, the additive concentration in the surface layer decreased, and the surface tension increased rapidly. While in the closed system, the volatilisation rate was zero as the partial pressure of the surfactant in the air was equal to that in the solution. As a result, the surfactant concentration was almost constant even the solution absorbed moisture from the surroundings. This is due to the high affinity of the surfactant vapour to adsorb on the solution surface. The main concluded point was the surface tension is directly controlled by the surface excess additive concentration.

The surface excess of an additive, which controls the surface tension, is presented in form of islands distributed heterogeneously on the film surface. These islands were nicely demonstrated by Nakoryakov et al. [56] using a high quality camera, as can be seen in Figure 2.3. These islands resulted in un-even surface tension distribution, which in turns, produced Marangoni convection. This was also demonstrated by the same authors using a high quality IR camera as shown in Figure 2.4. The enhancement of the absorption performance of aqueous LiBr solution due to Marangoni convection using different alcoholic surfactants was also certified by Daiguji et al. [57]. They proofed experimentally and theoretically that using surfactants enhances the absorption performance of immobile aqueous LiBr solutions.

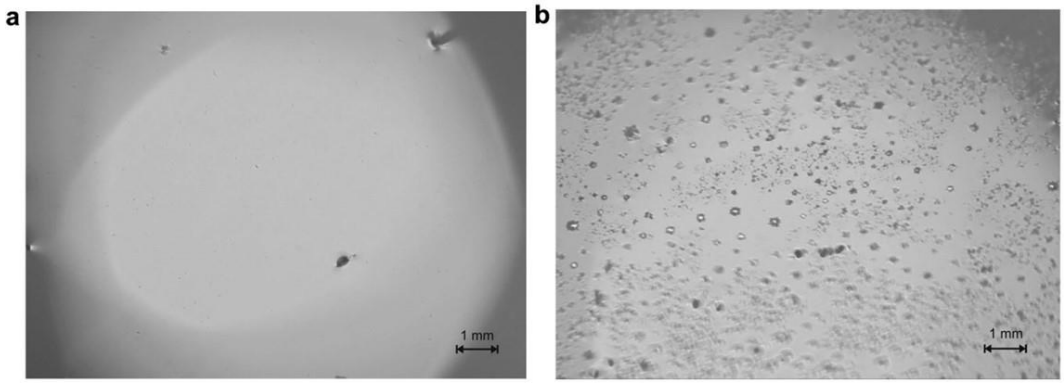

Figure 2.3 Pictures of the surface of an aqueous LiBr solution: (a) without surfactant and (b) with surfactant at 400 ppm [56].

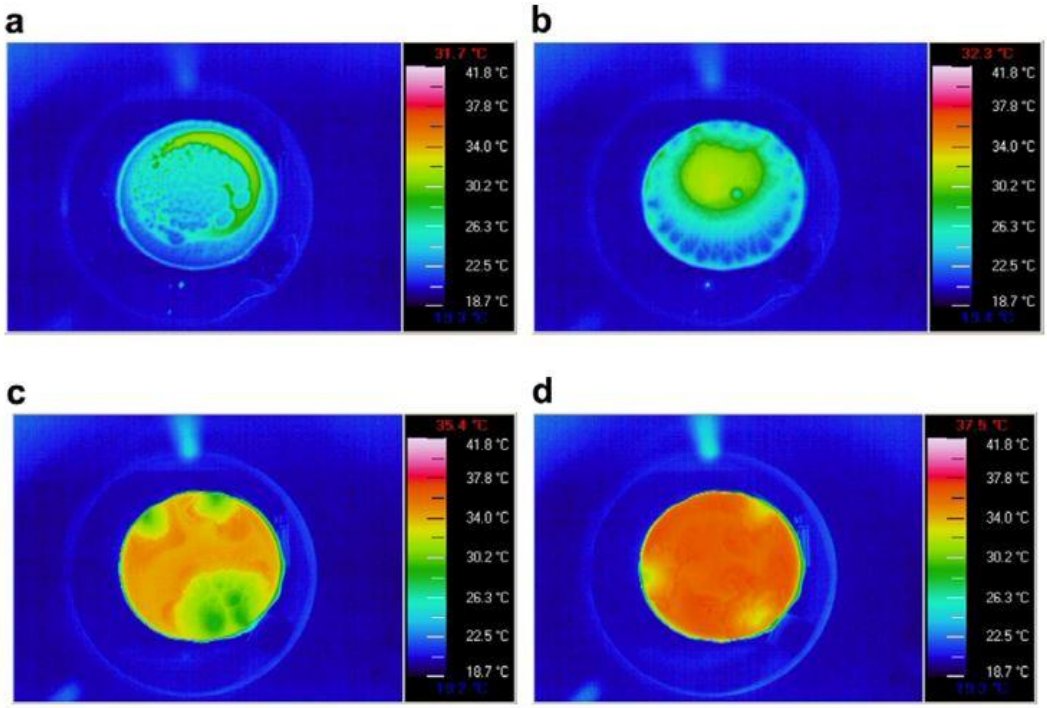

Figure 2.4 Thermograms of the moving surface layer of the aqueous LiBr solution with surfactant at (a) 1 s, (b) 10 s, (c) 60 s and (d) 120 s [56].

To mimic the effect of adding these surface active agents (surfactants) on the performance of a real absorber, Kang and Kim [58] designed and conducted a falling film absorption experiment to examine the effect of adding 2-Ethyl-1-Hexanol, 2-octanol and n-octanol to the H_2O-LiBr solution, in addition to the

effect of the roughness of the absorber's pipes on the heat and mass transfer. Bare, #600 and #24 (i.e., the roughness of 0, 0.39 and 6.97 μm) were used in their study. They concluded that heat and mass transfer additives (chemical treatment) have a higher significant effect than the micro-scale hatching (mechanical treatment). Chemical additives enhance the surface wettability by reducing the surface tension and cause interfacial turbulence due to the Marangoni effect. While mechanical treatment can only increase the surface wettability via the capillary force. They achieved a heat transfer rate of 2.4 higher by using just the mechanical treatment and 3.8 higher by using only 2E1H. However, they achieved a higher rate of 4.5 by using both mechanical and chemical treatments.

Recently, researchers have been investigating the use of nanotechnology in VARSs. Since the first proposition by Choi [59] of using nanofluids as potential alternatives for the traditional heat carriers through enhancing the thermal conductivity of the base fluid, huge efforts have been conducted to investigate the effects of nanoparticles on the overall properties of the nanofluids. Although some studies reported a reduction in the heat transfer coefficient, many studies reported anomalous enhancement if nanofluids are used instead of traditional working fluids [60], [61]. Brownian motion of the nanoparticles and subsequent micro-convection was suggested as one of the major responsible factors in the heat transfer enhancement [61]. This suggestion has stimulated researchers to utilise nanoparticles in mass transfer enhancement.

Kim et al. [62] conducted experimental work to investigate the heat and mass transfer enhancement of falling film absorption of H_2O-LiBr 53 wt.% using SiO_2 nanoparticles (20nm) and surfactant (150 ppm of 2-Ethyl-1-Hexanol (2E1H)) over 8 horizontal copper tubes (15mm in diameter, and 500mm length). They found that, the maximum heat and mass transfer was at 0.005 vol.% of SiO_2, where the heat transfer enhancement (~46.8% with only nanoparticles and ~23% with nanoparticles and surfactant) was higher than the mass transfer enhancement (~18% with only nanoparticles and ~5% with nanoparticles and surfactant). They mentioned that adding surfactant weakens the convective motion of the nanoparticles where Brownian motion gives significant impact on the absorption performance.

However, Kang et al. [46] used the same experimental setup but different nanoparticles (i.e., iron, Fe 100nm and carbon nanotubes, CNTs 25nm in diameter and 5µm length), and Gum-Arab as the dispersing agent. Entirely different results were obtained, and the mass transfer enhancement (i.e., ~210% for 0.01 wt.% CNTs) was significantly higher than the increase in heat transfer (i.e., ~5%). The authors reasoned their results to a catalytic role of the nanoparticles, which enhanced the diffusion rate within the falling film of the nanosolutions. Similarly, Lee et al. [47] investigated experimentally the effect of Al_2O_3 nanoparticles and Gum-Arab and 2E1H additives on the performance of a falling film of H_2O-LiBr solutions. Their results showed an increase in the steam absorption rate up to 77% using 0.01 wt.% Al_2O_3 and 2E1H, and a heat transfer enhancement of 19%.

Recently, Wang et al. [50] investigated the mass transfer characteristics of nanosolutions (i.e., aqueous LiBr (58 %) seeded with CuO nanoparticles (0, 0.05, and 0.1 vol.%) falling film mathematically and experimentally. They used the MATLAB software to solve the continuity, momentum, energy and mass transfer equations numerically. They achieved a very good agreement between the experimental and mathematical model data by adopting viscosity and thermal conductivity as functions of the number of the nanoparticles. The mathematical model and experimental results showed an enhancement in steam absorption as a function of the nanoparticles number and the flow rate. Nanoparticles number and flow rate increases, steam absorption increases. Although their mathematical model did not consider the Brownian motion of the nanoparticles, they considered in their conclusions that the Brownian motion and the related micro-convection in the nanosolution were the major responsible factors affecting the mass transfer. Moreover, they used gum Arabic by a quantity of 5 times higher than the CuO nanoparticles to disperse the high concentration of the nanoparticles (i.e., 0.1 vol. % = 6400 mg/l). Gum Arabic, as an organic polymeric material, increases the viscosity and reduces the surface tension of a solution. However, Wang et al. [50] ignored the effect of gum Arabic in their study and they did not give a clear mechanism how Brownian motion can enhance the steam absorption.

Pang et al. [60] published a review of combined heat and mass transfer characteristics in nanofluids. They concluded that generally the absorption rate of gas in a solution increases as the nanoparticle concentration increases, which improves the mass diffusion within the bulk solution. However, it is

supposed to achieve higher absorption rates with smaller sizes of nanoparticles at the same nanoparticle concentrations, but it was found that the higher absorption rates related to the big size nanoparticles as shown in Figure 2.5. It is obvious that the absorption ratios order (from the highest to the lowest) was achieved by the CNT (100 μm * 25 nm), Fe (100 nm), Al_2O_3 (20 nm) and SiO_2 (10-20 nm).

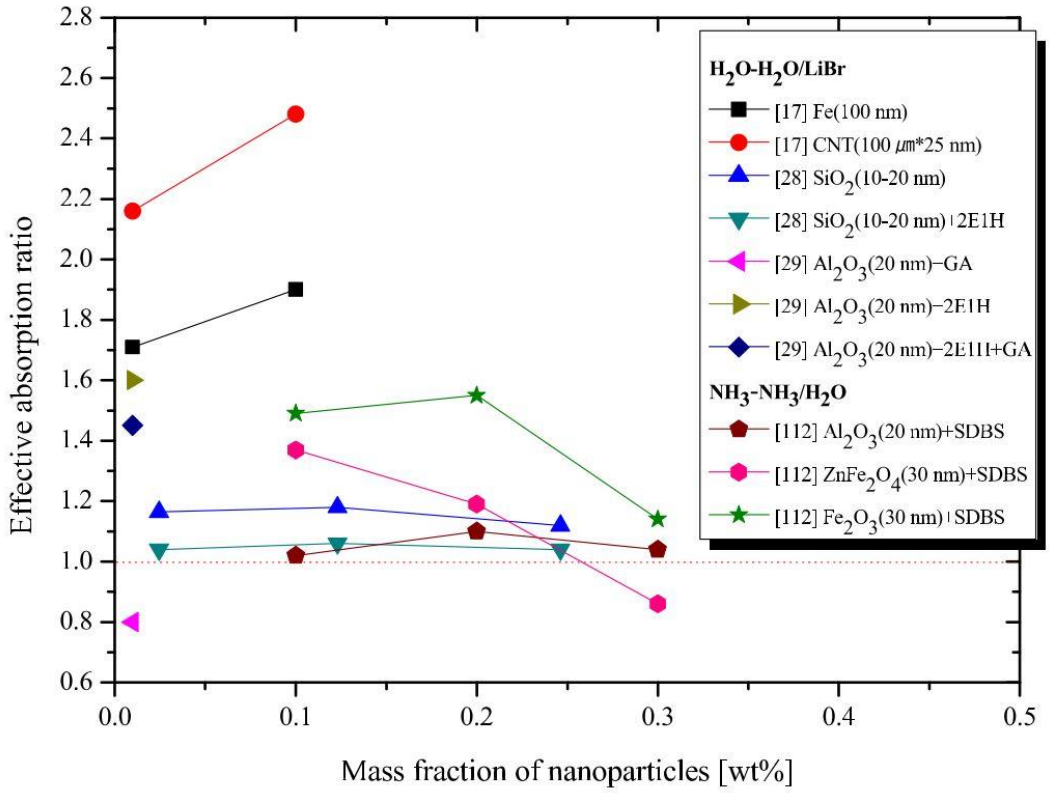

Figure 2.5 Effective absorption ratio with a falling film nanosolutions [60].

As an absorption process of steam into a solution is governed by (1) diffusion and (2) heat transfer, the fluid film should be thoroughly mixed to enhance the mass and heat transfer [63]. However, an obvious problem with the falling film experimental setup is that it is difficult to ensure the same surface area and

the thickness of the falling film- which are depending on the wettability and the solution flow rate [63]- in each run (see Figure 2.6). Therefore, it is difficult to judge that the achieved enhancement was due to the Brownian motion and the related micro-convection and/or the grazing effect of the nanoparticles, especially the results showed an increase in the mass and heat transfer through the falling film when the flow rate of the nanosolution was increasing until a certain value. Beyond that value, the mass and heat transfer changed negligibly.

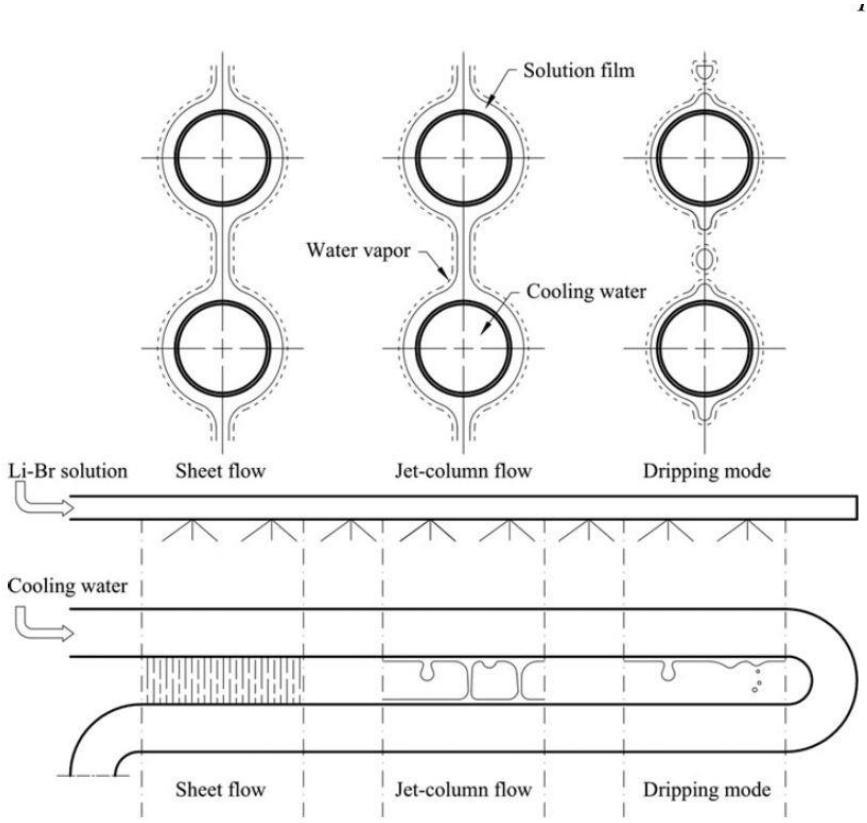

Figure 2.6 Illustration of the falling film modes (dripping, jet-column and sheet modes) [63].

Another benefit from seeding nanoparticles within a solution is the direct solar energy absorption, which is used to desorb the refrigerant in the generator. Phelan et al. [64] proposed the use of nanosolutions in solar VARSs. They suggested to re-direct the solar radiation into the generator of a VARS through a transparent window. The solar radiation will be directly converted into thermal energy via the dispersed nanoparticles, increasing the temperature of the nanosolution and generating the refrigerant.

Basing on the previous proposal, Gulati et al. [52] investigated numerically the performance of a VARS seeded with nanoparticles, namely aluminium, aluminium oxide and graphite. Their proposal was to direct the nanosolution into a direct absorption solar collector to harvest the solar energy and convert it into thermal energy. In addition to the base working fluid's optical properties, the diameter and the optical property, namely refractive index, of the nanoparticles were used to calculate the extinction coefficients of the nanosolutions. The solar energy distribution within the nanosolution was then calculated. A finite difference method was used to solve the energy balance equation to obtain the temperature distribution within the nanosolutions. They concluded that seeding nanoparticles directly in the generator's working fluid improves the VARS performance due to the absorption and scattering properties of the nanoparticles. They found the optimum nanoparticles concentrations as 0.6 vol.% and 0.04 vol.% for aluminium and graphite respectively. Three nanoparticle's diameters were used in their study, namely 10, 15 and 20 nm. Negligible effect of the nanoparticles diameter on the

performance of the VARS was found. They suggested using their model to investigate other nanoparticles types.

However, it is not correct to rely on the extinction coefficient alone to decide either a nanofluid is good for solar energy harvesting or not, as the extinction coefficient is the sum of the absorption and scattering coefficients. As it can be seen in Figure 2.7, although the extinction value of the silica colloid is higher than that of the gold nanofluid, the colour of the colloid is white, which is due to the visible light spectrum scattering from the silica particles back toward the observer. While the colour of the gold nanofluid is brownish-red, which is due to the absorption of the most visible light spectrum. Hence, the perfect material is the one which can collect most of the solar energy and convert it into heat, and its colour must be a perfect black.

In the next section, a comprehensive literature review regarding the photo-thermal conversion of the nanofluids is presented to figure out the new trends in producing perfect direct absorption solar collectors.

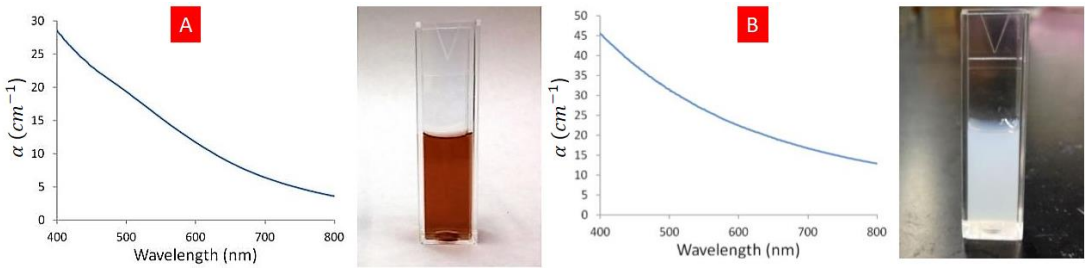

Figure 2.7 The spectral extinction coefficient. (A) 2 nm gold nanofluids. The brownish-red colour appears in the photograph is due to the light absorption across the entire visible spectrum. (B) 1 μm silica colloid. The colour appears white since the visible light spectrum is scattered from the particles back toward the observer. [65]

2.3 Direct Absorption Solar Collectors (DASCs)

Solar energy has been claimed as the energy of our future but comes with many challenges to overcome such as the high cost (due to using optical devices such as heliostats or reflectors to concentrate the solar energy, tracking devices to track the energy source, and vast land for installation) and the low efficiency (due to the heat losses) [25], [66], [67]. Solar thermal system, which typically has an absorbing plate with fluid running inside pipes, is a common way of utilising solar energy. Its efficiency is limited by not only how efficiently the solar energy is captured by the absorbing plate, but also how effectively the absorbed energy is transferred to the running fluid [25]. This surface-limited thermal energy transfer process limits the solar energy utilisation efficiency especially for high-temperature applications such as solar thermal power plants [68].

Direct absorption solar collector (DASC) is proposed in the 1970s. In this approach, the solar energy is directly absorbed by the working fluid by seeding certain particles in it [69]–[71]. Early studies were focused on micro-sized particles, and using nanoparticles is a recent development. Many studies have been conducted and most of these studies were based on the optical properties and characterized by the extinction coefficient [25], [72]–[76]. Although the extinction coefficient is a key factor, which determines the absorbed and scattered light by a nanofluid, it may not represent the actual photo-thermal conversion process; therefore, experimental photo-thermal tests possibly are more preferable [77].

The photo-thermal conversion efficiency of different nanoparticles, ranging from metal (such as Au, Ag, Cu, and Al), metal oxides (such as CuO, TiO_2, Al_2O_3, and Fe_2O_3) and carbon (such as Graphite, carbon nanotubes (CNTs), and carbon nanohorns (CNHs)), have been investigated under the laboratory and outdoor conditions. Plasmonic nanoparticles (such as Au and Ag) have attracted intense interest due to the effect of surface plasmon resonance (SPR), which usually occurs in the visible light spectrum, which represents almost 40% of the total solar energy [78] but weakly absorbed by most of the heat transfer fluids.

Among these studies, Zhang et al. [77] experimentally showed that using 6 ppm (~116 mg/l) aqueous gold nanofluid, which prepared by one-step method, could enhance the photo-thermal conversion efficiency by ~80% and reached a specific absorption rate (SAR) of ~1kW/g under 1 Sun from a solar

simulator. Bandarra Filho et al. [79] conducted the photo-thermal conversion tests of two-step aqueous silver nanofluids in the natural sunlight. An enhancement of 144% in the photo-thermal conversion efficiency and a specific absorption rate of ~0.6 kW/g were achieved by using 6.5ppm (~68 mg/l).

However, the enhancement in the absorption of plasmonic nanofluids has unavoidably a narrow bandwidth owing to their resonance characteristic [80]. Therefore, some researchers suggested to blend different nanofluids of different absorption peaks to get on a hybride of a broadband high absorption.

A blend of spherical gold nanoparticles with two different size gold nanoshells was proposed by Cole and Halas [81]. They theoretically determined the ideal fractions of the blended nanofluids that match the AM 1.5 solar spectrum, and revealed that mixing 35.9% gold nanospheres of 32 nm radius, 22.8% gold nanoshells of 28 and 42 nm core and shell radii, and 41.3% gold nanoshells of 47 and 58 nm core and shell radii respectively, can achieve a photo-thermal conversion efficiency of ~84%.

Another theoretical study was conducted by Lee et al. [82]. They theoretically investigated the efficiency of a direct solar collector using a hybrid core-shell gold nanofluid generated by mixing four different core and shell sizes. An efficiency of 70% was achieved by 0.05 vol.% (~ 3220 mg of gold/l) hybrid nanofluid. However, although the tunability of the optical properties of such core-shell nanoparticles is achievable, the difficulty in manufacturing this type

of nanoparticles makes it not suitable for further solar applications [80]. Very recently, a blend of three different nanofluids of gold nanorods of average length and aspect ratio of 26.6 nm and 1.77, 38.6 nm and 2.73 and 72.0 nm and 4.17 at different volumetric portions was suggested by Jeon et al. [80] as an alternative nanofluid suitable for solar applications. The total volumetric concentration was 0.0001% (~20 mg of gold/l) and the photo-thermal performance of the blended nanofluids was checked by measuring the temperature rise of the blend with time.

However, the common limitations, which can be drawn from the reviewed studies, are listed below:

1- The density of gold is high (19.4 g/cm^3 at 20^{o}C) comparing with other materials such as carbon (2 g/cm^3 at 20^{o}C). Therefore, even though a low volumetric concentration of gold nanofluid was prepared (as the one prepared by Jeon et al [80], [83]), the mass concentration remained high. The high cost of gold and the need for large amounts of working fluids for the solar applications push towards finding another alternative.

2- Preparing a hybrid from blending different nanofluids at different volumetric portions results in dilution of the counterparts in the hybrid nanofluid as the final volume is higher than the original one. Therefore, the peak of the extinction coefficient will be lower than the original peak according to Beer's law, which indicates that absorbance is linearly proportional to the concentration. However, a fair comparison between

the performance of the blended nanofluids and their original counterparts at the same concentration was not conducted.

3- These studies blended costly gold nanofluids to produce a nanofluid with a broadband absorption of the visible and near-infrared radiation. However, they ignored cheap nanofluids such as carbon black nanofluids, which have broadband absorption characteristic.

In many of the previous experimental studies, one thermocouple was used to measure the temperature rise of the nanofluids assuming a uniform temperature distribution although the effect of the optical path was not negligible, and that measured temperature rise was used to calculate the photo-thermal conversion efficiency [79], [84]–[87]. However, the non-linearly reduction in the radiative intensity along the depth of the nanofluid should cause a temperature difference within the nanofluid [88], [89]. Neglecting this temperature difference will lead to an inaccurate calculation of the efficiency. Moreover, most of the published work was based on only one particular type of particles, and a comparative assessment of the performance of commonly used nanomaterials for solar energy harness is still lacking. The effect of these nanomaterials needs to be investigated at the same concentration and under similar operating conditions to reach a fair comparison. In addition to the efficiency, the cost has to be considered very carefully for any practical application. For the purpose of comparison, some estimation of the cost of a unit heat generated in a unit time ($/kW) by different nanoparticles is preferred.

2.4 Solar-Assisted Steam Generation

Recently, DASCs have been proposed as novel solar-driven steam generation systems, and using gold nanofluids has attracted intense interest albeit they are among the most expensive materials. This interest comes from two main reasons: Firstly, most of the solar working fluids are semi-transparent for the visible spectrum, which represents ~40% of the solar energy, and the resonance of the conducting electrons of the gold nanoparticles can be tuned so that the peak absorbance occurs in the visible spectrum. As mentioned in the previous section, the enhancement in the light absorption has unavoidably a narrow bandwidth of the wavelength, which promoted the use of hybrids of different sizes and/or shapes of gold nanoparticles to broaden the bandwidth of the peak absorption. However, according to the Beer's law, a reduction in the peak absorption value necessarily occurs due to the dilution of gold nanofluids at a given total particle concentration. This means a higher concentration of gold nanoparticles is needed to prepare a hybrid with a broad bandwidth at the same peak value of absorbance. Secondly, the claim of nanobubbles generation around immersed nanoparticles can enhance the efficiency of the solar-driven steam generation, albeit the bulk temperature of a nanofluid still subcooled [90]–[92], is still subjecting to strong debate. It has been suggested that nanobubbles can only be generated under the very high intensity of light, i.e., of thousands of kW/m^2 [93]–[95], which consequently requires expensive optical and tracking devices.

Among recent studies that used gold nanoparticles to enhance the solar energy harvesting, Neumann et al. [91] concluded that steam can be generated efficiently if an aqueous nanofluid is subjected to the solar radiation. They used two types of nanoparticles, namely Au/SiO_2 shell/core and carbon nanoparticles in preparation of the nanofluids so that they had the same average extinction coefficients. A Fresnel lens (26.67 cm x 26.67 cm) of 44.5 cm focal length was used to concentrate the natural sunlight. The temperature and pressure of the generated steam were measured. The results showed a fast generation of steam. The pressure signal started in increasing after 5s and 20s and reached ~16.5psi and ~15.25psi after 50s of illumination the gold and carbon nanofluids respectively. However, after 50s of illumination, the temperature of steam generated from gold nanofluids reached ~23.5^{o}C while ~7.5^{o}C from carbon nanofluid. In another experiment, they measured the mass reduction of 25ml and 35ml of the nanofluids illuminated by concentrated solar energy using an analytical balance of 1mg resolution. One temperature sensor was inserted in the nanofluids to measure the temperature rise due to sensible heating. However, the experiments were conducted outdoors under natural sunlight; therefore, uncontrolled environment such as wind and clouds can affect the readings especially the analytical balance. The simple calculations showed that 42% of the solar energy was converted into steam, which represented 80% of total latent and sensible heats.

Neumann et al. [91] suggested the nanobubbles mechanism as the reason behind the high efficiency of steam generation as shown in Figure 2.8. Due to

the interfacial thermal resistance between the nanoparticles and water, the temperature of the nanoparticles goes up higher than the water boiling temperature producing steam nanobubbles surrounding the nanoparticles. Continuous heating causes a continuous increase in the volume of the nanocomplexes (nanobubbles plus nanoparticles), and these nanocomplexes float towards the nanofluid-air interface due to the buoyancy forces. Finally, steam escapes to the surroundings and the nanoparticles return to the nanofluid.

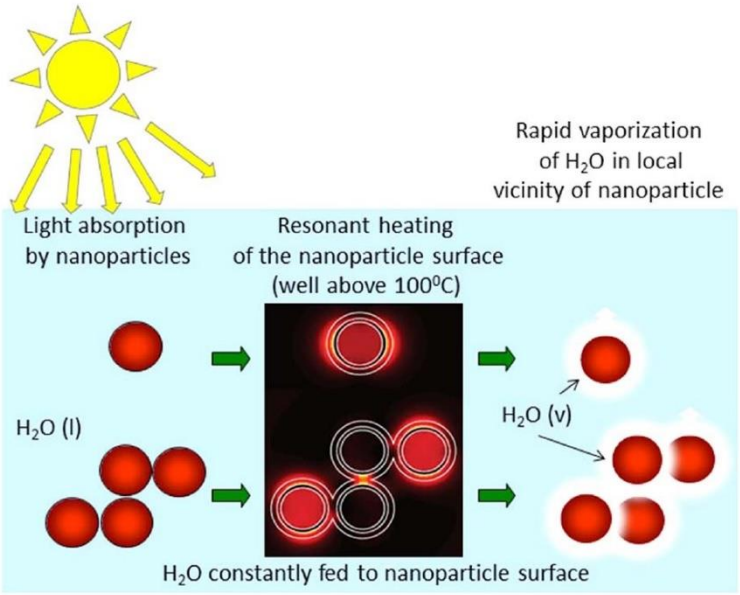

Schematic of nanoparticle-enabled solar steam generation: initially, light is absorbed by nanoparticles, raising their surface temperature above the boiling point of the fluid. The nanoparticle surface serves as a boiling nucleation site. Vapor is formed around the nanoparticle surface, and the complex moves to the liquid–air interface, where the steam is released. New liquid is replenished at the hot nanoparticle surface, and the process is repeated.

Figure 2.8 Schematic diagram for a suggested mechanism of solar steam generation via nanoparticles [91].

Neumann et al. suggested this technique, i.e., the nanoparticle-enabled solar vaporisation for different applications such as distillation [91], [96] and sterilisation [92]. They experimentally distilled ethanol from ethanol-water mixture seeded with gold nanoshell particles utilising the solar energy. They

got on an ethanol distillate significantly richer than the distillate got by using conventional thermal heat source [91]. In another work, Neumann et al. [92] built two prototypes of a solar-driven steam autoclave. Utilising the gold/silica nanoshell/core particles suspended in water to absorb the concentrated solar radiation from a parabolic dish, they succeeded to produce steam and maintain the temperature of 14.2L between 115^{o}C and 132^{o}C. They suggested their prototype to be used in remote areas out of electricity grids.

However, Phelan et al. [93] showed experimentally that the minimum irradiance required to generate boiling in different nanofluids is in the range of thousands of Suns (1 Sun = 0.1 W/cm^2) as shown in Figure 2.9. Furthermore, Baffou et al. [95] evidenced experimentally that the bubbles generated from illuminating gold nanoparticles submersed in water with intensive laser (thousands of W/cm^2) are not made from steam but from the dissolved air in water and high temperatures (> 220^{o}C) are required to trigger the bubble generation. Also, the experimental findings of Fang et al. [97] emphasized the need for very high radiation intensities to generate steam around nanoparticles. They found that the threshold intensity of the laser used to generate the steam around a gold nanoparticle (100 nm in diameter) was 2.5 * 10^{10} W/m^2, which was 2.5 * 10^7 folds higher than the value of the standard solar radiation, i.e., 10^3 W/m^2.

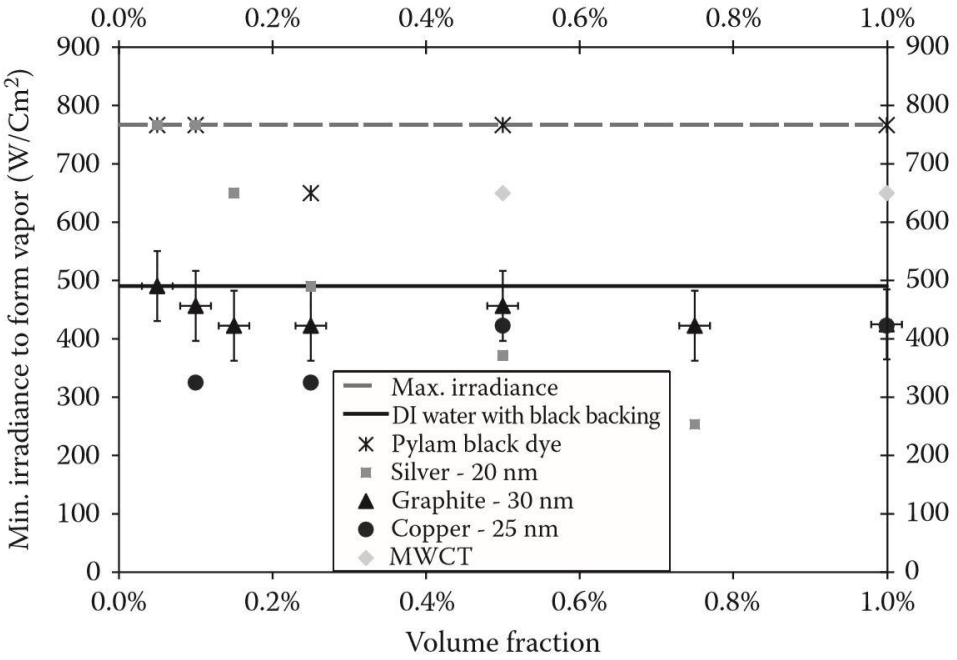

Figure 2.9 Minimum irradiance to generate vapour bubbles in different nanofluids at different concentrations [93].

Jin et al. [88] investigated the solar steam generation via gold nanofluids. The gold nanofluids were prepared by diluting a stock one, which synthesised by the one-step method, i.e., citrate reduction method. Using a Fresnel lens, the natural sunlight was concentrated to 220 Suns (1 Sun = 1000 W/m^2) and directed into the gold nanofluid, which contained in two concentric quartz tubes with vacuum in between to eliminate the convection losses. Three thermocouples were inserted in different depths in the light path. The experimental results showed that the nanofluid's temperature reached the boiling temperature (100^{o}C). The higher the nanofluid's concentration is, the faster boiling is. Also, the results showed that there is a temperature distribution within the nanofluid at the early stage of illumination. This temperature distribution was also verified by the simulation results. The main conclusion was; there is no evidence of the nanobubble generation around

the nanoparticles. The classical nucleation theory reveals a need for superheating of 2400^{o}C and the Young-Laplace equation shows that a high-pressure difference (~120 atm) across a bubble generated around 20nm particle is required. Furthermore, the simulation results of the classical heat transfer equation for a nanoparticle surrounded by water revealed negligible temperature difference (in 10^{-6} K) between the nanoparticle's surface and the surrounding water. The bulk temperature was ~59 ^{o}C after 60s of illumination as shown in Figure 2.10.

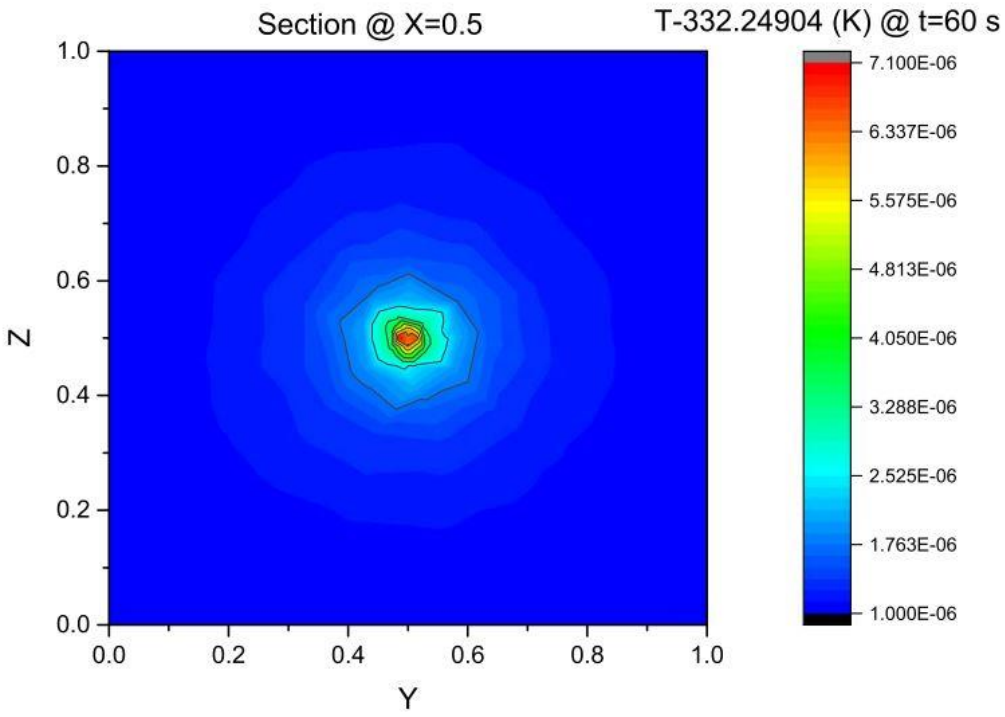

Figure 2.10 Temperature difference between a Au nanoparticle and surrounding water. The nanoparticle is in the centre of the cube and subjected to 220 Suns radiation [88].

Amjad et al. [98] experimentally investigated the volumetric solar heating and steam generation via gold nanofluids. Gold nanofluid was prepared by the

one-step method namely citrate reduction method. Different dilutions (0.008 wt.% (80 mg/l) - 0.04 wt.% (400mg/l)) were prepared by adding pre-calculated amount of DI water to the stock nanofluid. A solar simulator was used to produce 280 Suns. Three thermocouples were used to measure the temperature distribution within the light depth inside the nanofluid and another thermocouple was used to measure the temperature of the generated steam. The results revealed that the temperature of 0.016 wt.% (160 mg/l) gold nanofluid reached the boiling temperature (100^{o}C) after ~50s, 100s and ~160s along the nanofluid's depth. High efficiency (~95%) of steam generation was achieved at the saturated boiling stage of 0.04 wt.% (400 mg/l) gold nanofluid, while ~42% for DI water. The presence of nanoparticles in the condensate was checked relying on the UV-Vis test. The authors concluded that there were no particles in the condensate and they suggested this technique to produce clean water. The interesting finding is the condensation rate of the solar-generated steam. As shown in Figure 2.11, the condensation rate of the different gold nanofluids is almost constant after 120s. Assume the evaporation rate is equal to the condensation rate, the nanoparticles have negligible effects on the physio-thermal properties of water, which is understandable because of the low volumetric concentrations. The only task that the nanoparticle conduct is converting the solar radiation into thermal energy, increasing the temperature to the boiling temperature. The higher the nanoparticle is, the fast boiling of the free nanofluid surface layer is. However, it is not clear that why the condensation rate of solar-generated steam from the DI water is lower than the condensation rate of solar-generated steam from the gold nanofluids, even though the water temperature reaches the boiling temperature at ~60s.

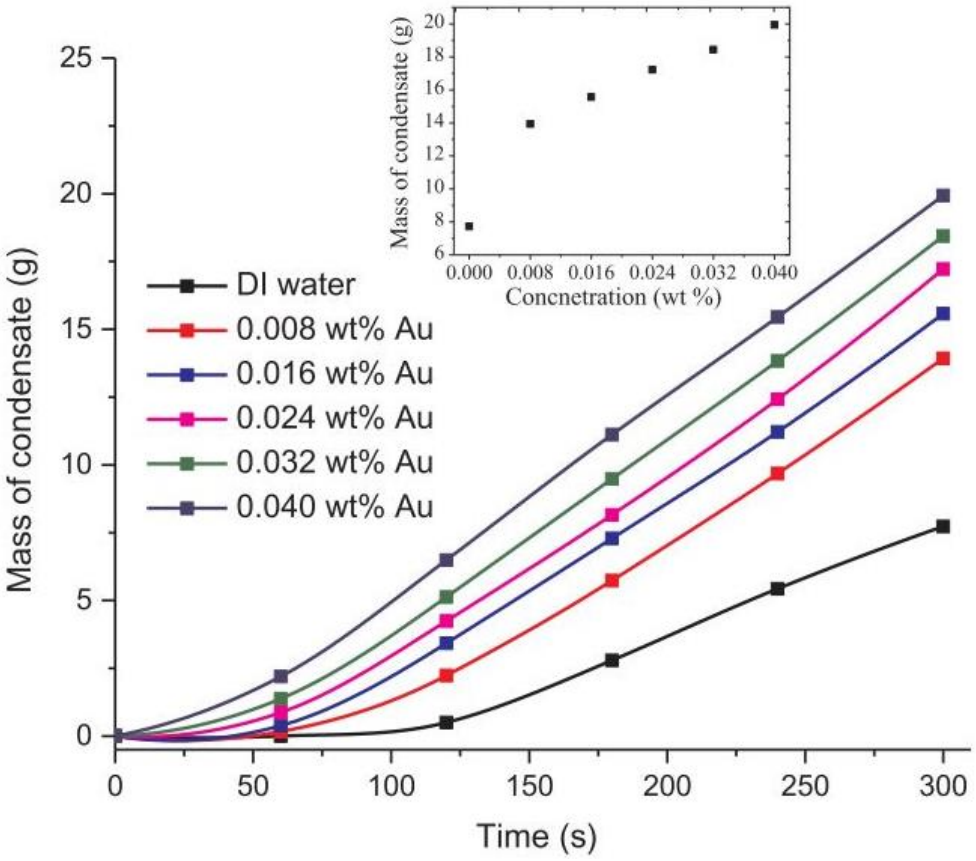

Figure 2.11 Condensation of solar-generated steam [98].

The effect of adding gold nanoparticles to graphene oxide nanofluid was investigated by Fu et al. [99]. 50 mg of graphene oxide powder, which was prepared by the oxidation process of powder flake graphite, were added to 100 ml of deionised water and sonicated until a homogenous dispersion was formed. Colloidal gold, which was synthesised by citrate reduction, was mechanically mixed with the graphene oxide nanofluid, i.e., the mixture was stirred for 30 min. The absorbance of gold, graphene oxide and graphene oxide-gold nanofluids was measured using a spectrophotometer through the wavelength range between 290 and 800 nm. The interesting finding was that the absorbance of graphene oxide-gold nanofluids was higher than of the graphene oxide nanofluid and the gold nanofluid. This result is against the

Beer's law, which indicates that the absorbance is linearly proportional to the concentration. Therefore, it is supposed that the mix of the two nanofluids will have an absorbance in between of the original values due to dilution. However, it is not clear what the gold nanofluid concentration was, and what the ratios of gold nanofluid to graphene oxide nanofluid were. Furthermore, the authors mentioned that "trace of gold nanoparticles (15.6 wt.%) in graphene oxide nanofluids could significantly improve the efficiency of solar vapour generation."; however, 15.6 wt.% represents 156000 mg/l. Such concentration cannot be trace category. Another point is that the experiments were conducted under the natural sunlight. It is difficult to eliminate the uncertainties accompanied by the natural sunlight, and this effect can be seen clearly as fluctuations in the steam pressure results. Therefore, it is difficult to judge that gold nanoparticles had a synergetic effect and improved the evaporation rate especially the mass reduction of the samples was recorded for only 10 min and during this period the temperature did not reach the steady-state value. The temperature rise figure showed negligible difference among the different nanofluids, i.e., graphene oxide, graphene oxide-gold 2.6 wt.%, 7.8 wt.% and 15.6 wt.%. This is in addition to the results of the mass loss showed negligible difference among the graphene oxide-gold 2.6 wt.%, 7.8 wt.% and 15.6 wt.% after 7 min of illumination.

Zhou et al. [100] generated steam efficiently under low intensities of artificial solar radiation via alumina nanoporous template coated by gold nanoparticles. A systematic procedure was performed to synthesize the optimum absorptive nanostructure through controlling the pores' size and the layer thickness of

the coating gold nanoparticle. An absorbance of ~99% of the radiation across the wavelength from 400nm to 10 μm and a steam generation efficiency of over 90% were achieved under 4 Suns illumination. The authors concluded that the evaporation rates of water with the optimised plasmonic absorber were 2.1 and 3.6 times the evaporation rate without the optimised plasmonic absorber at 1 and 4 Suns respectively.

A flexible thin gold porous membrane was synthesised by Bae et al. [101]. The average absorbance of this membrane was 91% across the wavelength range 400nm-2500nm. This membrane had the ability to localise the solar energy in a few micrometre-thick layer, generating water vapour with 57% efficiency at 20 kW/m^2. A xenon arc lamp with a filter (1.5 AM) was used to produce artificial solar radiation. The thin porous gold membrane was put on a hydrophilic microporous substrate to: firstly, provide mechanical support; secondly, float the membrane; and thirdly, to feed the membrane with water. The complex of the thin porous gold membrane and the microporous substrate was put on the surface of the water sample (20mm in diameter and 45mm in height). Using a digital mass scale and infrared camera, the mass reduction and the temperature of the water sample were recorded. The thermograms of the infrared camera showed the ability of the membrane on localising the thermal energy at the top and bottom of the water sample when the gold membrane was at the top and bottom of the sample respectively. The data of the evaporation rate as a function of the light intensity showed a continuous increasing as the light intensity was increasing.

The reviewed literature shows a growing interest in using gold nanoparticles as efficient photo-thermal conversion DASCs. Indeed, using gold nanoparticles enhances the harvesting of solar energy, converting it into thermal energy, but there is a clear lack in comparative studies that investigate the feasibility of using such expensive material, namely gold, rather than cheap materials such as carbon black. The comparison is needed in both the cost and the performance of different nanoparticles at the same operating conditions to achieve a fair conclusion.

2.5 Chapter Summary

From the literature review, one can conclude the following:

1- H_2O-LiBr absorption refrigeration systems are mature technologies. They are eco-friendly due to the use of water as a refrigerant instead of environmentally harmful ones such as CFCs, HCFCs and HFCs, which are commonly used in VCRSs. Furthermore, the peak electricity demand on national grids can be reduced significantly if VARSs are used instead of VCRSs since the former are driven thermally, while the latter are usually driven electromechanically. However, the VARSs are bigger and have lower COP than VCRSs.

2- The sun is a renewable and clean source of energy. Utilising the solar energy for cooling and heating is very attractive especially for cooling in summer where the time of peak electricity demand is during the availability of the solar energy at high intensities. However,

conventional solar collectors suffering from low efficiencies especially at high temperatures due to the heat losses.

3- Nanoparticles and nanofluids have attracted growing attention due to their fascinating characteristics. It has been suggested that seeding nanoparticles in working fluids can enhance their thermal properties such as thermal conductivity and heat transfer coefficient. Moreover, it has been suggested that the Brownian motion of the nanoparticles and the accompanied micro-convection can enhance the mass transfer. However, there is still a debate if the nanoparticles can enhance the heat and mass transfer or not due to the controversy results available in the literature.

4- Nanoparticles seeded in transparent working fluids can increase the photo-thermal conversion efficiency. Recently, due to the tunability of the LSP of the gold nanoparticles, increasing interest can be noticed to use gold nanofluids, hybrids and membranes. However, there is a shortage in comparative studies that compare the performance of the gold nanoparticles with other cheap ones at the same operating conditions such as the surrounding temperature and relative humidity, light intensity and nanoparticles concentration. Furthermore, blending nanofluids of different sizes and shapes of gold nanoparticles has been suggested to broaden the overall spectral absorption peak. However, there is no study comparing the photo-thermal performance of a blend of different nanofluids with the original ones at the same concentration. The need for the comparative study is due to the fact that blending different nanofluids at different portions leads to dilute the counterparts

as the overall volume increases, and according to Beer's law, the absorbance decreases as the concentration decreases.

Therefore, this thesis is trying to answer the research questions mentioned above as follows:

- In Chapter Three, a comparative study will figure out the best choice among expensive materials such as gold nanoparticles, non-expensive materials such as copper oxide nanoparticles and cheap ones such as carbon black nanoparticles. Also, examining the effect of blending different nanofluids having different peak absorbance at different wavelengths. Does this blending have a synergetic effect on the absorbance value of the hybrid nanofluid or not?
- In Chapter Four, a comparative study will investigate the solar vaporisation via gold and carbon black nanofluids, trying to figure out the feasible nanofluid and the mechanism. Is there a nanobubbles generation around the nanoparticles? Or is solar vaporisation due to the conventional mechanism, i.e., the kinetic energy of the water molecules?
- In Chapter Five, the effect of Brownian motion of the nanoparticles and the related micro-convection process on the steam absorption of the nanosolutions will be investigated using constant surface area and thickness of different samples. Also, the effective thermal conductivity and viscosity will be examined.

Chapter 3

PHOTO-THERMAL CONVERSION EFFICIENCY OF DIFFERENT NANOFLUIDS

3.1 Introduction

As reviewed in sec.2.3, direct absorption nanofluids have been introduced as effective alternatives to increase the solar thermal conversion efficiency. Hybrid nanofluids were also recently proposed to broaden the absorption spectrum. However, a comparative assessment of the performance of commonly used nanomaterials for solar energy harness is still lacking. Since both the aqueous lithium bromide solution and water has almost the same transparency (see Figure 3.1), the performance assessment of three different categorised aqueous nanofluids, i.e., gold (Au), copper oxide (Cu), carbon black (CB) nanofluids and their hybrids, in terms of photo-thermal conversion efficiency (PTE), specific absorption rate (SAR) and materials cost is demonstrated. Moreover, a mathematical model was built depending on Beer's law to predict the PTE enhancement.

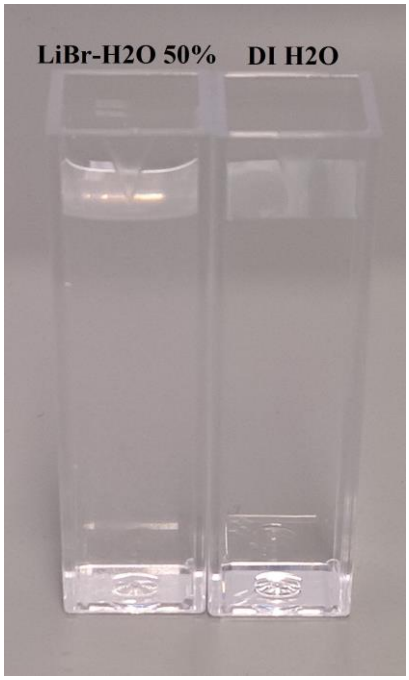

Figure 3.1 Transparency of de-ionised water and 50 wt.% aqueous lithium bromide solution.

3.2 Theoretical Part

It is empirically found that the reduction in intensity, dI, of light passing through a thin layer, dy, containing an absorbing species at molar concentration c (see Figure 3.2) follows the following equation [102], [103]:

$$dI = -\kappa c I dy \qquad 3.1$$

where κ is the proportionality coefficient.

Rewriting Eq. 3.1

$$\frac{dI}{I} = -\kappa c dy \qquad 3.2$$

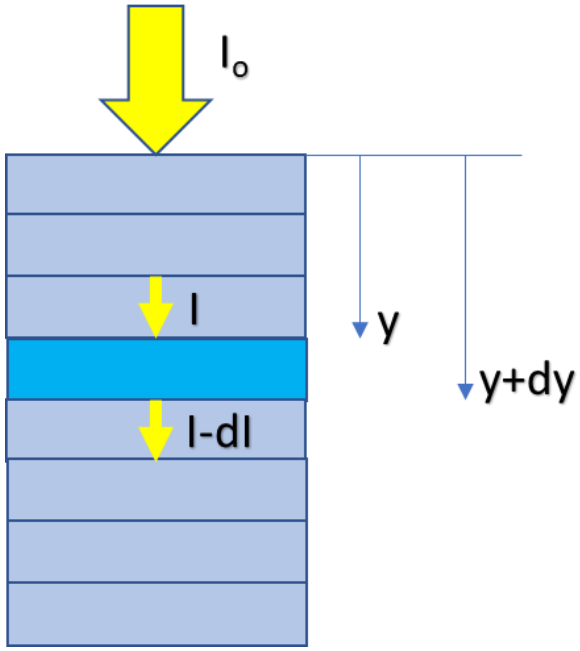

Figure 3.2 Light attenuation in absorbing medium.

Hence,

$$\int \frac{dI}{I} = -\kappa c \int dy \qquad 3.3$$

$$lnI = -\kappa cy + C \qquad 3.4$$

where C is the integration constant.

When $y = 0, I = I_o$, hence, $C = lnI_o$

Substituting in Eq. 3.4,

$$ln\frac{I}{I_o} = -\kappa cy \qquad 3.5$$

$$T = \frac{I}{I_o} = e^{-\kappa cy} = e^{-\alpha y} \qquad 3.6$$

where T is the spectral transmittance; I is the spectral transmitted light intensity @ y; α is the extinction coefficient and equals to κc .

Assuming that the nanoparticles are small enough so that the particle size parameter ($\beta = \frac{\pi D}{\lambda}$, where D is the nanoparticle's diameter and λ is the wave length) is much less than one, then the scattering effect can be neglected [68], [76], [104] and an energy equation can be written relying on the energy conservation law as:

$$I_{abs} = I_o - I \tag{3.7}$$

$$I_{abs} = I_o - I_o e^{-\alpha y} \tag{3.8}$$

$$\frac{I_{abs}}{I_o} = 1 - e^{-\alpha y} = 1 - T \tag{3.9}$$

$$\frac{dI_{abs}}{dy} = \alpha I_o e^{-\alpha y} = \alpha I_o T \tag{3.10}$$

Eq. 3.9 shows clearly that the absorbed energy is an exponential function of the extinction coefficient, which is a function of the nanofluid's concentration, and the length of the light path. Moreover, Eq. 3.10 shows that the rate change of the absorbed energy with respect to depth is a function of the incident light intensity in addition to the extinction coefficient and depth. A solution of Eq. 3.9 is shown in Figure 3.3 and the solution of Eq. 3.10 assuming unity extinction coefficient is shown in Figure 3.4. It is clear that the higher extinction coefficient is, the higher absorbed light intensity in a thinner volume of the nanofluid. Also, the higher incident light intensity is, the higher the rate of change of the absorbed light intensity with respect to the nanofluid's depth. Therefore, the nanofluid's temperature is expected to be heterogeneous as the extinction coefficient and the incident light intensity increases.

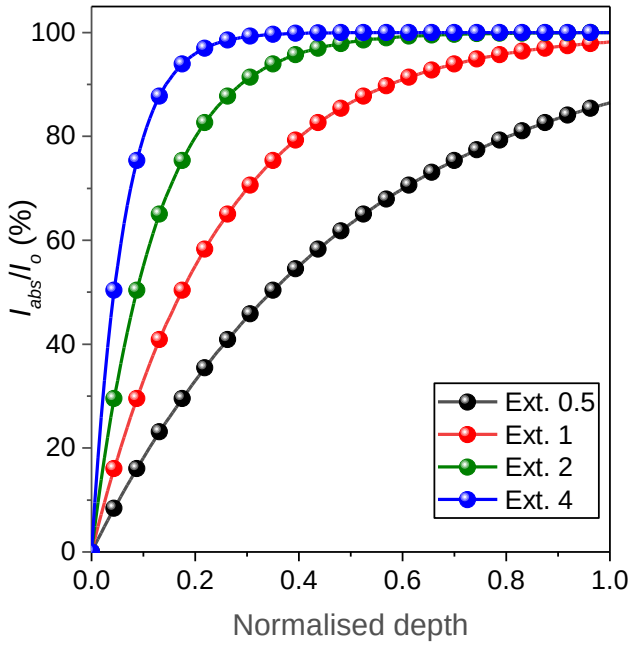

Figure 3.3 Percentage of the absorbed light intensity as a function of nanofluid's depth at different extinction coefficients.

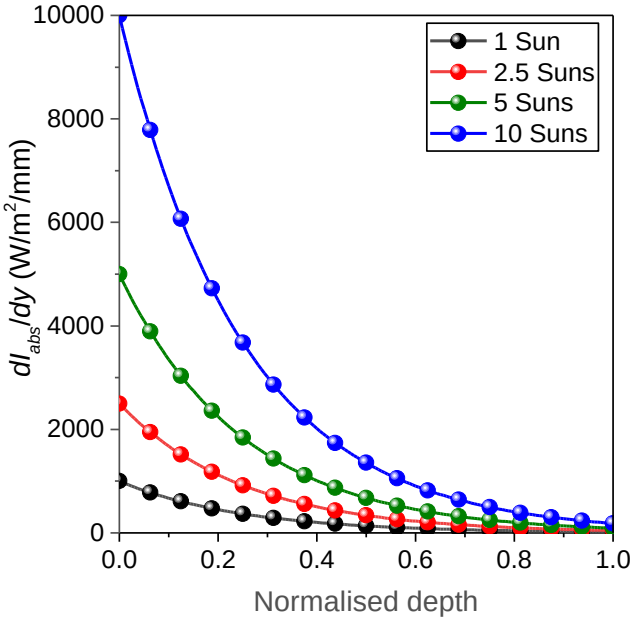

Figure 3.4 The rate change of the absorbed light intensity as a function of nanofluid's depth at different incident light intensities.

3.3 Experimental Part

3.3.1 Gold nanofluids preparation

In this study, gold (Au) nanofluid was synthesised by the citrate reduction method as reported by Chen and Wen [105]. Typically, 100 ml of 5 mM $HAuCl_4$ aqueous solution was mixed with 100 ml of 10 mM trisodium citrate aqueous solution. Then, the resultant mixture was heated to the boiling temperature until its colour became wine red. After that, the resultant was put into a sonication bath at 80 °C for 3 h. The synthesised gold nanoparticles were left for 24 h at the room temperature and then purified by the membrane dialysis method. In this process, the gold nanofluid was put in a membrane tube with a pore size of 2–3 nm in diameter to allow a smooth diffusion of ions and keep the gold nanoparticles inside the tube. The membrane tube was located in a beaker filled with DI water of 2000 ml and stirred by a magnetic stirrer. The DI water was changed twice a day for ten days.

3.3.2 Carbon black and copper oxide nanofluids preparation

Carbon black (CB) and copper oxide (Cu) nanofluids were prepared by the two-step method, i.e. by dispersing a certain amount of pre-synthesised nanopowder to a hosting liquid. CB nanopowder was purchased from Alfa Aesar (CAS# 1333-86-4, purity 99.9^{+}%, average particle size 42 nm, S.A. 75 m^2/g, bulk density 80-120 g/l and density 1.8-2.1 g/cm^3 at 20^{o}C). The Cu nanopowder was purchased from Sigma-Aldrich Corporation (CAS# 7440-50-8, purity 99.5^{+} %, average particle size 40-60 nm, density 8.94 g/cm^3 at 25^{o}C). Magnetic stirrer and overhead mixer were used to disperse CB and Cu nanopowders in DI water, i.e., 200 mg of CB nanopowder in 1 l of DI water

and 1000 mg of Cu nanopowder in 100 ml of DI water. It was found that dispersing both nanopowders was very difficult due to hydrophobicity. Later, a sonication probe (Fisher Scientific, 700 W power and 20 kHz frequency) was used to break down nanoparticles' aggregation and to disperse the particles in water. The procedure used by Retamal Marín et al. [106] was adopted, i.e., the amplitude was 100, the pulse mode was 2 s sonication: 2 s no sonication, and the sequence was 4 min sonication : 5 min cooling down the sample in tap water. Even high sonication power was consumed (1.5313 x 10^9 J/m^3), a complete separation of the phases, i.e., particles and water phases, happened as can be seen in Figure 3.5. Therefore, measures had to be taken to overcome this issue.

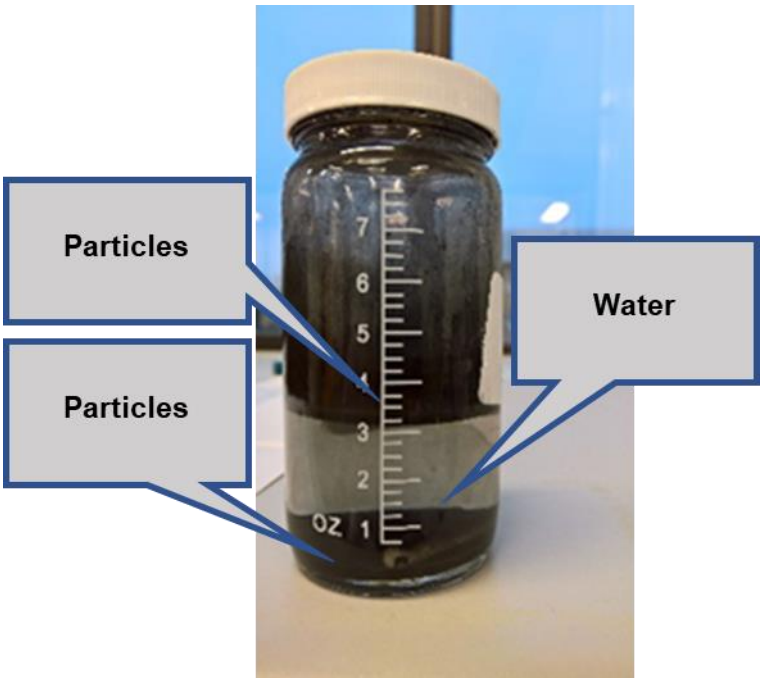

Figure 3.5 Cu particles separation after 15 min even high sonication energy density (1.5313 x 10^9 J/m^3) was consumed.

Appling surfactants can overcome the hydrophobicity issue. Surfactants, surface active agents, are molecules consisting of two main groups at least; hydrophilic and hydrophobic groups. The hydrophilic group is a polar or ionic portion, while the hydrophobic one is a non-polar portion of the surfactant molecule, usually a straight or branched hydrocarbon or fluorocarbon chain [107]. The hydrophilic portion (head) interacts strongly with water molecules through dipole or ion-dipole interactions, while the hydrophobic portion (tail) interacts weakly with water molecules. In other words, water molecules avoid contact with the hydrophobic tails. Consequently, these tails are squeezed out the water by accumulation at interfaces and aggregation in solution forming units referred to as micelles [107]. Adsorption of surfactants at interfaces, e.g., water/oil (w/o), water/air (w/a) and water/solid (w/s), has a reduction effect on the interfacial surface tension ($\gamma_{w/o}, \gamma_{w/a}, \gamma_{w/s}$). The higher the adsorbed surfactant is, the larger reduction in the interfacial tension. As a result, surfactants have a main role in colloid stability, e.g., emulsions and suspensions, and find many applications such as detergents, paints, cosmetics, pharmaceutical and oil industries [107], [108].

The non-ionic Spans and Tweens are the most used surfactants. Their suitability as food additives is approved and they have broad applications in cosmetics and pharmaceutical preparations. However, Spans are insoluble in water but soluble in most organic solvents. While Tweens are soluble in water [107]. Moreover, Tween 80 hydrophilic head has three OH branches (see Figure 3.6) which can play good rule in the dispersion process. For these

reasons, Tween 80 was selected to improve the wettability and disperse ability of the nanoparticles in water.

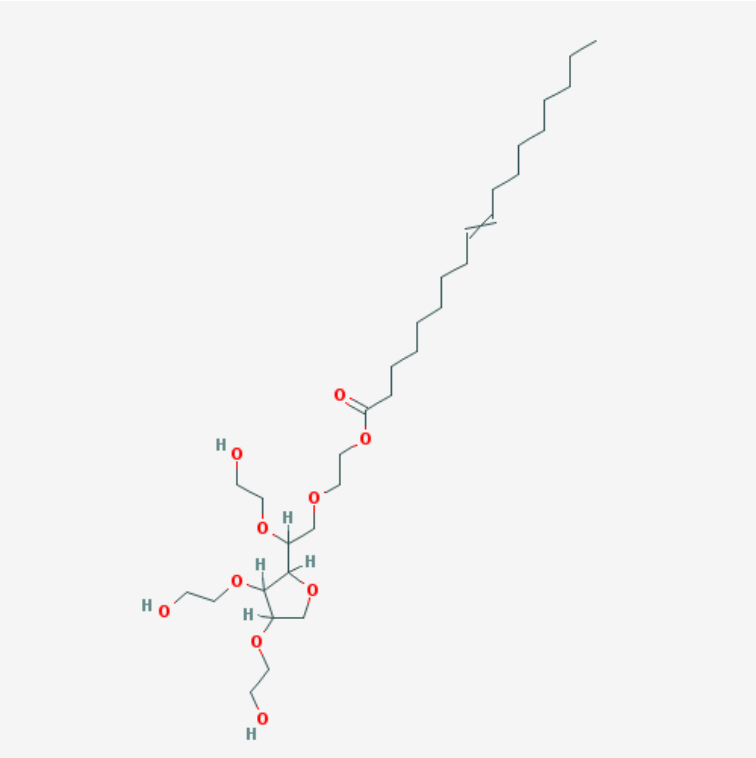

Figure 3.6 Tween®80 structure[1].

Tween®80 was purchased from Sigma-Aldrich (Mw 1310, CMC 0.012mM and ρ 1.06 g/ml). 530 mg of Tween®80 was dissolved in 1 l of DI water to prepare a solution of 0.404 mM. After that, 200 mg of the CB was added to the solution and the overall mixture was stirred for 1 hr using an overhead mixer at 2000 rpm. After foam separation as shown in Figure 3.7, well dispersed CB-H_2O was achieved. Then probe sonication was performed and size distribution measurements depending on the dynamic light scattering (DLS) were

1 https://pubchem.ncbi.nlm.nih.gov/image/imagefly.cgi?cid=443315&width=500&height=500

conducted to investigate the relation between the sonication energy and the size of nanoparticles' aggregates.

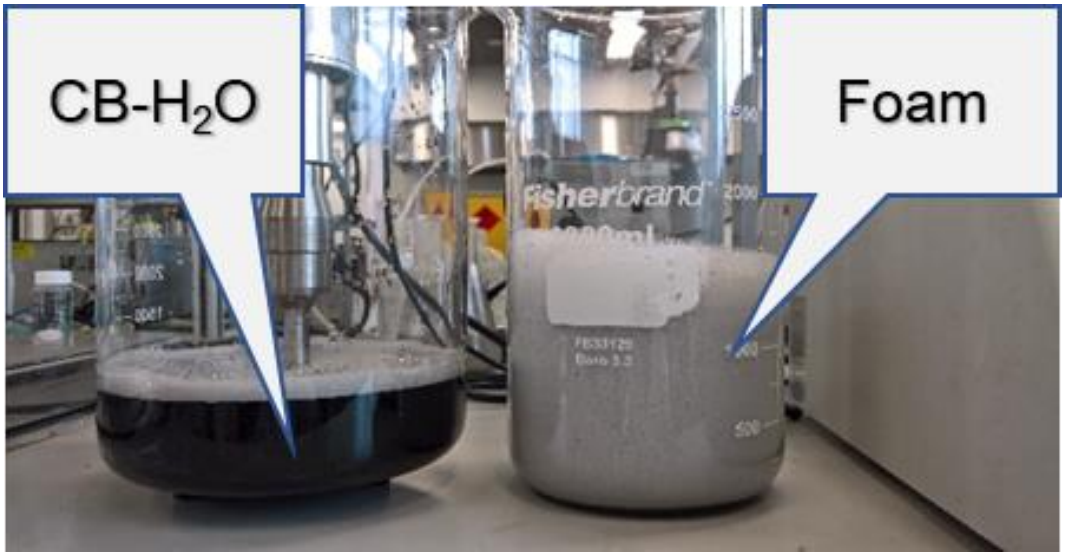

Figure 3.7 Aqueous CB nanofluid after mixing.

Ultrasonic energy is a common preparation technique for the characterisation of particle systems due to the widespread of the ultrasonic equipment. The high-power ultrasound leads to cavitation, which is a phenomenon related to the formation of bubbles filled with vapour and dissolved gases. These bubbles grow to a critical size to become unstable and finally implode. These implosions of the bubbles cause temperature peaks and violent micro-jets. Consequently, strong interactions between the micro-jets and the particles occur leading to defragmentation (size reduction) of the aggregates and agglomerates [106], [109].

Published research results show a power relationship between the average size of particles and the ultrasound energy as [106]:

$$Average\ size\ \propto (Energy)^{-b} \quad 0.1\ < b < 0.15 \qquad 3.11$$

However, analysis of our results shows some deviation with a power value of 0.16 as can be seen in Figure 3.8. The trend of particle size reduction raises questions: Is the ultrasound technique is effective to reach the minimum possible size (42 nm)? And is that minimum possible size reachable? However, Retamal Marín et al. [106] answered these questions. They concluded that the concept of reaching the complete dispersion with minimum size fails. Moreover, they demonstrated that samples subjected to a high sonication energy were contaminated due to the abrasion of the ultrasonic probe.

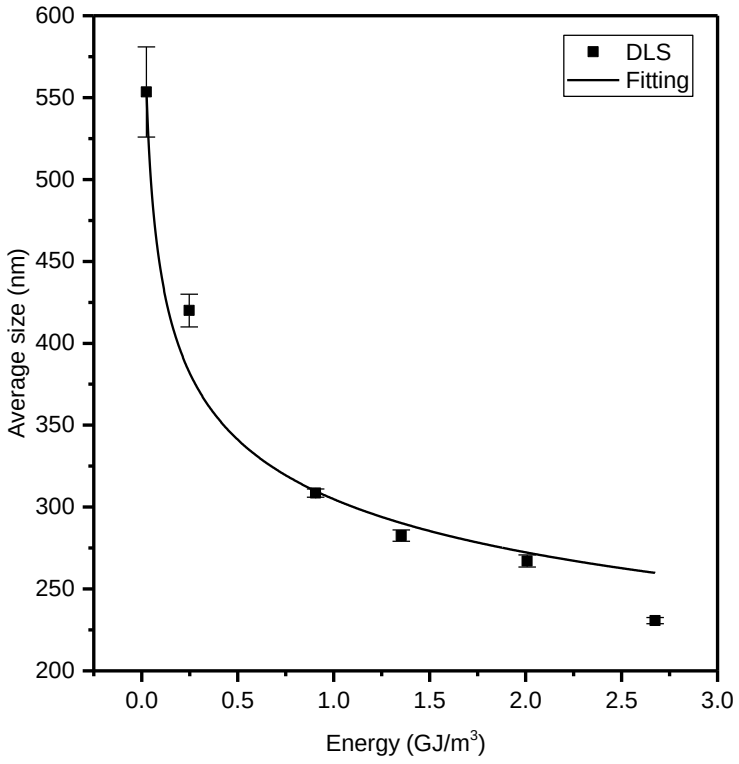

Figure 3.8 Particles' average size as a function of sonication energy per unit volume of the nanofluid.

After 24 hr of storing, sedimentation of CB was detected. Therefore, a stabilizing agent was required to overcome this issue. Gum Arab (GA), which is an edible natural polymer, was selected because GA has both hydrophilic and hydrophobic affinities. GA dissolves in water even at high concentrations producing relatively low viscosity compared with other gums [110]. Furthermore, GA has been used in many studies to prepare stable nanofluids. For example, Wang et al. [111] used GA to prepare a stable homogeneous aqueous suspension of MWCNTs. They found the optimum GA concentration was 450 mg/l (0.045 wt.%). However, Indhuja et al. [112] used a concentration of GA of 2500 mg/l (0.25 wt.%) to prepare stable MWCNTs aqueous suspensions. Boncel et al. [113] used GA as a stabilising agent to prepare different carbon-based nanofluids. They used 5000 mg/l (0.5 wt.%) GA-H_2O solutions for MWCNTs suspensions, while 10000mg/l (1 wt.%) for spherical carbon particles. Furthermore, Bandyopadhyaya et al. [114] demonstrated that GA is better than other dispersant agents such as SDS and CTAC. They succeeded to prepare a uniform ink-like dispersion of 500 mg/l (0.05 wt.%) SWCNTs in 2 wt.% GA aqueous solution. They reported that the dispersion was stable even after 3 months of storing on a shelf. Moreover, 0.5 wt.% GA reduces the surface tension and the interfacial tension ($\gamma_{w/a}, \gamma_{w/o}$) to 46.9 and 9.9 dynes/cm respectively [115].

Four different concentrations of GA, i.e., 2000 mg/l (0.2 wt.%), 10000 mg/l (1 wt.%), 20000 mg/l (2 wt.%) and 30000 mg/l (3 wt.%), in water were prepared. CB nanofluid (200 mg/l), which previously prepared, was mixed with the four

concentrations of the GA solutions by 1:1 ratio. As a result, four CB nanofluids were prepared as shown in Figure 3.9 :

#1 100 mg/l CB, 15000 mg/l (1.5 wt.%) GA

#2 100 mg/l CB, 10000 mg/l (1 wt.%) GA

#3 100 mg/l CB, 5000 mg/l (0.5 wt.%) GA

#4 100 mg/l CB, 1000 mg/l (0.1 wt.%) GA

The samples were stable even after a week from the first preparation and sample #1 (1.5 wt.%) GA was stable after 4 weeks, as shown in Figure 3.9. However, shaking the samples by hand could homogenise the suspension easily.

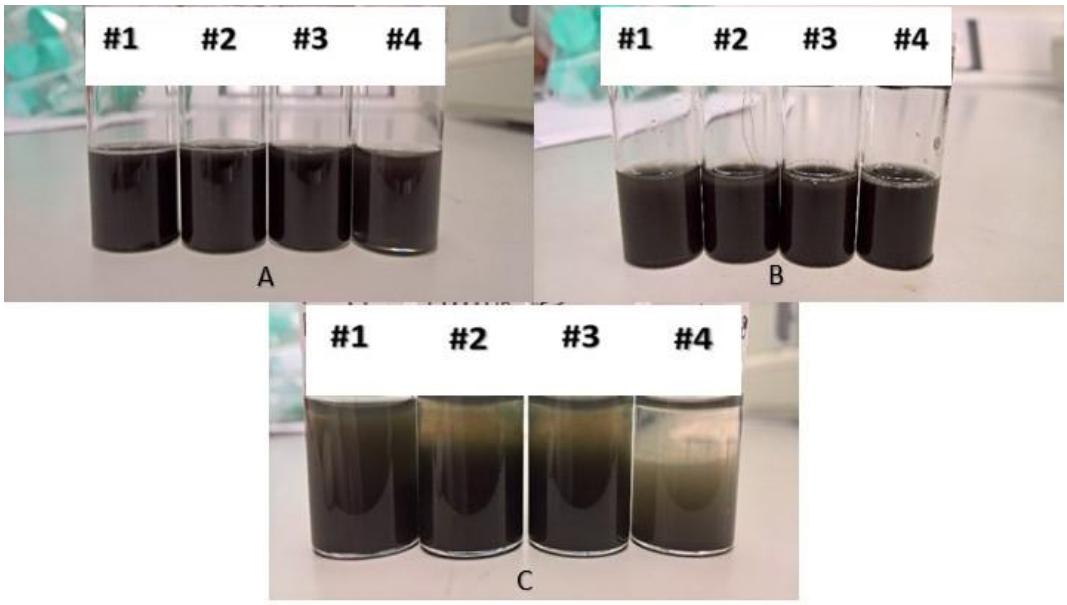

Figure 3.9 Aqueous suspensions of 100 mg/l CB at different GA concentrations. #1, #2, #3 and #4 are 1.5%, 1%, 0.5% and 0.1% GA respectively. (A) just after preparation, (B) a week after and (C) 4 weeks after preparation.

For Cu aqueous suspensions, the same procedure used in preparation of CB nanofluids was adopted.

3.3.3 Nanofluids characterisation

After the preparation stage of the nanofluids, i.e., Au, CB and Cu nanofluids as shown in Figure 3.10, the characterisation processes were started. A flame atomic absorption spectrometer (AAS) was used to measure the concentration of the Au nanofluid. Atomic absorption spectrometry technique relies on the intrinsic absorption of atoms in their gaseous phase. The metal solutes must be completely dissolved in a solution form. Therefore, aqua regia (a mixture of HNO_3 and HCl in a ratio of 1:3) was used to dissolve the Au nanoparticles into a homogenous solution. The AAS atomises the Au solution into small aerosols (droplets) before passing into a flame, which volatiles the aerosols generating the metal atoms in their gaseous phase. The AAS measures the absorption of these atoms, which depends on the metal concentration, compares the results with standard data, and calculate the metal concentration. The concentration of the stock Au nanofluids was determined as 250 mg/l.

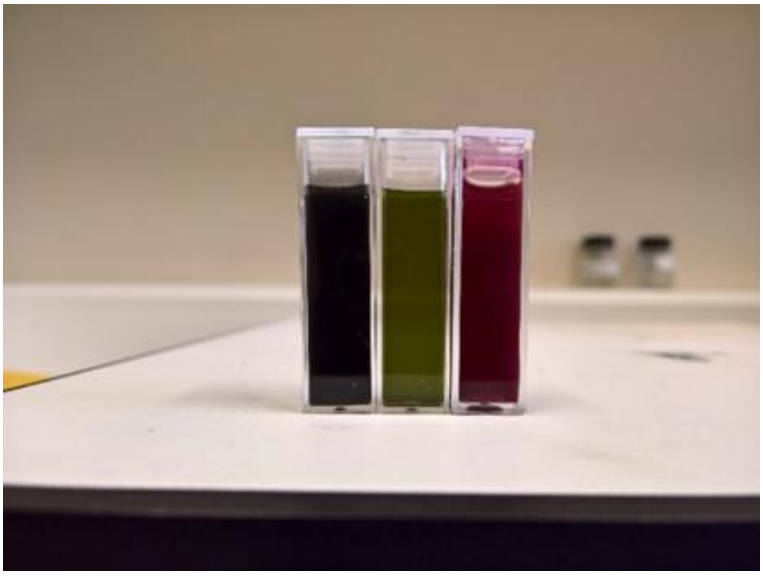

Figure 3.10 A photo of the nanofluids: Au nanofluid on right, Cu nanofluid in middle, and CB nanofluid on left.

The Zeta-potential and particle size distribution of the different nanofluids were measured by a Malvern Zetasizer (NanoZS90 5001). The Zeta-potential measurement bases on measuring the velocity of the particle using a laser Doppler electrophoresis technique when an electrical field is applied on a sample. Knowing the electrical field, particle velocity, viscosity and dielectric constants enable Zeta-potential calculation [116]. The measured Zeta-potentials were (- 45.7 ± 6.01 mV), (- 51.1 ± 7.08 mV) and (- 32.3 ± 4.66 mV) for Au, Cu and CB nanofluids respectively, which reveals good stability [117], [118]. The particle size distribution measurement depends on the Dynamic Light Scattering (DLS). The instrument measures, for short time interval (in microseconds), the light scattering due to the Brownian motion of suspended particles from a laser (e.g., 633 nm) that passes through the suspension. The measured fluctuations in intensity of the scattered light depend on the particles' size. The smaller the particle is, the faster Brownian motion, resulting

in more sharp fluctuations in the light intensity [116]. The size distribution of the three nanofluids, i.e., Au, Cu and CB nanofluids, are shown in Figure 3.11, Figure 3.12, and Figure 3.13 respectively. The results show polydispersions of the nanofluids especially for Au and Cu nanofluids. However, size distribution by number shows better results. That is due to the scattering light intensity depends on the sixth power of the particle diameter. For instance, a particle of a diameter of 100 nm has light scattering change 10^6 higher than a particle of the diameter of 10 nm. That means few large particles share a high percentage of the total scattering light. This is the case with Au and Cu nanofluids.

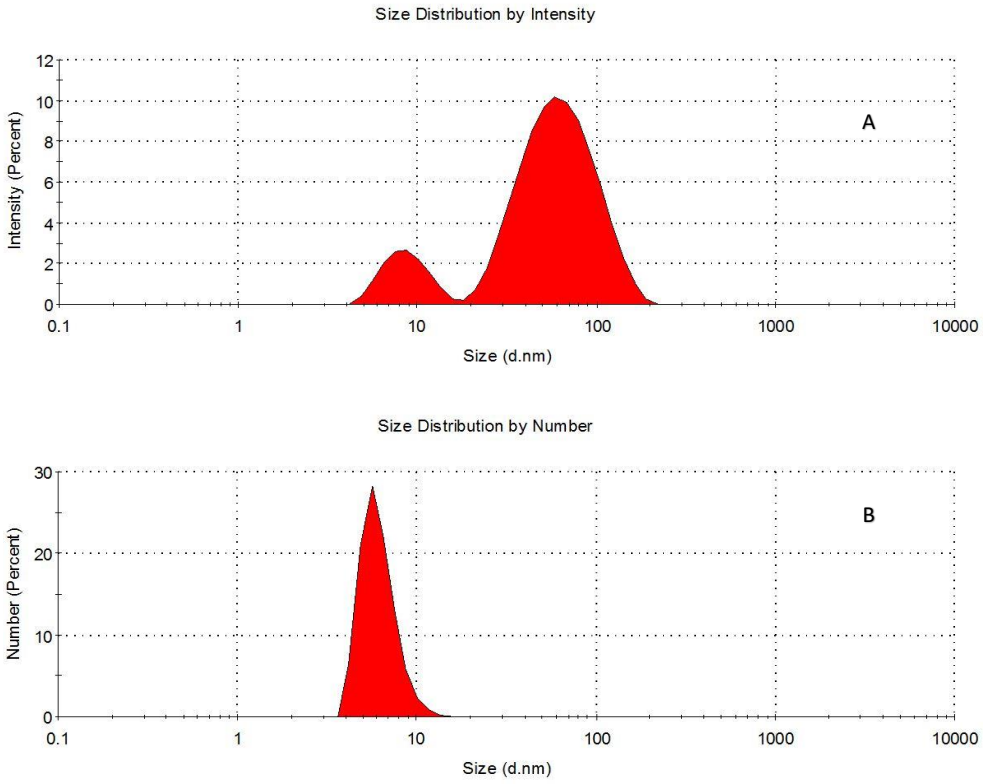

Figure 3.11 Size distribution of Au nanoparticles by (A) intensity and (B) number.

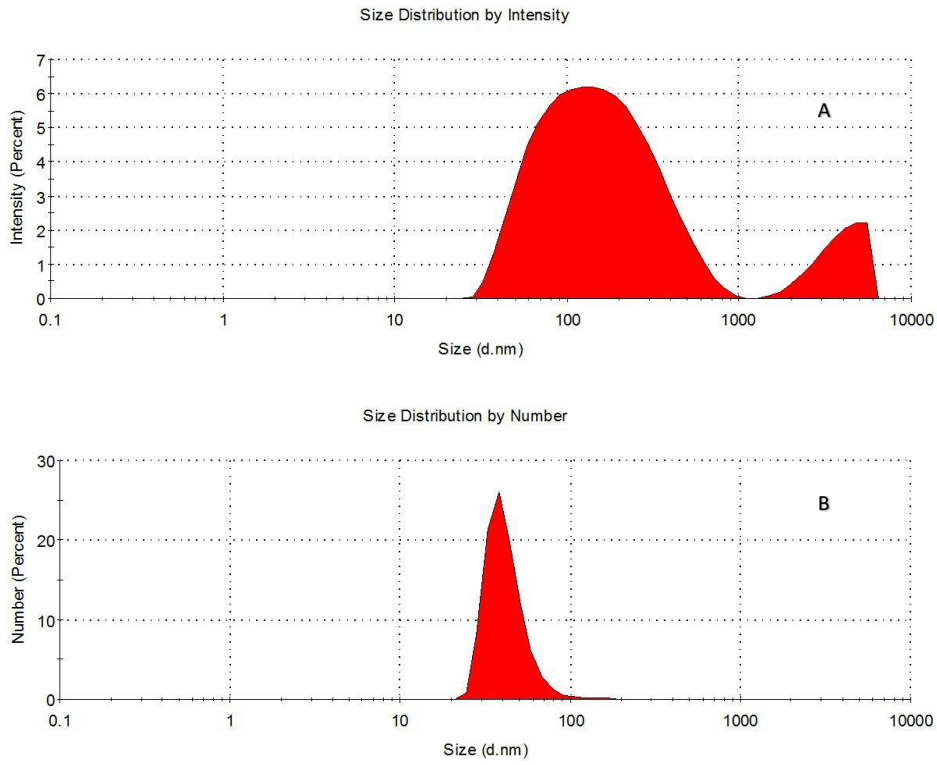

Figure 3.12 Size distribution of Cu nanoparticles by (A) intensity and (B) number.

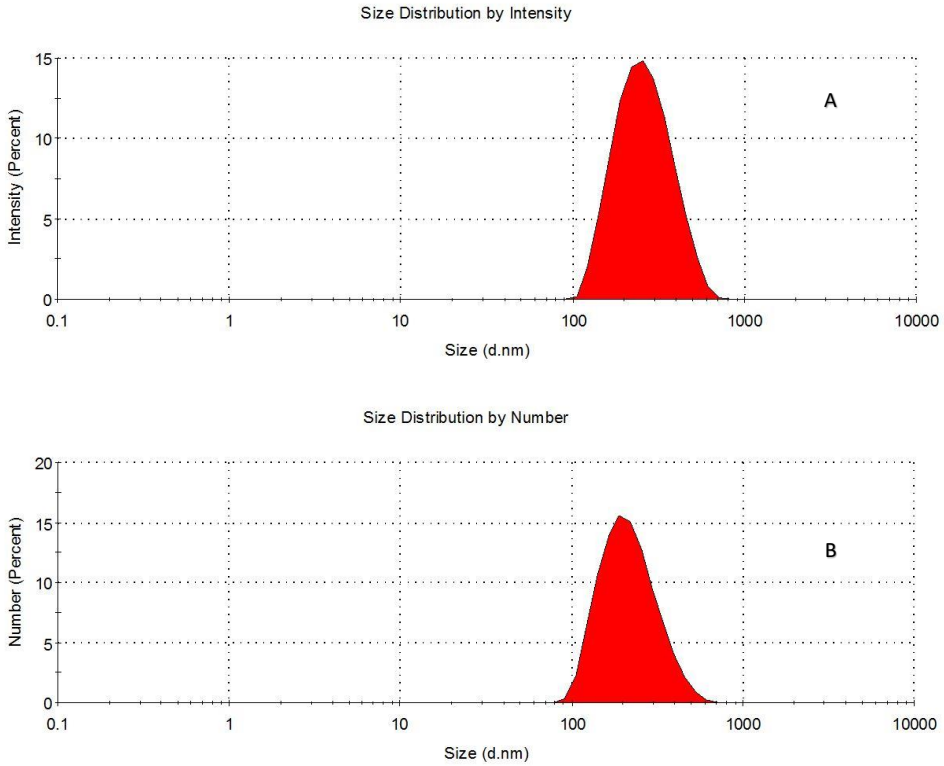

Figure 3.13 Size distribution of CB nanoparticles by (A) intensity and (B) number.

A transmission electron microscope (TEM, FEI Tecnai TF20) was used to examine the shape and size of the nanoparticles. The synthesised Au nanoparticles had different shapes (spherical, oval, and triangular) and sizes (small and large), as shown in Figure 3.14 (A). While big clusters of Cu and CB nanoparticles can be seen in Figure 3.14 (B) and (C). The TEM results interpret the DLS results well.

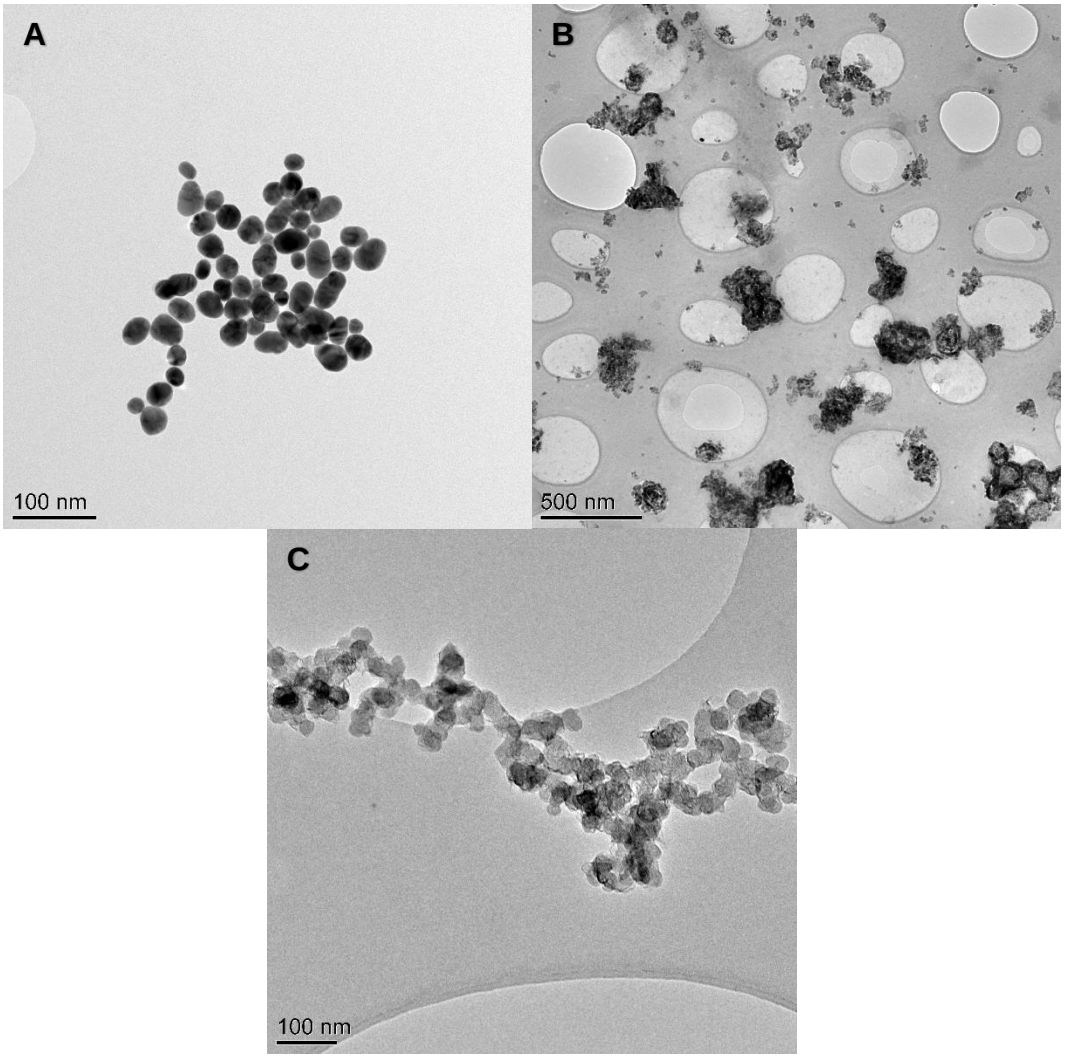

Figure 3.14 TEM graphs of (A) Au, (B) Cu and (C) CB nanofluids.

A Spectrophotometer (UV-1800, SHIMADZU) was used to investigate the stability and to measure the absorption capability of the prepared nanofluids. As the absorbance of a nanofluid depends on the size and shape of the nanoparticles, the spectrophotometer can be used to identify the status of nanoparticle aggregation [118]. Negligible changes was detected by the absorbance of the nanofluids for the freshly made and those stored for one-week. The absorbance results are presented in Figure 3.15, which reveal an excellent agreement with Beer's law, indicating a linear relationship between absorbance and solution concentration. It is clear that gold nanofluids have good absorbance in the range 300-600 nm wavelength and the peak value is around 528 nm, which is due to the local surface plasmon resonance, while the peak value of the absorbance of the copper nanofluids is around 740 nm. However, the absorption capability of the carbon black nanofluids is better than the gold and copper nanofluids over the whole spectrum.

3.3.4 Photo-thermal conversion

The photo-thermal conversion experimental setup is shown in Figure 3.16. A sun simulator (ORIEL® Sol3A™, Xenon Arc Lamp, CLASS AAA SOLAR SIMULATOR) was used as a light source to minimise the uncertainties under direct sunlight. This sun simulator provides a radiation spectrum matches the solar spectra, and the intensity can be varied by using suitable filters. This device is certified to IEC 60904-9 2007 edition, JIS C 8912 and ASTM E 927-05 standards. The performance parameters of the sun simulator are; spectral match between 0.75 – 1.25%, special non-uniformity < 2% and temporal instability < 0.5%.

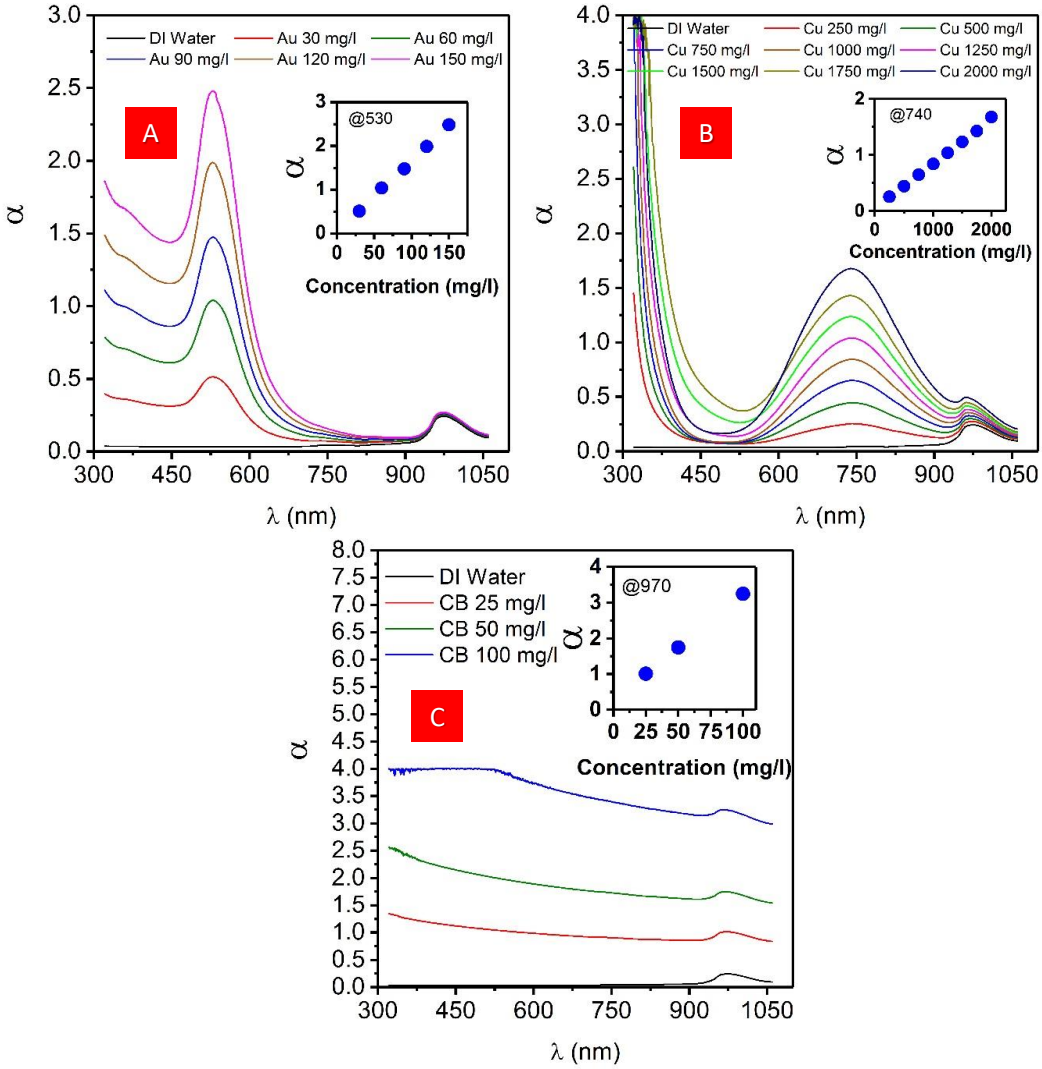

Figure 3.15 Spectral absorbance of different concentrations of nanofluids. The insets show the linear relationship between absorbance and concentration. (A) Au, (B) Cu, (C) CB nanofluids.

It has been shown in Figure 3.4, to make the temperature of the sample as homogenous as possible, two measures are required; firstly, the sample must be as thin as possible, and secondly, the incident light intensity must be as low as possible. Therefore, by using a precise micro-pipette, a 3 ml sample was put in a Petri dish (35 mm diameter) to get on a thin layer of the nanofluid (~3 mm) to minimise the temperature gradient within the sample. The Petri

dish was located on a hollow transparent light-weight holder in the centre spot of the solar simulator.

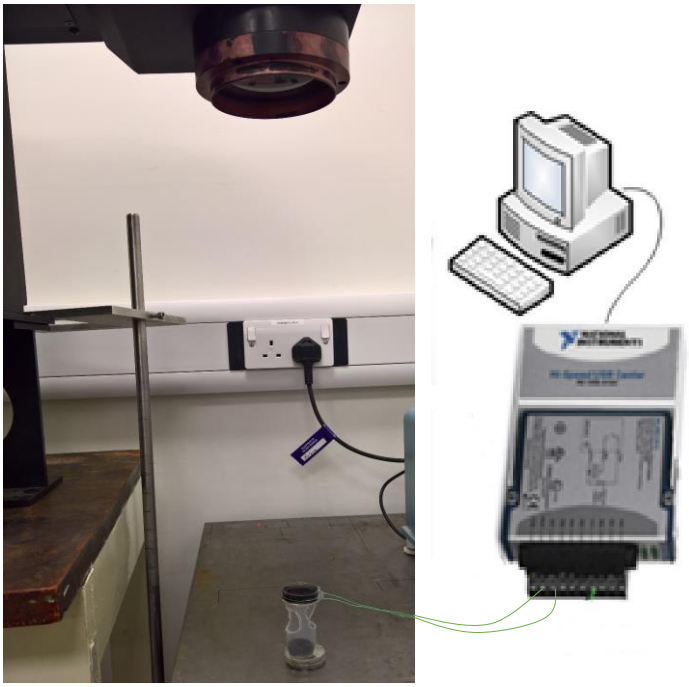

Figure 3.16 Experimental setup for the photo-thermal conversion tests.

A K-type thermocouple (Omega 5TC-TT-K-36-36, a diameter of 0.13 mm and an uncertainty of ±0.5 K) was used to measure the temperature of the sample at ~1.5 mm from the base of the Petri dish. The bulk temperature data were recorded every 30 seconds to a PC via data acquisition hardware under the LabVIEW environment. Preliminary tests with five thermocouples located at different positions on the bottom of the Petri dish showed that the space variation of the sample temperature was negligible as shown in Figure 3.17, which reveals that the solar simulator generates uniform light intensity. Furthermore, by using two thermocouples, one is just under beneath the sample level and the other at the bottom of the sample, the highest

temperature difference was less than 0.5 K for the highest concentration sample. Therefore, using one thermocouple located at the centre of the sample is very reliable. A repeatability test was performed using one sample and the standard deviation was ≤0.5 K (see Figure 3.18). This high repeatability was due to the use of Class AAA solar simulator, high-quality thermocouples and well-controlled laboratory environment. Therefore, one test for each sample was performed for the remaining samples.

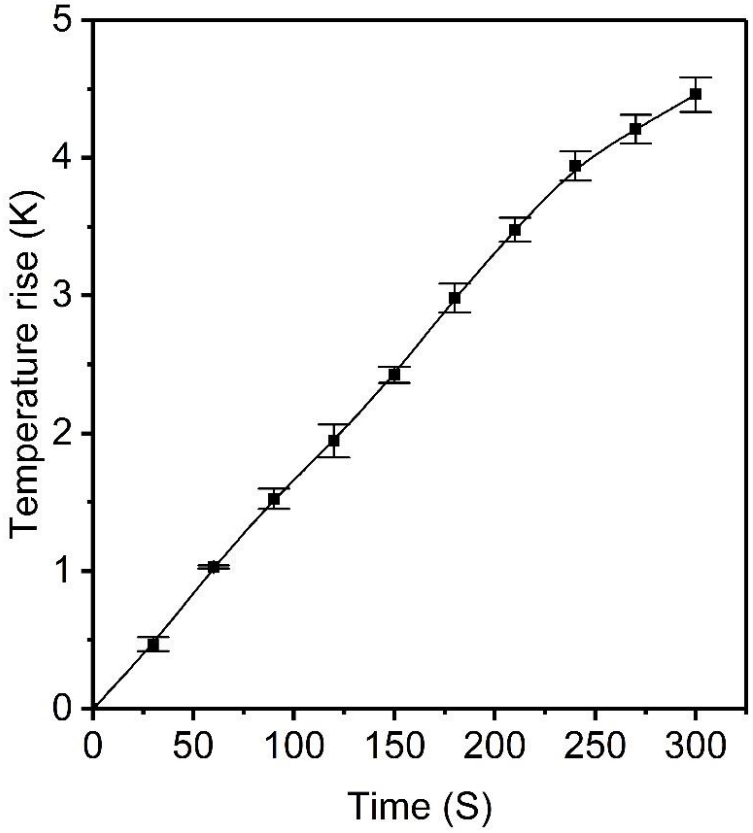

Figure 3.17 Average temperature rise of a water sample using 5 thermocouples at different positions on the base of the Petri dish.

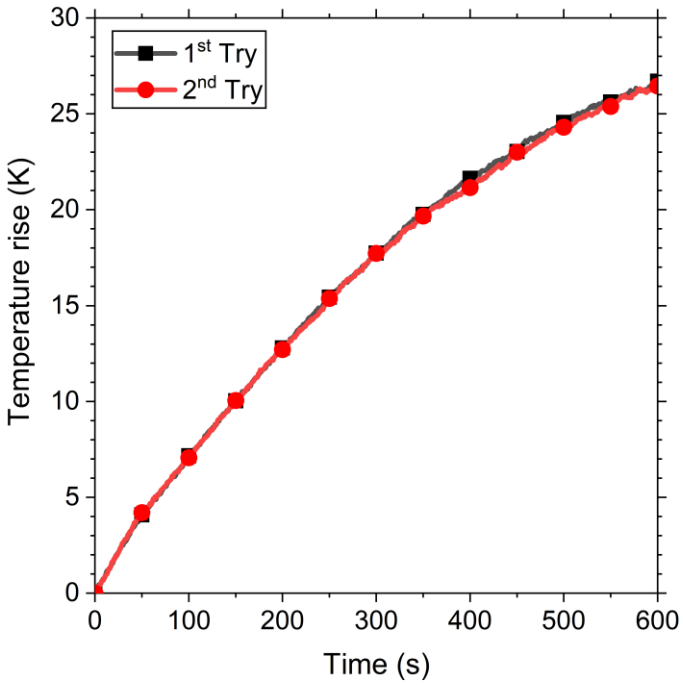

Figure 3.18 Repeatability test of the photo-thermal conversion.

3.3.5 Results and discussion

The nanofluid samples were subjected to 1000 W/m^2 radiation from the solar simulator for 300 s during which the temperature was being recorded. The photo-thermal conversion efficiency is defined as the ratio between the energy stored in the nanofluid and the total incident radiation:

$$PTE = \frac{\left(c_w m_w \Delta T_w + c_{np} m_{np} \Delta T_{np}\right)/\Delta t}{I_o A} \qquad 3.12$$

where c_w and c_{np} are the specific heat of water and the nanoparticles; $m_w$and $m_{np}$are the mass of water and the nanoparticles respectively; ΔT_w and ΔT_{np} are the water and nanoparticles temperature rise in the Δt time interval; I_o is the incident radiation intensity; and A is the illumination area of the nanofluid. The temperature difference between the nanoparticles and the hosting fluid (water) is negligible for low intensity continuous radiation [77], [119], and the

nanoparticles mass is negligible comparing to the hosting fluid mass. Therefore, 3.12 can be re-written as:

$$PTE \approx \frac{c_w m_w}{I_o A} \frac{\Delta T_{nf}}{\Delta t} \qquad 3.13$$

where ΔT_{nf} is the temperature difference rise of the bulk nanofluid.

The temperature difference and photo-thermal conversion efficiency (PTE) curves are shown in Figure 3.19 for Au, Cu and CB nanofluids respectively. It is evident that the temperature difference rise for each nanofluid increases as the time increases. Also, it is clear that ΔT_{nf} increases as the nanoparticle concentration increases. This is due to the enhancement of the water absorption of the radiation by the nanoparticles. Returning to Eq. 3.13, the PTE is proportional to the ratio ($\frac{\Delta T_{nf}}{\Delta t}$), or in other words, PTE is a function to the rate change of the temperature. Thus, the PTE decreases as the time increases until reaching a steady state value, as shown in Figure 3.19.

Due to the low intensity of the radiation and negligible effect of the length of the light path within the sample (sample thickness is ~ 3mm), and according to the Beer's law, which indicates that absorbance of a sample is linearly proportional to its concentration, it is expected that ΔT_{nf} is linearly proportional to the nanoparticle concentration. Indeed, that is well presented in Figure 3.20. It is clear that the rate change of the temperature rise with respect to the concentration increases as the time increases. This is because more radiative energy is captured and converted to thermal energy with time. As a consequent, the PTE increases linearly as the concentration of the nanoparticle increases, as shown in the inset of Figure 3.20.

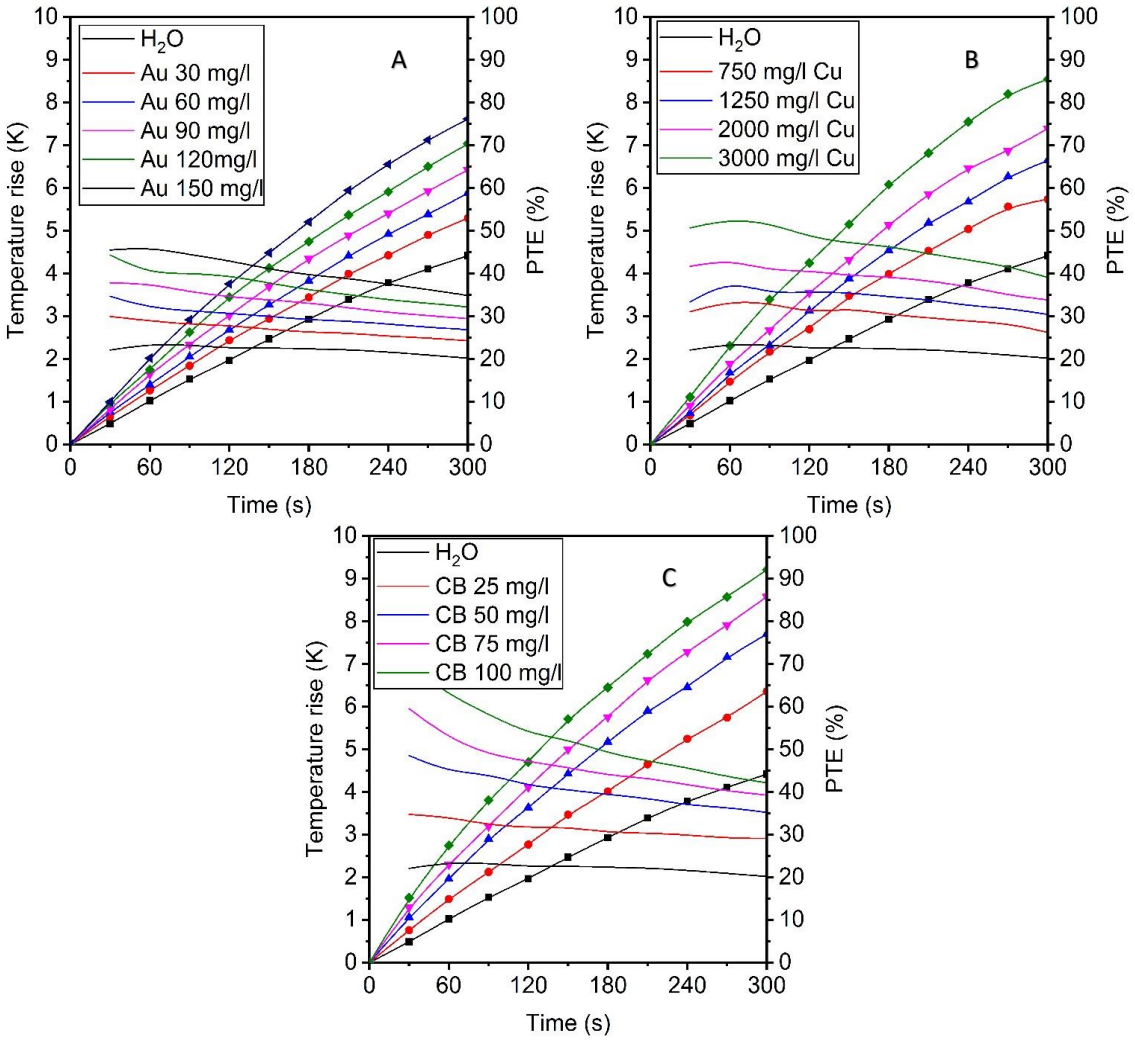

Figure 3.19 Temperature rise and photo-thermal conversion efficiency variation with time (A) for Au nanofluids and water, (B) for Cu nanofluids and water, and (C) CB nanofluids and water (solid lines represent PTEs and symbol-lines represent temperature rise).

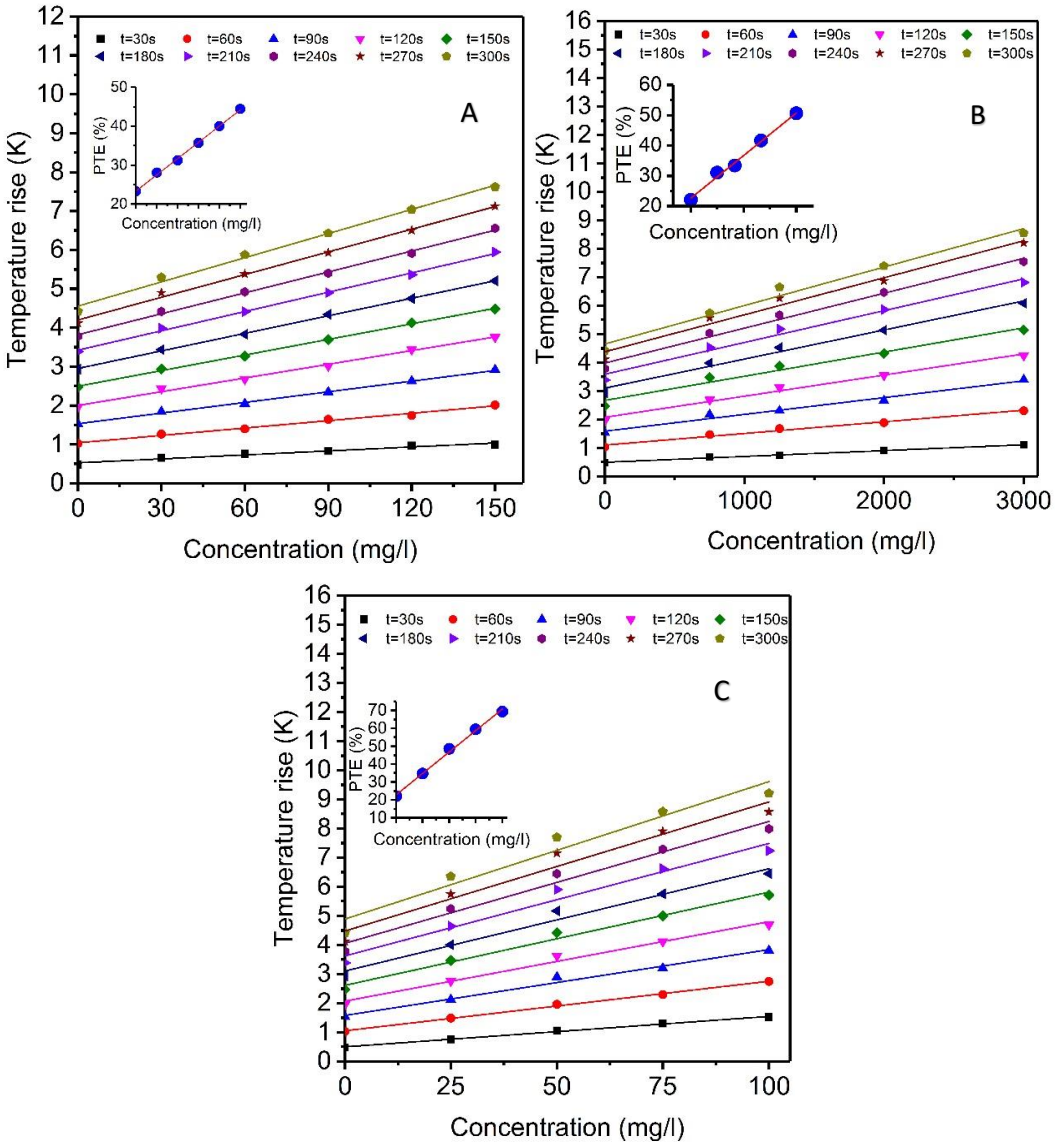

Figure 3.20 Temperature rise of a nanofluid as a function of its concentration at different time steps. The symbols represent the experimental data and lines represent the trend lines. The inset shows the photo-thermal conversion efficiency as a function of the concentration of (A) Au nanofluids, (B) Cu nanofluids, (C) CB nanofluids.

Practically, the improvement in the PTE of nanoparticles seeded working fluid comparing to the PTE of the hosting fluid is the fruit. This is the percentage enhancement of the PTE, which can be written as:

$$Enhancement = \frac{PTE_{nf} - PTE_w}{PTE_w}.100\% \qquad 3.14$$

A comparison between the Au and Cu nanofluids is presented in Figure 3.21. Obviously, the higher the nanoparticle concentration, the higher the photo-thermal conversion enhancement is. The maximum enhancement for Au nanofluid is ~72% at 150 mg/l concentration, and for Cu nanofluid is ~ 100% at 3000 mg/l. However, it seems that the PTE of 60 mg/l Au nanofluid approximately equal to 750 mg/l Cu nanofluid, 90 mg/l Au nanofluid approximately equal to 1250 mg/l Cu nanofluid, and 150 mg/l Au nanofluid is equal to 2000 mg/l Cu nanofluid.

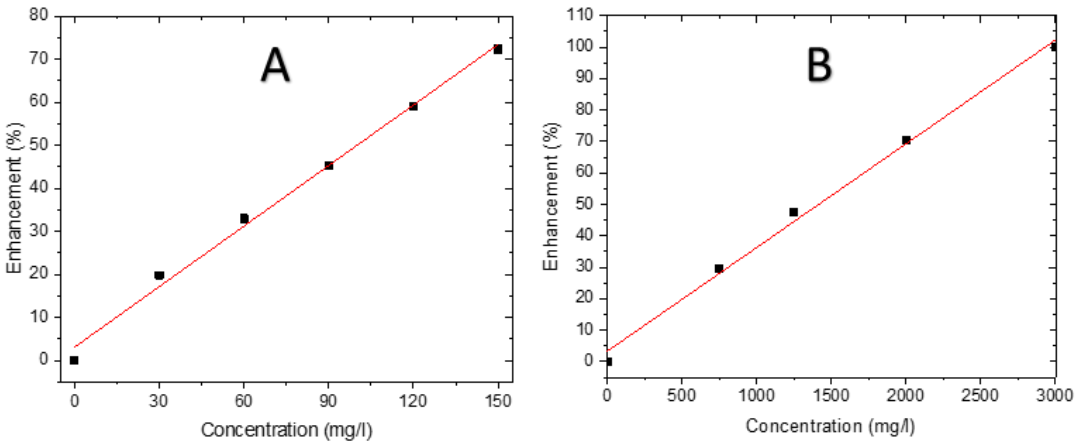

Figure 3.21 Photo-thermal conversion efficiency enhancement for: (A) Au, (B) Cu nanofluids.

Blending different plasmonic nanofluids with different absorption peaks was suggested by Cole and Halas [81], Lee et al. [82], and Jeon et al. [80] to improve the radiative absorption with broader absorption peaks. However, none of them compared the PTE of the hybrid nanofluid with that of the original nanofluids under the same concentration. In this work, hybrids from blending Au (absorption peak at ~528 nm wavelength) and Cu (absorption peak at ~740 nm wavelength) were prepared. Firstly, 1 ml Au nanofluid was blended with 1 ml Cu nanofluid, and then an absorbance spectrum test was performed for the hybrid. The results are shown in Figure 3.22. Indeed, the width of the absorbance peak became broader for the hybrid, but the absorbance value apparently became lower. It is logical because mixing different nanofluids together leads to the dilution of the original nanofluids due to the increase in the overall volume of the hybrid. For instance, in a hybrid of 1 ml of Au nanofluid with 1 ml of Cu nanofluid, the concentration of Au and Cu nanoparticles becomes half of the original (i.e., this is true if there is no reaction and/or aggregation between the blended nanofluids). Good agreement was found between the absorbance spectrum of the hybrid measured by the spectrophotometer (experimental) and the average absorbance of the original nanofluids (theoretical). Such results were quite different from what reported earlier [81], [82]. Though a high solar collector efficiency was reported by using a hybrid in Jeon's experiment (~71%) [80], the result is misleading due to a nearly doubled hybrid particle concentration used.

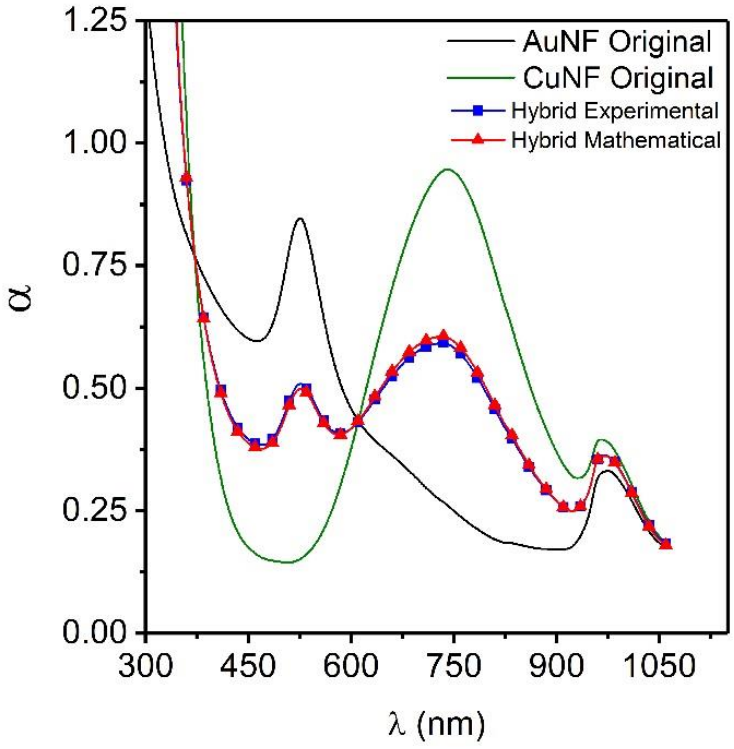

Figure 3.22 The absorbance spectrum of Au, Cu and a blend of 1:1 nanofluids.

To check this thermally, photo-thermal conversion tests were conducted for three hybrids. These hybrids were prepared by mixing equal portions of Au and Cu nanofluids that showed approximately the same PTE enhancement (i.e., 60 mg/l Au nanofluid with 750 mg/l Cu nanofluid, 90 mg/l Au nanofluid with 1250 mg/l Cu nanofluid, and 150 mg/l Au nanofluid with 2000 mg/l Cu nanofluid respectively). The results are shown in Figure 3.23, and it is clear that the temperature rise curves are almost identical for the hybrids and their original ingredients. Using hybrid nanofluids does not produce any additional benefits. Comparing to other materials, carbon-based nanofluids have the most desired absorption spectrum (see Figure 3.15 (C)). With its super absorbance at low concentrations (less than 100 mg/l), CB nanofluids appear

the most feasible choice for solar energy harvesting, where an enhancement of ~125% was achieved by 100 mg/l CB nanofluid, as shown in Figure 3.24.

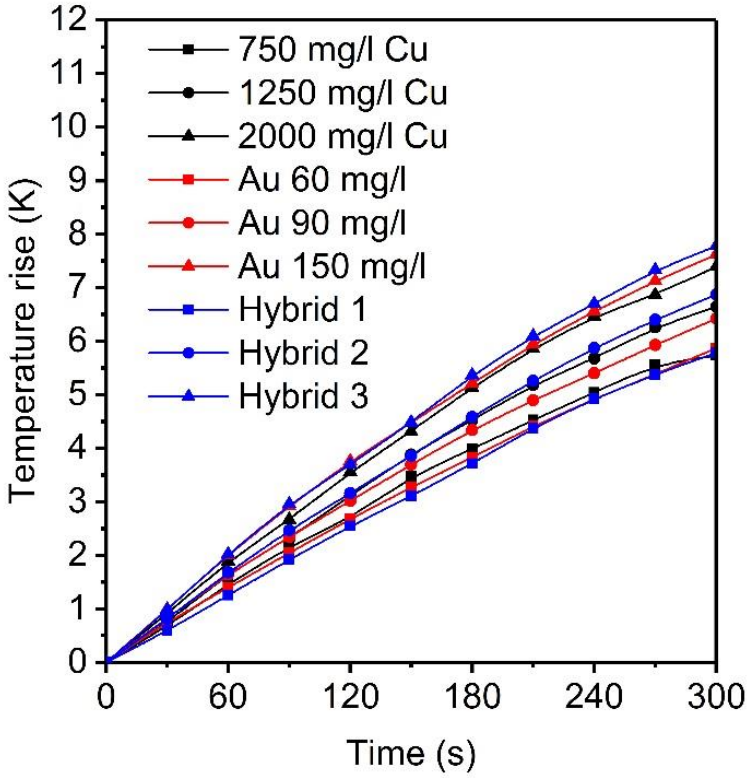

Figure 3.23 Temperature rise variation with time of Au and Cu nanofluids and their hybrids.

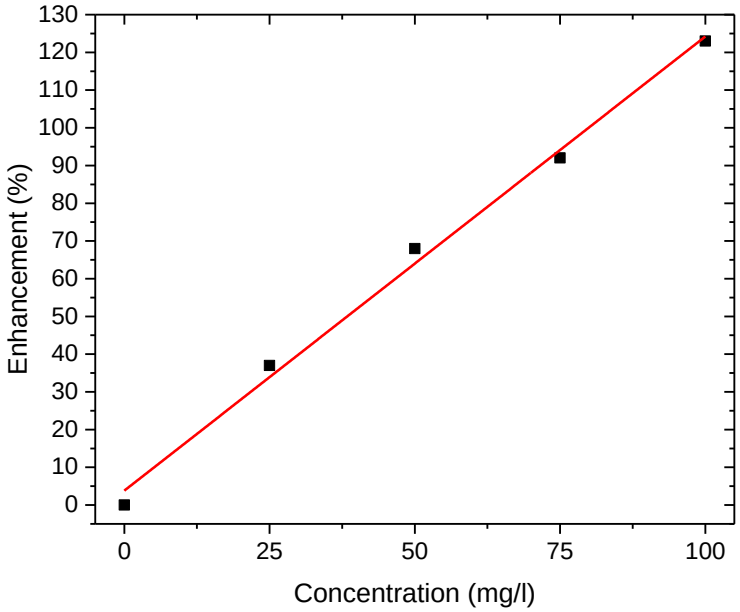

Figure 3.24 Photo-thermal conversion efficiency enhancement of CB nanofluids.

From the previous results, it is clear that for the same nanoparticles concentration, the temperature rise of Au nanofluids is higher than that of Cu nanofluids. Therefore, to quantify the ability of a certain nanoparticle to generate heat, the specific absorption rate (SAR) in $[^{kW}/_{g}]$ was used, which indicates the amount of heat generated per unit time by a unit mass of nanoparticles [77], [79]:

$$SAR = \frac{\left[\left(c_w m_w + c_{np} m_{np}\right)\Delta T_{nf} - c_w m_w \Delta T_w\right]/\Delta t}{m_{np}} \qquad 3.15$$

However, the cost of the nanofluids is crucial for solar applications, especially applications that need large amounts of working fluids. So, to investigate this

factor, the estimated cost (EC) in [$^{\$}/_{kW}$] of generating a unit heat per a unit time was employed:

$$EC = \frac{cost_{np}}{SAR} \qquad 3.16$$

where $cost_{np}$ is the cost of the nanoparticles in [$^{\$}/_{g}$]used in synthesizing the nanofluids. The price of Au and Cu was taken from the international markets for metal stocks, which represents the lowest cost to generate one kW of heat, while the price of CB was taken from the supplier (Alfa Aesar). Figure 3.25 shows the SAR and EC of both Au, Cu and CB nanofluids. It is obvious that Au nanofluids have higher SAR than Cu nanofluids (ten folds), but the cost of generating 1kW heat is much higher than that of Cu nanofluids (i.e., the cost of using the lowest Au nanoparticles concentration, 30 mg/l, is higher than $100, while the cost of using the highest Cu nanoparticles, 3000 mg/l, is less than $ 0.3). However, the SAR for the CB nanofluids is higher than that of Au nanofluids and, at the same time, $EC$is comparable with that of Cu nanofluids.

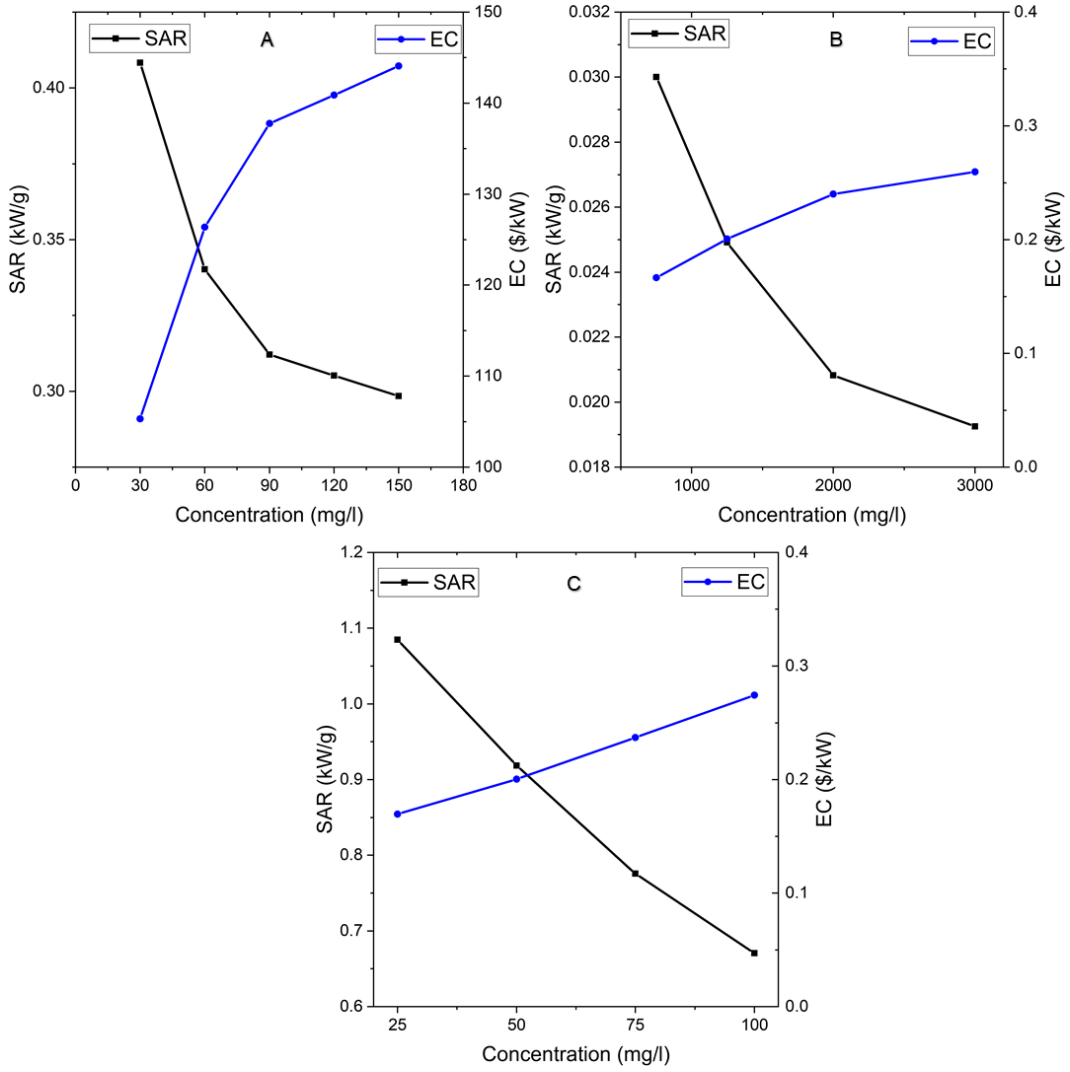

Figure 3.25 Specific absorption rate and cost of a unit heat per unit time for: (A) Au, (B) Cu, (C) CB nanofluids.

The prediction of the maximum PTE can be done by relying on the results of the absorbance spectrum tests as follow:

$$PTE_{max} = \frac{\int_0^\infty I_{\lambda,abs} d\lambda}{\int_0^\infty I_{\lambda,o} d\lambda} = \frac{\int_0^\infty I_{\lambda,i}(1 - e^{-A_\lambda y}) d\lambda}{\int_0^\infty I_{\lambda,o} d\lambda} \quad 3.17$$

where A_λ is the spectrulal absorbance.

The solar spectral irradiance of air mass (AM) 1.5 was adopted as shown in [78].

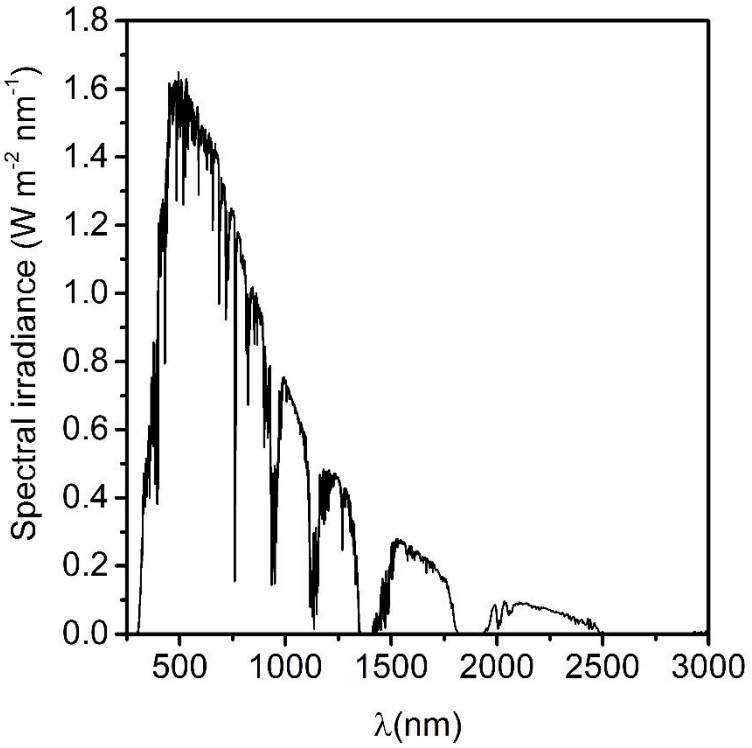

Figure 3.26 Spectral irradiance of the solar energy at the sea level (AM 1.5).

Due to the limitation of the spectrometer used in this study (320 nm ≤ λ ≤ 1060 nm), and because water is almost transparent over this range (see Figure 3.15), the calculated PTE_{max} was assumed to represent the effect of nanoparticles only. Therefore, the PTE enhancement can be re-written as:

$$enhancement_{max} = \frac{(PTE_{max} + PTE_w) - PTE_w}{PTE_w}.100\% \qquad 3.18$$

A comparison between the maximum enhancement predicted from Eqn. 3.18 and the photo-thermal conversion enhancement is shown in Figure 3.27. The

results show a linear behaviour as expected. It is clear that CB nanofluids have the highest enhancement comparing to Au and Cu nanofluids, due to their broad and high absorbance spectrum.

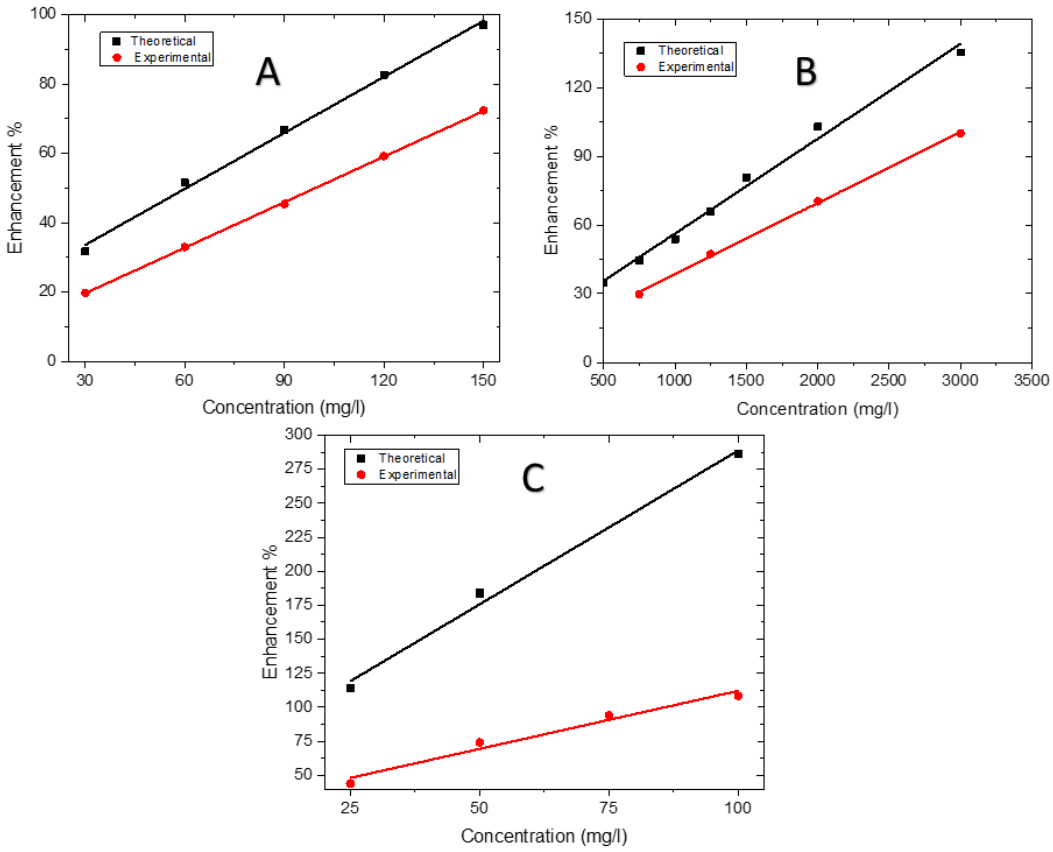

Figure 3.27 A comparison between the maximum enhancement (Theoretical) and PTE enhancement (experimental) for: (A) Au, (B) Cu, and (C) CB nanofluids.

3.4 Chapter Summary

In order to enhance the solar photo-thermal conversion performance based on the direct absorption concept, Au, Cu, Au-Cu hybrid, and CB nanofluids with different concentrations were prepared and characterised in this work. Extensive experiments were conducted with various nanofluids under a high-quality solar simulator, and important conclusions can be drawn as follows:

- Seeding water with nanoparticles enhances the solar photo-thermal conversion efficiency, and this enhancement is linearly proportional to the nanoparticle concentration, which obeys the Beer's law.
- The solar energy absorption efficiency does not increase by blending different nanofluids with different absorbance peaks. Although the blending broadens the peak's width, it reduces the absorption peak value due to the dilution in particle concentration.
- Considering both photo-thermal conversion efficiency and potential economic cost, CB nanofluid is a suitable candidate, while Au is not.
- Using the optical properties of a nanofluid could predict its maximum solar photo-thermal conversion efficiency.

Chapter 4

NANOPARTICLE-ASSISTED SOLAR EVAPORATION

4.1 Introduction

Vaporisation is a phase change process of a material from the liquid phase to vapour. The atoms or molecules of a material are held together by cohesive forces in the liquid phase. The transition to the gaseous phase (vapour) happens when the atoms or molecules get enough kinetic energy to overcome these cohesive forces. Vaporisation can be subdivided into two main categories:

- Evaporation. In this case, the atoms or molecules at the interfaces between the gaseous and liquid phases get enough kinetic energy to overcome the cohesive forces and escape to the gaseous phase. Evaporation continues when the partial pressure of the vapour is lower than the saturation pressure. In this case, the rate of the escaping atoms or molecules to the gaseous phase is higher than the rate of the rate of re-joining to the liquid phase. Therefore, the net change is a reduction in the mass of the liquid phase and an increase in the mass of the gas phase. While at saturation point, where the partial pressure of the vapour is equal to the saturation pressure, the net change of the liquid and gaseous mass is zero since the both the escaping and re-joining rates are equal.
- Boiling. In this case, a transition process from liquid to gaseous phase occurs at the interface between the liquid and the container's wall. Boiling happens when the vapour pressure becomes higher than the

system pressure. The vapour phase is surrounded by the liquid phase forming bubbles. These bubbles grow up due to continuous heating and float up, due to the reduction in their density, to the interface between gaseous and liquid phases to release their contents to the gaseous phase.

In both evaporation and boiling, utilising the solar technologies can be recognised as sustainable and eco-friendly ones. Utilising the solar energy in steam generation instead of heating the bulk volume of a nanofluid can enhance the steam generation process. This enhancement can be achieved if most of the solar energy is absorbed in a very thin (molecular-sized) layer of a nanofluid at the interface between the gaseous and liquid phases.

As reviewed in sec. 2.4, vaporisation through direct absorption solar collectors (DASCs) has recently drawn significant attention. Many studies suggested plasmonic nanoparticles, such as gold nanoparticles, to enhance the photo-thermal conversion efficiency of DASCs. However, there is still a lack of comparative studies of the feasibility of using gold nanoparticles for solar applications. In this chapter, the performance assessment of two different categorised particles, i.e., gold and carbon black suspended in water, will be performed in terms of evaporation rate, materials cost and energy consumption.

4.2 Nanofluids Preparation and Characterisations

The preparation procedure of gold and carbon black nanofluids and their characterizations can be seen in the previous chapter, sections 3.3.1, 3.3.2 and 3.3.3.

4.3 Solar Evaporation Experimental Setup

The photo-thermal conversion experimental setup is schematically shown in Figure 4.1. A solar simulator (ORIEL® Sol3A™, Xenon Arc Lamp, CLASS AAA SOLAR SIMULATOR) was used as a light source to minimise the uncertainties under direct sunlight. This solar simulator provides a radiation spectrum matches the solar spectra, and the intensity can be varied by using suitable filters (AM1.5). This device is certified to IEC 60904-9 2007 edition, JIS C 8912 and ASTM E 927-05 standards. The performance parameters of the sun simulator are; spectral match between 0.75 – 1.25% of the solar spectrum, spatial non-uniformity < 2% and temporal instability < 0.5%. A FLIR ONE infrared camera (sensitivity of 0.1 ^{o}C) to detect the temperature distribution within the nanofluids, a Fresnel lens (Edmund Optics) with a 250 mm focal distance to focus the source light, and a digital weighing scale (Ohaus Discovery, a resolution of ±0.1 mg) to measure the samples' mass change were used.

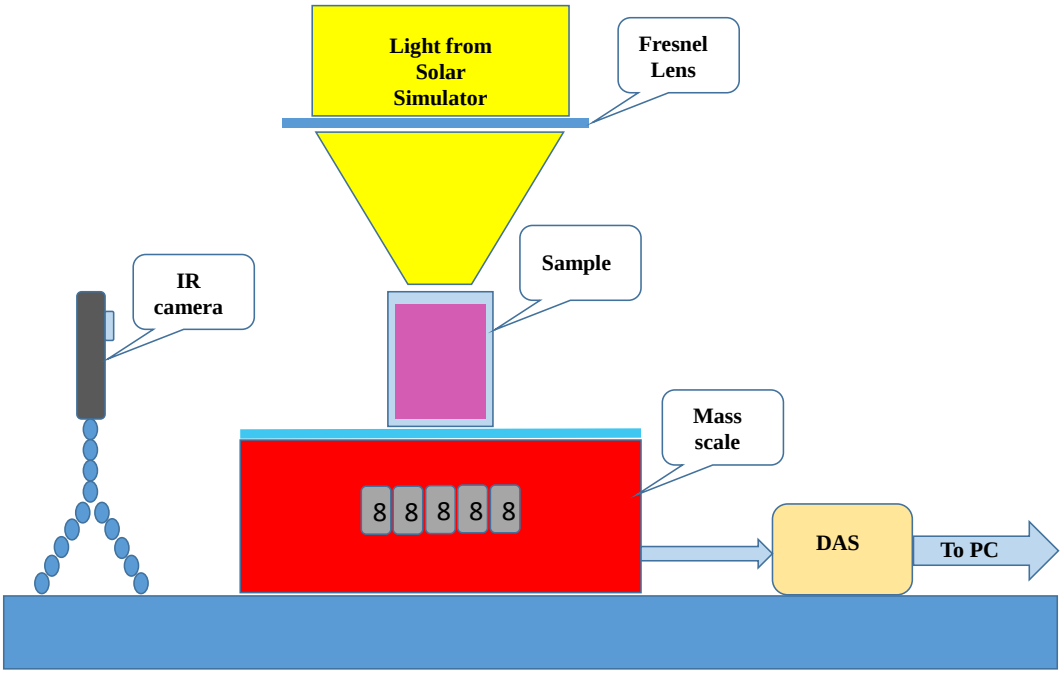

Figure 4.1 Solar evaporation experimental setup.

Three containers were utilised in this study: Two were cylindrical ones of 35 mm diameter and 40 mm in height. One of them was used to get the temperature distribution within the nanofluids using the infrared camera, while the other one was also used to measure the temperature distribution but by using four thermocouples (Omega 5TC-TT-K-36-36, a diameter of 0.13 mm and an uncertainty of ±0.5 ^{o}C). The third container was a Petri dish of 35 mm diameter. 35 ml sample was put in the cylindrical container, and a 4 ml sample was put in the Petri dish to form a thin layer of the nanofluid (~4 mm) to minimise the temperature gradient within the sample, as discussed in sec. 3.2. The data (mass and bulk temperature) were recorded to a PC via a data acquisition system under the LabVIEW environment. The experimental setup, except the solar simulator, was located on a heavy optical table to minimise the vibration effect on the readings, and the experiments were performed in

an isolated (the disturbance and noise were as minimum as possible) and well-controlled lab (the temperature and humidity were within 1^{o}C and 2% respectively). The repeatability was checked. The maximum standard deviations were 3.5mg and 0.33^{o}C for mass and temperature measurements.

4.4 Results and Discussion

4.4.1 Experiments with 35 ml samples

To demonstrate qualitatively the effect of nanoparticles concentration on the solar radiation absorption, temperature distribution within the bulk fluid and evaporation rate, experiment was done by using gold nanofluids (0, 25, 50, and 100 mg/l) subjected to a radiation (heating-up) from the solar simulator (10 kW/m^2) for 900 s and continued for another 900 s without radiation (cooling-down). A FLIR ONE infrared thermal camera (0.1^{o}C sensitivity) was positioned 50 cm far from the sample to capture the temperature distribution within the nanofluid's depth each 60 s and a precise mass scale (Ohaus Discovery, 0.1 mg sensitivity) was used to measure the mass change of the samples, which represents the mass of the generated steam, each one second. The results are shown in Figure 4.2 and Table 4.1.

Figure 4.2 shows the mass change of the samples with time at different nanoparticles concentrations. Obviously, nanoparticles concentration increases, mass change increases, which means steam generation increases. These results suggest that the temperature of the nanofluids at the interface between the liquid and gas phases increases as the nanoparticles

concentration increases. Indeed, the results presented in Table 4.1 justify this suggestion.

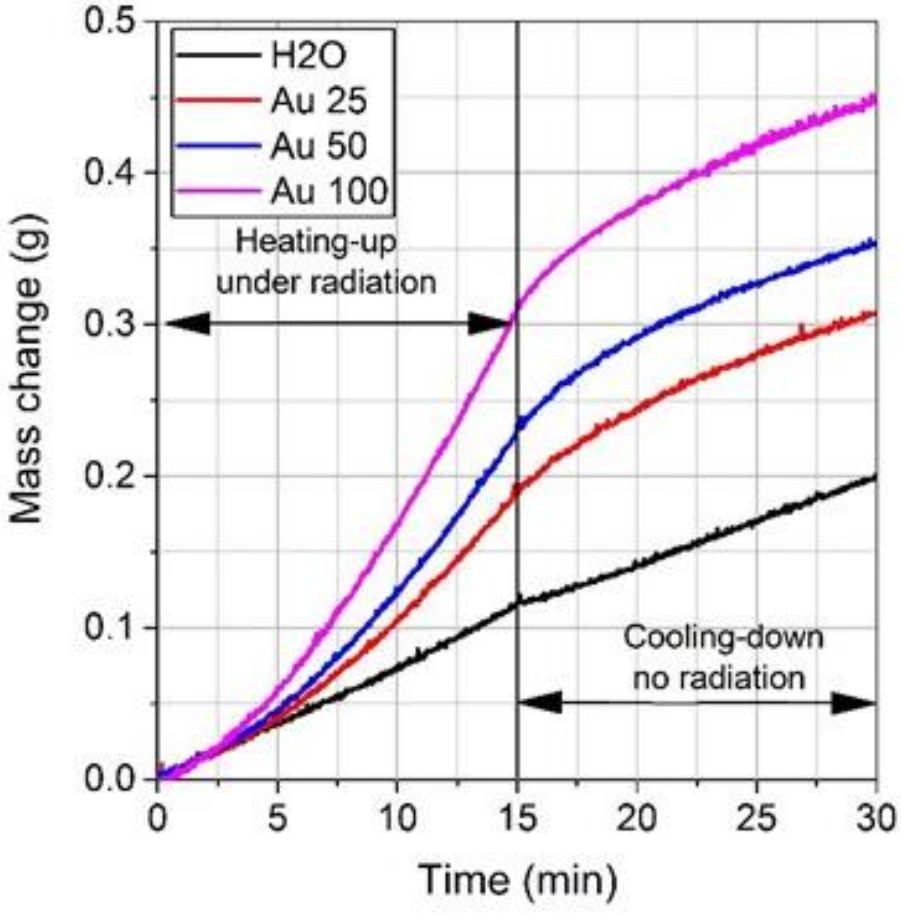

Figure 4.2 Mass change with time of different concentrations of gold nanofluids subjected to 10 kW/m^2.

Table 4.1 Temperature distribution within different concentrations of gold nanofluids. The samples are subjected to 10 kW/m^2 radiation for the first 15 min (heating-up process), after that samples go through a cooling-down process (No radiation).

Time [min]		Au 0 mg/l	Au 25 mg/l	Au 50 mg/l	Au 100 mg/l
Initial stage	0	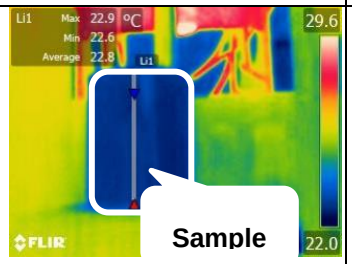	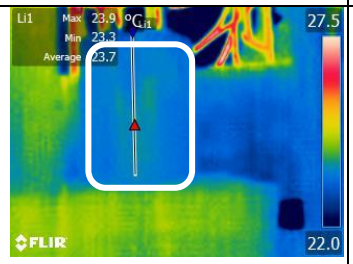	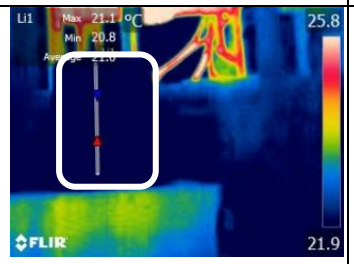	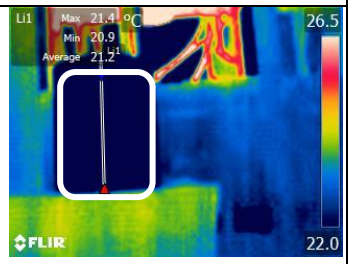
Heating-up under solar radiation	5	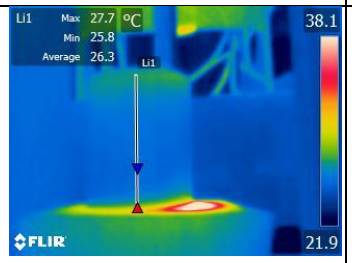	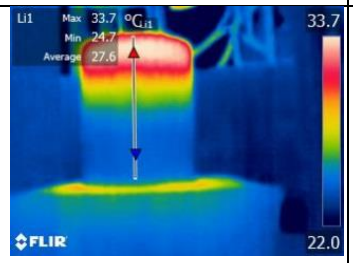	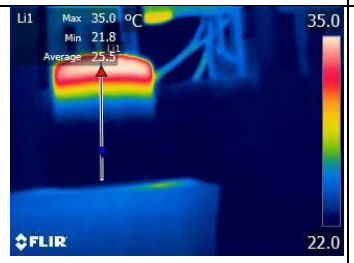	
	10	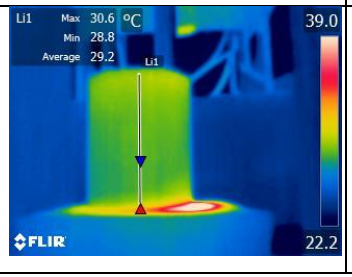	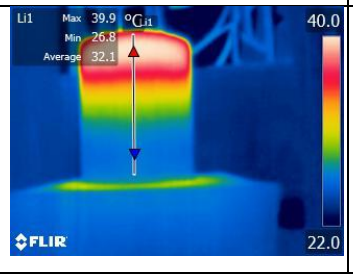	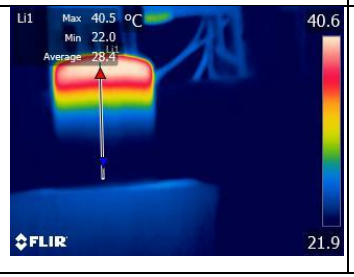	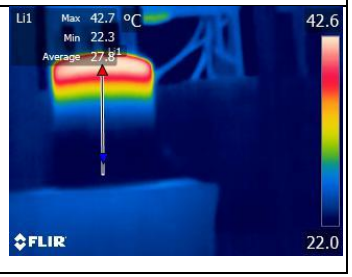

	15	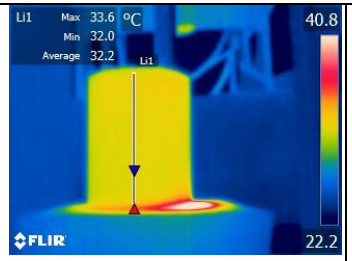	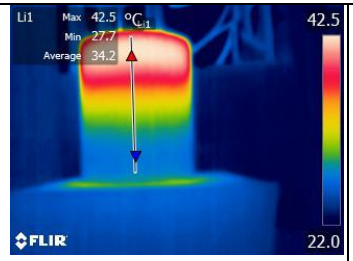		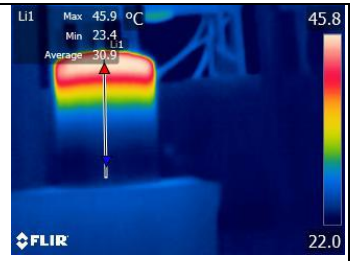
Cooling-down (no radiation)	**20**	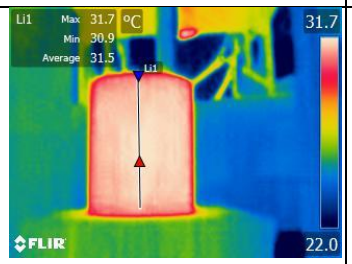	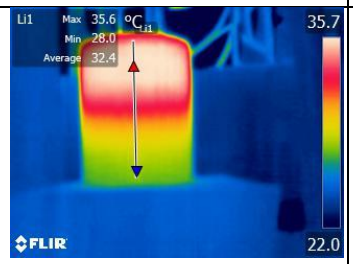	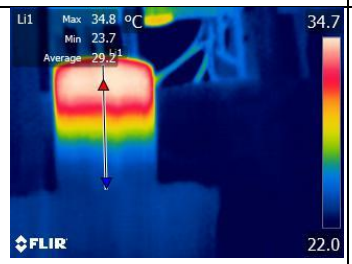	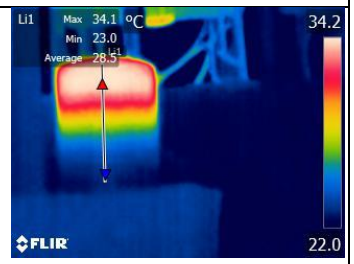
	25	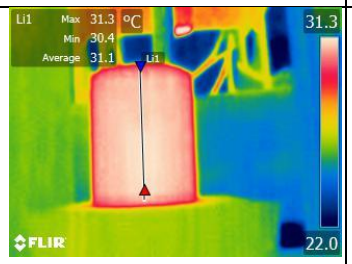	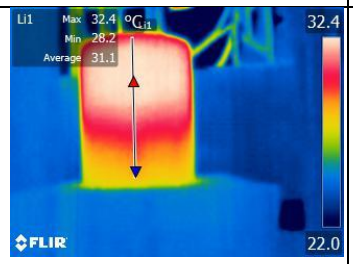	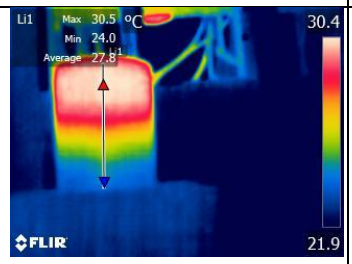	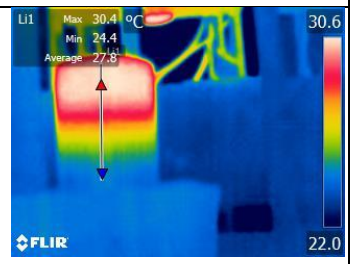
	30	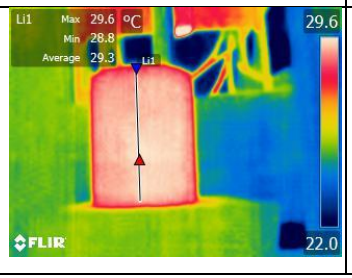	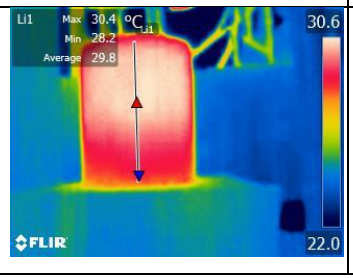	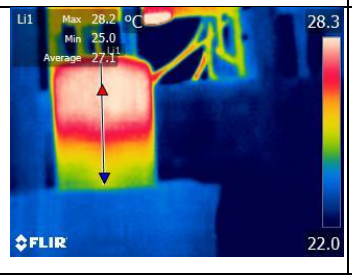	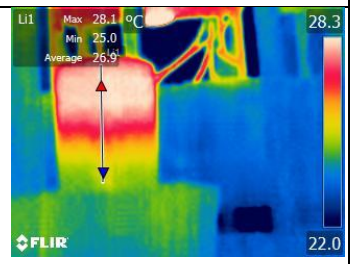

Table 4.1 shows the temperature distribution within the samples' volume for different nanoparticle concentrations at different times. The first column shows the temperature distribution within the samples at the initial stage, i.e., before subjecting the samples to the radiation of the solar simulator. The second, third and fourth columns show the temperature distribution within the samples after 5, 10 and 15 min of samples' illumination with the radiation of the solar simulator respectively. While the fifth, sixth and seventh columns shows the temperature distribution within the samples after 5, 10 and 15 min of cooling down process, i.e. after closing the shutter of the solar simulator. It is clear that adding nanoparticles to water makes the temperature distribution highly non-homogeneous during the heating-up process under the solar simulator light. With the increase of nanoparticles concentration, the hottest layer of the nanofluid becomes thinner and closer to the interface between the gaseous and liquid phases, resulting in a higher evaporation rate. For instance, the maximum temperatures of these hottest layers are 33.7, 35 and 37.1 ^{o}C for 25, 50 and 100 mg/l Au nanofluids after 5 min of illumination. Also, it is clear that a thin layer of nanofluid is needed to minimise the nonhomogeneity in the temperature. Therefore, a small volume of the nanofluids was used to investigate the feasibility of using gold nanofluids in solar evaporation applications, as in section 4.4.2. However, the temperature distribution gradually becomes homogenous during the cooling-down process, i.e. under no radiation.

These results can be interpreted relying on Beer's law, which relates the transmitted radiation to the material properties through which the radiation is passing, as described in the previous chapter, sec. 3.2.

Assuming constant spectral extinction coefficient, the graph of Eq. 3.9 is shown in Figure 4.3. As the evaporation process is a surface phenomenon, it is preferred to trap most of the solar energy in a very thin layer of the nanofluid to maximise the efficiency of the solar evaporation process. However, it is obvious that to achieve this goal, a high extinction coefficient is needed. For instance, the extinction coefficient of 24 is required to absorb 90% of the incident energy in 1mm thick nanofluid's layer, as can see in Figure 4.3 (B). Going back to Figure 3.15(C) and assuming that Beer's law is still applicable (Beer's law is applicable for dilute solutions), performing linear extrapolation reveals that the corresponding concentration is 830 mg/l. It is expected that the concentration of gold nanofluid must be higher than 830 mg/l due to its low absorbance comparing to carbon black, as can be seen in Figure 3.15(A). Such a high concentration might prevent utilising gold nanofluids in solar applications that need to a big volume of working fluids.

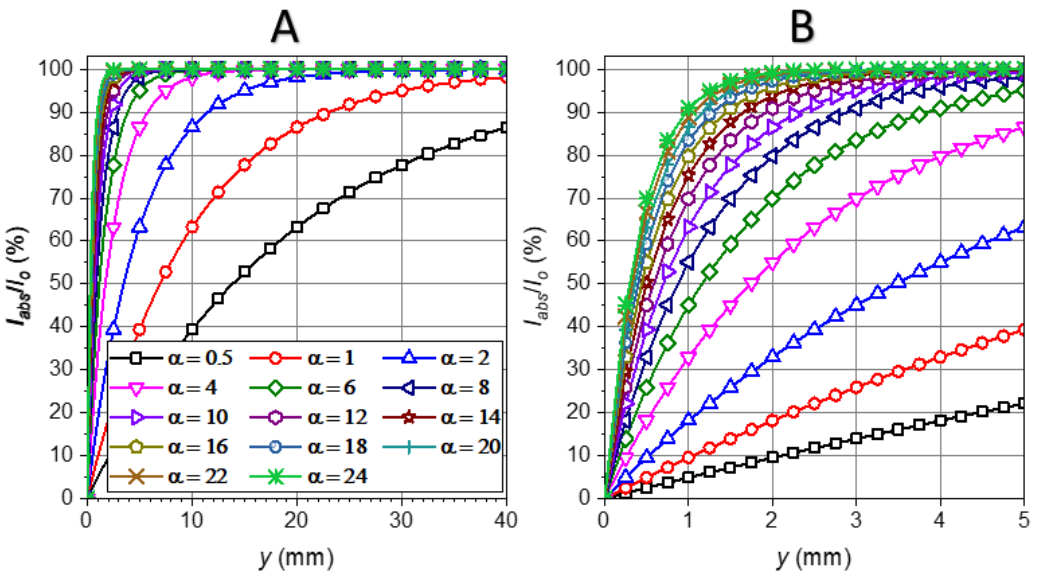

Figure 4.3 Percentage of the absorbed energy as a function of the light path at different extinction coefficients. Light path is 40 mm (A) and 5 mm (B).

Figure 4.4 shows the rate change of the absorbed light intensity with respect to the nanofluid's depth as a function of the incident light intensity, which represents the graph of Eq.3.10, assuming unity extinction coefficient. It is clear that the incident light intensity has a significant effect on the $\frac{dI_{abs}(\lambda)}{dy}$ value. As the initial incident light increases, the slope of $\frac{dI_{abs}(\lambda)}{dy}$ increases when $y \to 0$. In other words, more energy is absorbed near the interface between the liquid and gaseous phases when the incident light is increased. As a result, it is expected that the highest temperature is near the interface. To justify this expectation, a photo-thermal conversion experiment was performed using carbon black nanofluid (CB 25 mg/l) under different light intensity, i.e. 1, 2.5, 5 and 10 Suns. The temperature distribution within the nanofluid was recorded via 4 K-type thermocouples (Omega 5TC-TT-K-36-

36, a diameter of 0.13 mm and an uncertainty of ±0.5 °C) positioned at the centre of the sample at different depths from the air-nanofluid interface, as can be seen in Table 4.2. Indeed the temperature decreases nonlinearly as the position goes deeper in the nanofluid during the heating-up under the incident radiation and the best fitting expression for this temperature decay is $T(y) = a\, e^{-\frac{y}{b}} + T_o$ where a and b are constants and y is the position from the interface. This nonlinear decay becomes more obvious when the intensity increases. The trend of the temperature distribution lines suggests that the temperature near the interface is highest. While during the cooling-down process (no radiation), it is clear that the temperature becomes lower near the interface than the other positions in the nanofluid, which is due to the heat loss by evaporation and convection.

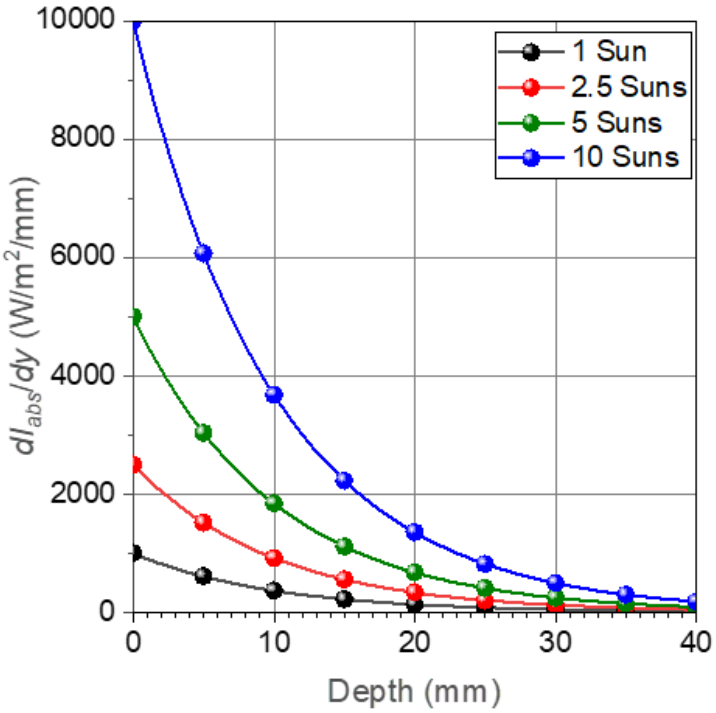

Figure 4.4 The rate change of the absorbed energy with respect to nanofluid's depth at different incident light intensities.

Table 4.2 The effect of the incident light intensity on the temperature distribution during heating-up (symbols for the experimental data and the lines are trend lines) and cooling-down of a nanofluid at different time steps.

	Heating-up	Cooling-down
1 Sun	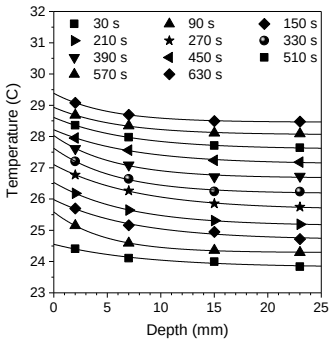	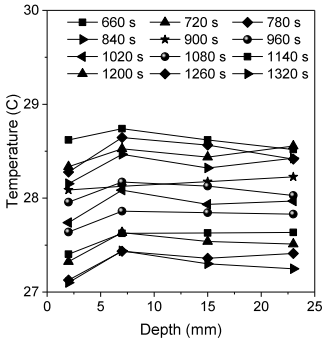
2.5 Suns	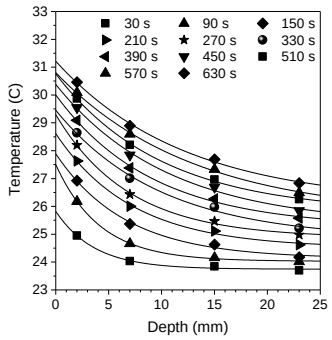	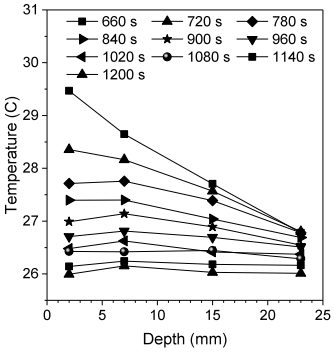
5 Suns	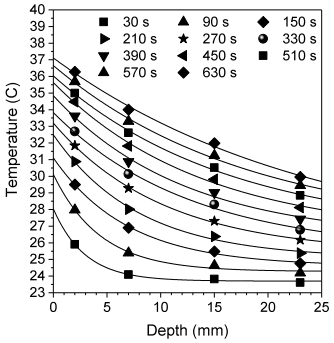	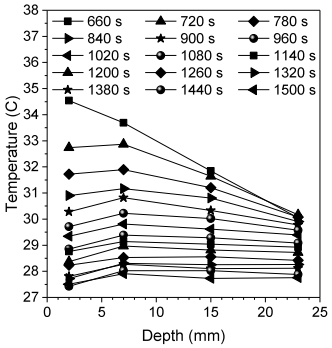
10 Suns	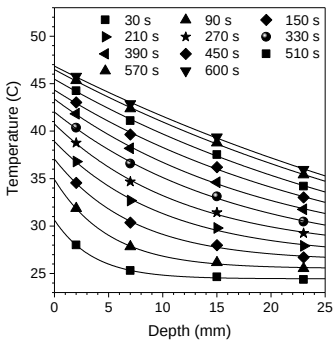	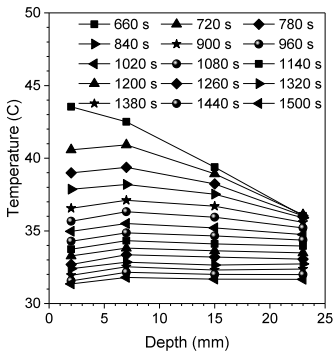

4.4.2 Experiments with 4 ml samples

In this section, a comparative examination between gold (high-cost) and carbon black (low-cost) nanofluids has been conducted quantitatively. A 4 ml of gold or carbon black nanofluid sample was put in the 35 mm Petri dish making ~4 mm thin layer under a solar radiation of 10 kW/m^2 for 600 s. During this period, the samples' temperature and mass were recorded, as shown in Figure 4.5. It is qualitatively evident that the temperature and mass change trends are the same for both carbon black and gold nanofluids. However, the values differ quantitatively, and this depends on the light absorption characteristics. Both the temperature and the evaporated mass of the carbon black nanofluids are higher than that of gold nanofluid, which is consistent with the absorbance characteristics shown in Figure 3.15.

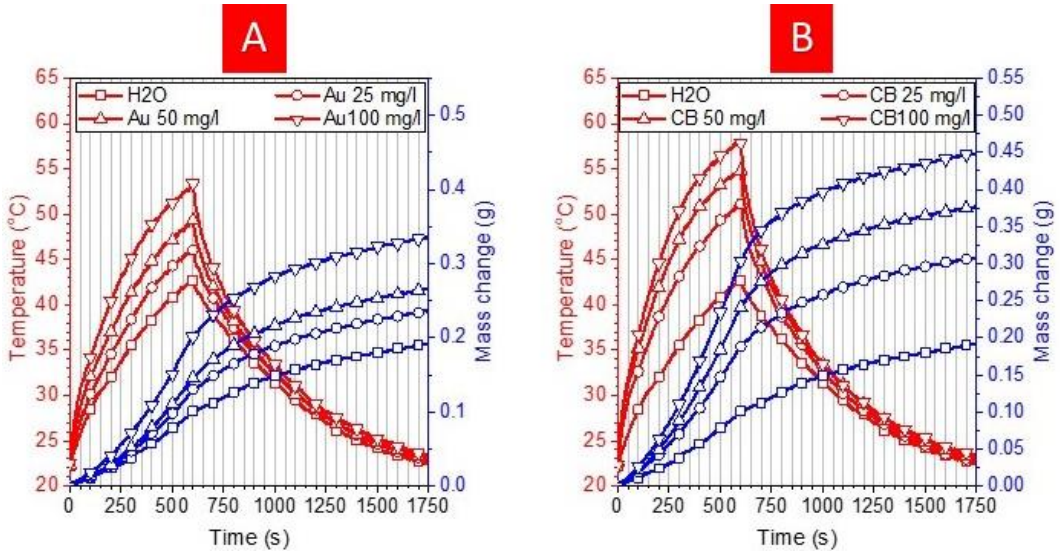

Figure 4.5 Temperature and mass change with time for (A) gold and (B) carbon black nanofluids subjected to 10 kW/m^2 irradiance.

Figure 4.6 shows the evaporation rate, the numerical differentiation of the mass change with time, as a function of time and temperature at different nanoparticle concentrations for gold and carbon black nanofluids respectively. It is noted that for both samples, the evaporation rate is higher during the heating-up period than the cooling-down period at the same temperature reading, and this difference becomes more significant as the nanoparticles concentration becomes higher. As the evaporation rate is proportional to the kinetic energy of the water molecules at the interface between the gaseous and liquid phases, this difference shall be related to the interface temperature difference between the heating-up and cooling-down periods as the rate change of the absorbed energy with respect to the sample depth is an exponential function as shown in Figure 4.4 and Table 4.2. and this difference increases as the nanofluid's extinction coefficient increases. It shall be noted that the thermocouple is located 2 mm beneath the interface between air and the nanofluid sample. Therefore, even the measured fluid temperature is the same, the interface temperature during the heating-up shall be higher than that during the cooling-down processes and consequently, a higher evaporation rate is expected during the heating-up period.

In addition, one can see that the evaporation rate of different nanofluid concentrations is the same during the cooling-down period at temperatures below 35^{o}C. This is consistent with the temperature measurement in Figure 4.5, where the temperatures of all concentrations become the same after time ~1100 s. As a result, it can be concluded that the effect of the nanoparticles is just to enhance the radiation absorption properties. To enhance the

evaporation rate, a better approach is to trap most of the solar energy near the surface, which requires very high nanoparticle concentrations. That will raise problems such as nanoparticles' instability, viscosity increase, and cost increase.

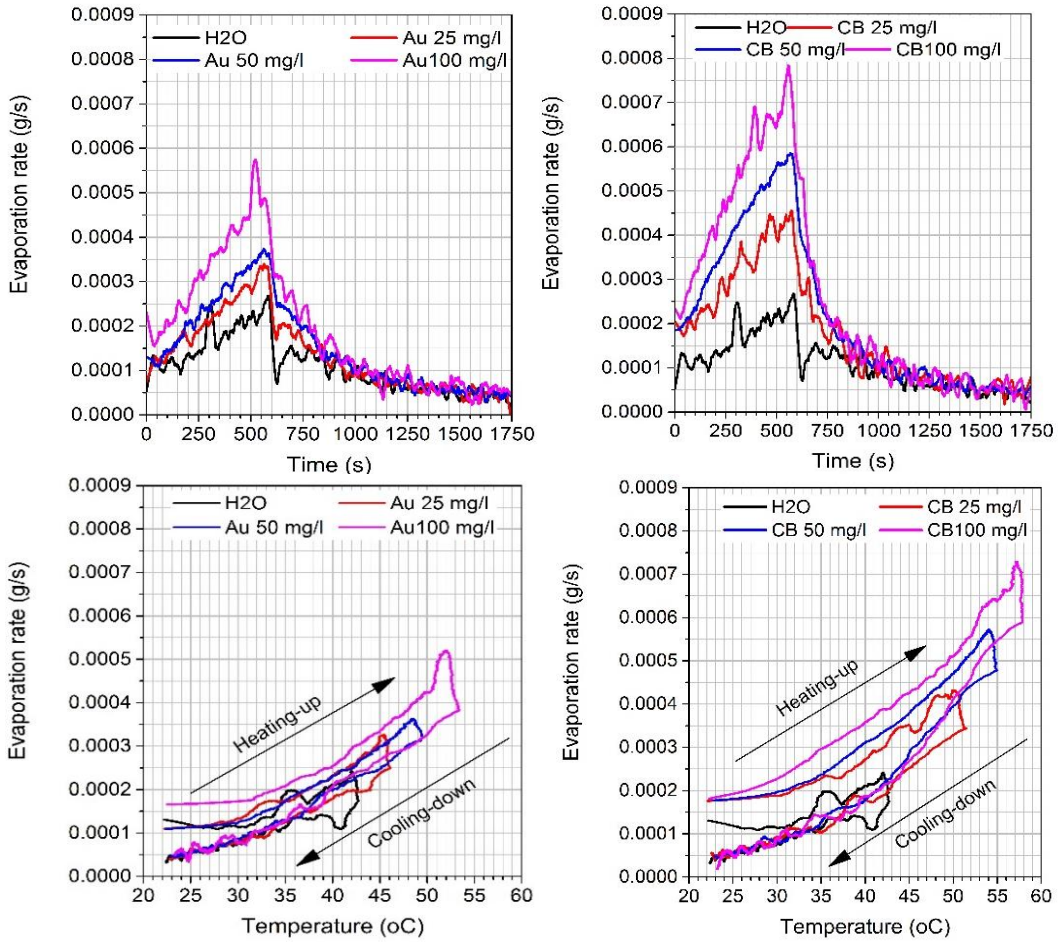

Figure 4.6 Evaporation rates for gold and carbon black nanofluids as a function of time (upper row) and temperature (lower row). Heating-up process is under 10 kW/m^2 irradiance.

To investigate the feasibility of using gold nanofluids in solar evaporation applications, the estimated cost of producing 1 g/s of water vapour was calculated as:

$$EC = \frac{Cost_{np}}{\left(\frac{\dot{m}}{V * C}\right)} 10^6 \qquad 4.1$$

where EC is the estimated cost $\left[\frac{\$}{g/s}\right]$, $Cost_{np}$ is the cost of 1 gram of the nanoparticles $[\frac{\$}{g}]$. The value of \$43 was used for gold nanoparticles, which represents the price of gold in the global stocks market, and that of \$0.18 was used for carbon black nanoparticles, which represents the supplier price; $\dot{m}$ $[\frac{g}{s}]$ is the evaporation rate; V is sample's volume $[ml]$ and C is the sample's concentration $[\frac{mg}{l}]$. The results are shown in Figure 4.7. The cost of producing 1 g/s vapour by gold nanofluids is much higher than that produced by carbon black nanofluids (~300 folds). Also, one can see that the cost of producing vapour is proportional to the nanoparticles concentration even though the evaporation rate increases as the concentration increases. This is because most of the nanoparticles are in the bulk volume of the samples and not directly participate in vapour production.

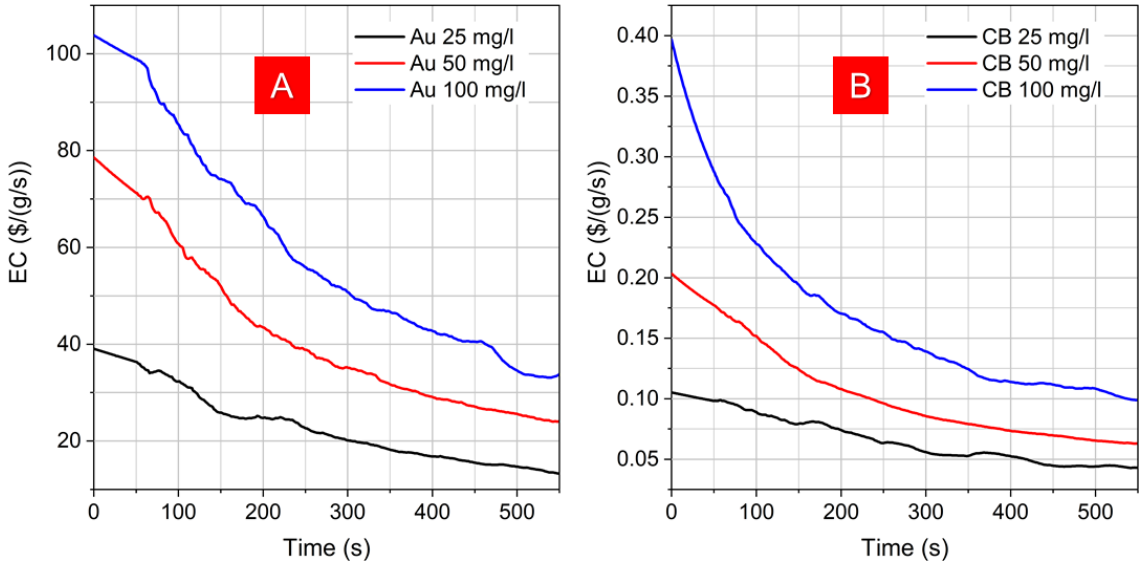

Figure 4.7 The dynamic cost of producing 1 g/s vapour using (A) gold and (B) carbon black nanofluids subjected to 10 kW/m^2.

The following equations were used to investigate how much of the absorbed solar energy was consumed by evaporation (latent heat) and how much was for heating-up the bulk nanofluid (sensible heat):

$$E_{evap.} = \sum_{i=1}^{n} (m_{i-1} - m_i) \ * \ h_{fg,i} \qquad 4.2$$

$$E_{heating-up} = \sum_{i=1}^{n} C_{p,i} \ * m_i \ * (T_i - T_{i-1}) \qquad 4.3$$

where i is the time step and each step equals 1 s; $n = 600\ s$, which represent the heating-up period; $E_{evap.}$ is latent heat; m_i is the instantaneous sample's mass in$[g]$; $(m_{i-1} - m_i)$is the instantaneous vapour mass generated in one second in $[g]$; $h_{fg,i}$ is enthalpy change from liquid to vapour at time step i in $[\frac{J}{g}]$; $E_{heating-up}$ is sensible heat; $C_{p,i}$ is the specific heat capacity of the

nanofluid at time step i in $\left[\frac{J}{gK}\right]$; T_i is the instantaneous sample's temperature in $[K]$.

The thermophysical properties of the nanofluids can be assumed as the same of water because the maximum volumetric concentration is 0.000518% and 0.005% for gold and carbon black nanofluids respectively [77], [85], [120], [121]. The specific heat capacity of water was assumed constant and equal to 4.183 J/gK. This assumption is due to the specific heat capacity of water changes negligibly, i.e. between 4.182 J/gK at 20 °C and 4.185 J/gK at 60 °C [122]. While a linear fit with r^2 of 0.9998 was used for $h_{fg,i}$ as a function of temperature. The results are shown in Figure 4.8 and Figure 4.9. It is clear that the energy used for evaporation by carbon black nanofluids is ~1.64 times higher than that consumed by gold nanofluids. The latent to sensible heat ratio is also higher for carbon black nanofluids and such a ratio increases as the concentration increases.

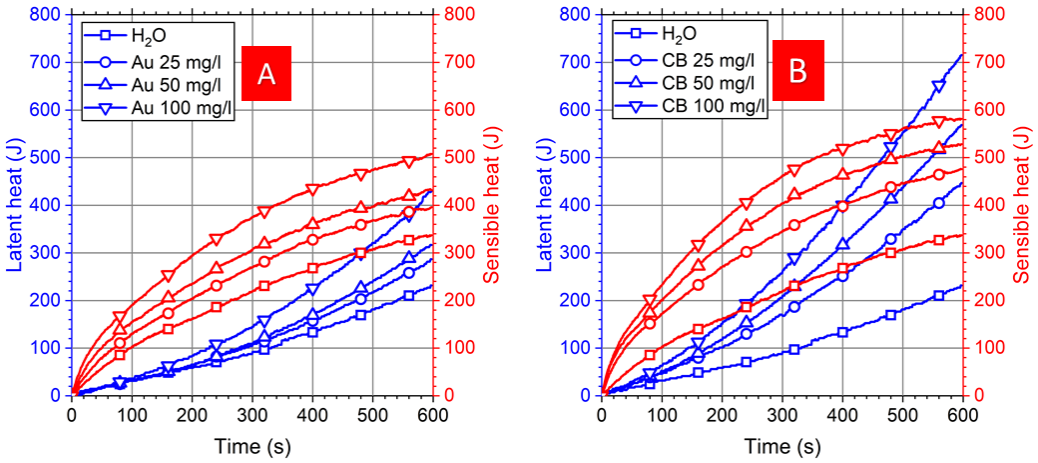

Figure 4.8 Total latent and sensible heat for (A) gold and (B) carbon black nanofluids subjected to 10 kW/m² irradiance.

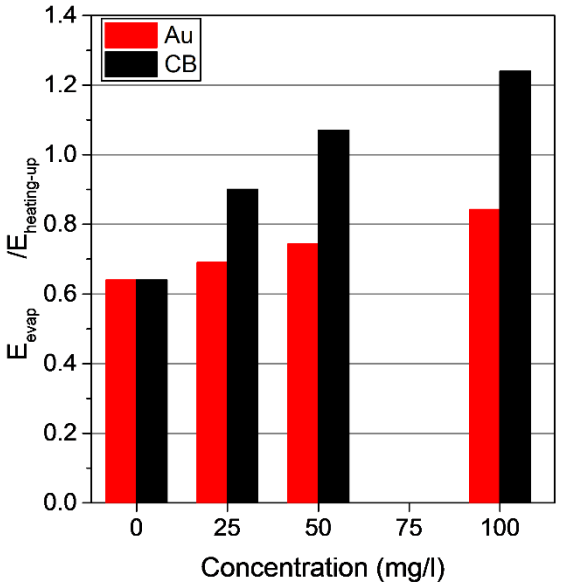

Figure 4.9 The ratio of latent to sensible heat of Au and CB nanofluids. Time= 600 s and I=10 kW/m^2.

Figure 4.10 shows the temporary evaporation efficiency, i.e. energy consumed for evaporation (latent heat) to the total incident energy, as a function of nanofluid's concentration. It is obvious that the evaporation efficiencies of carbon black nanofluids are higher than that of gold nanofluids, which is due to the better solar absorption of carbon black than gold nanofluids. The evaporation efficiency increases as the time increases because of the temporal temperature increase, as shown in Figure 4.5. However, the photo-thermal conversion efficiency (PTE)-the ratio of the evaporation energy (latent heat) to the energy stored in the nanofluid (sensible heat) to the total incident energy-decreases as time increases, as shown in Figure 4.11. This reduction in PTE is due to the heat losses by convection and radiation. At the first stage, i.e. time ~0s, the increase in the nanofluid's

temperature is negligible. Therefore, the heat loss is almost zero. As the time increases, the nanofluid's temperature increases, and consequently the heat loss by convection and radiation increases. As a result, the rate of storing energy in the nanofluid (sensible heat) decreases as time increases, as shown in Figure 4.8 and finally, the PTE decreases. Both evaporation process and heat loss by convection and radiation depend on the surface area and temperature. Increasing the nanofluid's surface area and temperature enhances the evaporation rate, but also increases the heat losses.

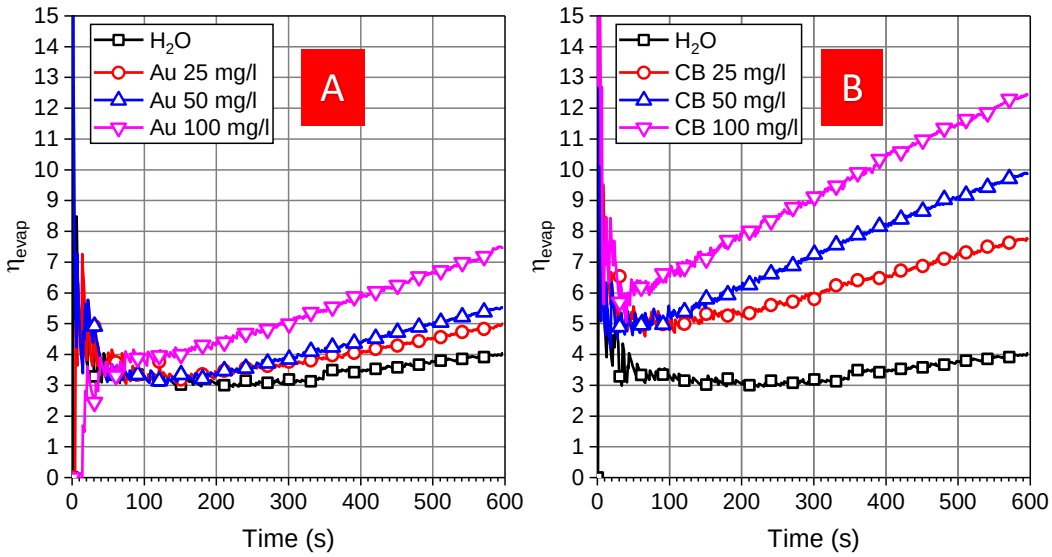

Figure 4.10 Evaporation efficiency as a function of time at different nanofluid's concentration for (A) gold and (B) carbon black nanofluids subjected to 10 kW/m^2 irradiance.

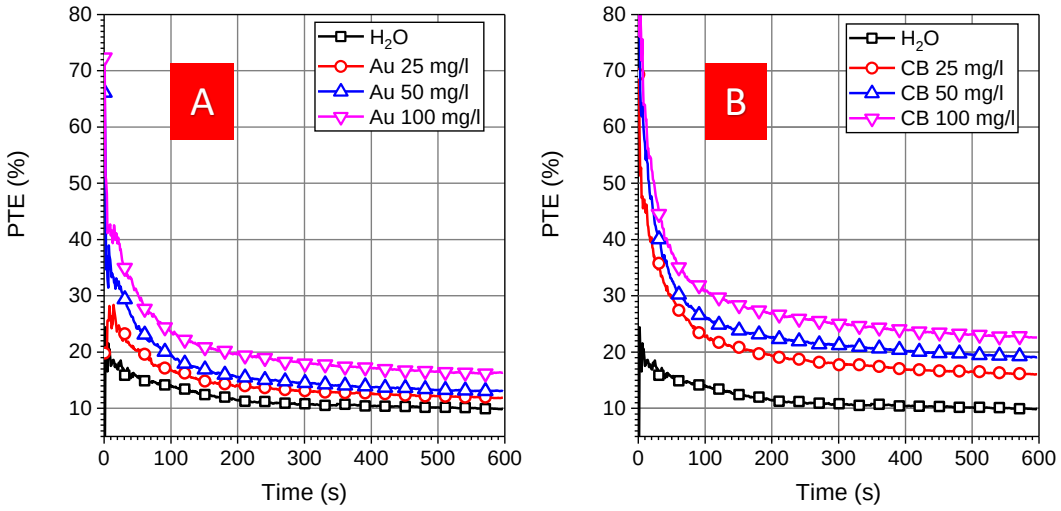

Figure 4.11 Photo-thermal conversion efficiency as a function of time at different nanofluid's concentration for (A) gold and (B) carbon black nanofluids subjected to 10 kW/m^2 irradiance.

4.4.3 Experiments with a porous medium

It is proved in 4.4.1 and 4.4.2 that nanoparticles can convert the photo-energy into thermal-energy. The higher the nanoparticles concentration and/or the incident light intensity is, the higher the photo-thermal conversion is near the liquid/gaseous interface, which leads to higher temperatures there and higher evaporation rates. However, Figure 4.10 and Figure 4.11 show that unavoidable part of the incident radiation goes to heat up the bulk nanofluid sensibly by heat conduction mode. While the better scenario is converting most of the absorbed energy into vapour to enhance the evaporation efficiency. These findings suggest that using very thin black porous medium might be a better alternative. This porous medium has to absorb the solar energy efficiently converting it into thermal energy. Also, the porous medium must transfer the converted energy to the water molecules at the

gaseous/liquid interface effectively but suppress the heat transfer into the water bulk volume. Water must be fed continuously to the porous medium in order to compensate for the evaporated water.

In order to investigate the solar water evaporation via a porous medium, A micro-sized thin black carbon-based gas diffusion layer (GDL), which is commonly used in fuel cells industry, was purchased from Fuel Cells Etc[1]. Some of the GDL's properties can be seen in Table 4.1.

Table 4.3 Properties of the GDL type ELAT.

Property	**Units**	**Value**	Hydrophilic ELAT
Thickness	micron	406	
Areal Density	g/cm²	0.013	
Volumetric Density	g/cm³	0.346	
Porosity	%	80	
Carbon Content	%	99.5	

The spectral absorbance of the GDL is presented in Figure 4.12, which reveals high absorption capability.

[1] http://fuelcellsetc.com/

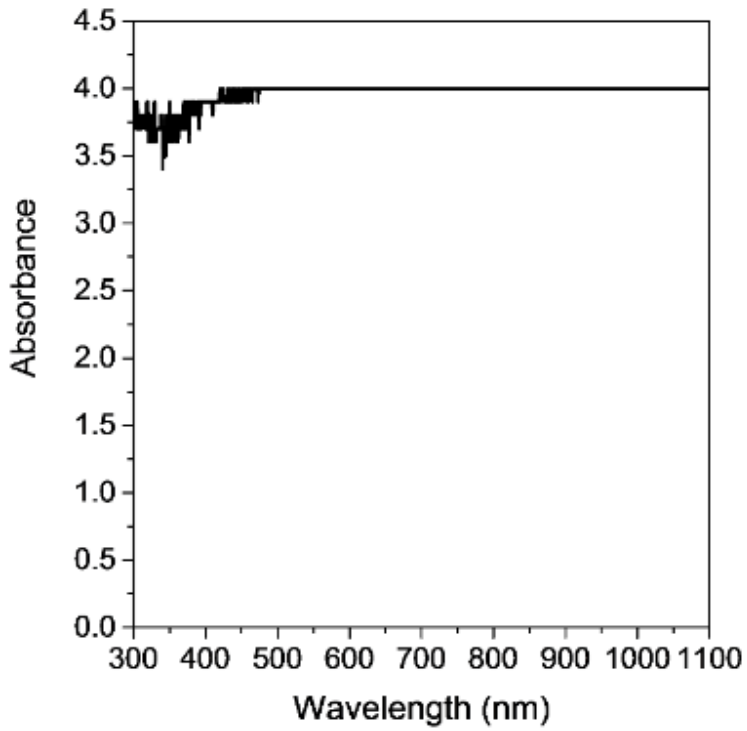

Figure 4.12 Spectral absorbance of the GDL.

As the porosity of the GDL is 80%, it is expected that heat can transfer from the hot GDL to the bulk water through the watery volumetric contact. To avoid this heat loss, a piece of polystyrene insulation board (PIB) was used to block the way against the heat to transfer to the bulk volume of water, and a hydrophilic tissue was used to feed the GDL with water, as shown in Figure 4.13.

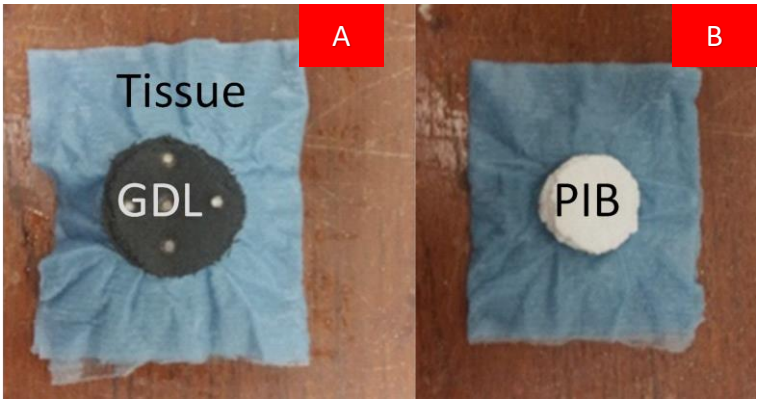

Figure 4.13 The GDL, hydrophilic tissue and PIB system. (A) a top view and (B) a bottom view.

A comparison of steam generation via different concentrations of gold nanofluids, GDL and GDL+PIB under the same operating conditions is shown in Figure 4.14. Even though seeding gold nanoparticles in water enhanced steam generation, using a black porous medium (GDL) produced steam higher than the 100 mg/l gold nanofluid. This outweighing is understandable since the GDL's absorbance was higher than gold nanofluids' absorbance, as can be seen in Figure 3.15 (A) and Figure 4.12. Furthermore, significant enhancement in the steam generation was achieved by using PIB as thermal insulation to prevent heat transfer by conduction, reducing the heat losses as sensible heating and improving the solar evaporation.

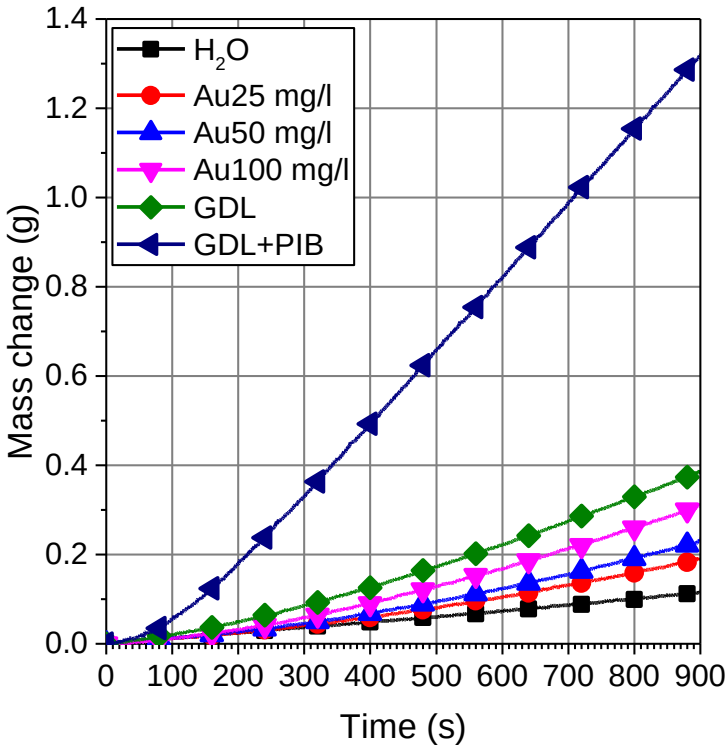

Figure 4.14 A comparison of steam generation via gold nanofluids, GDL and GDL+PIB.

The evaporation rate and efficiency of the GDL+PIB were investigated under three light intensities, namely; 0.82, 5 and 10 kW/m^2. The results are shown in Figure 4.15 and Figure 4.16. Incident light intensity increases, evaporation rate increases. ~1, ~3.25 and ~6.25 kg/hr m^2 evaporation rates were achieved under 0.82, 5 and 10 kW/m^2 intensities respectively. These rates show a linear relationship between the evaporation rate and incident light intensity. However, a nonlinear relationship was found between the evaporation efficiency and the light intensity. The light intensity increases, the efficiency decreases. These are logical results because the GDL's temperature increases when the incident light intensity increases, which results in a higher evaporation rate and heat losses.

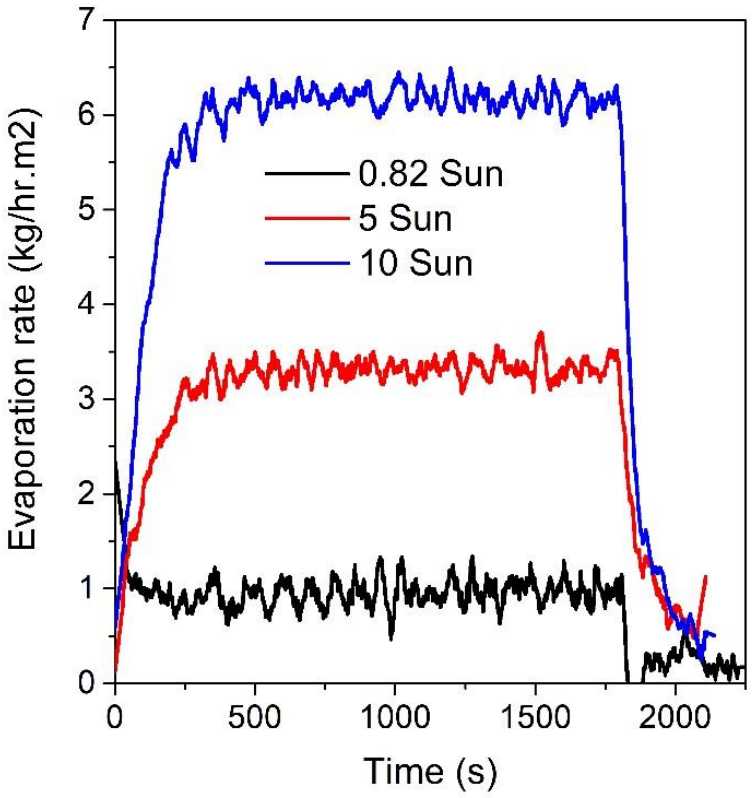

Figure 4.15 Solar evaporation via GDL+PIB under different light intensities.

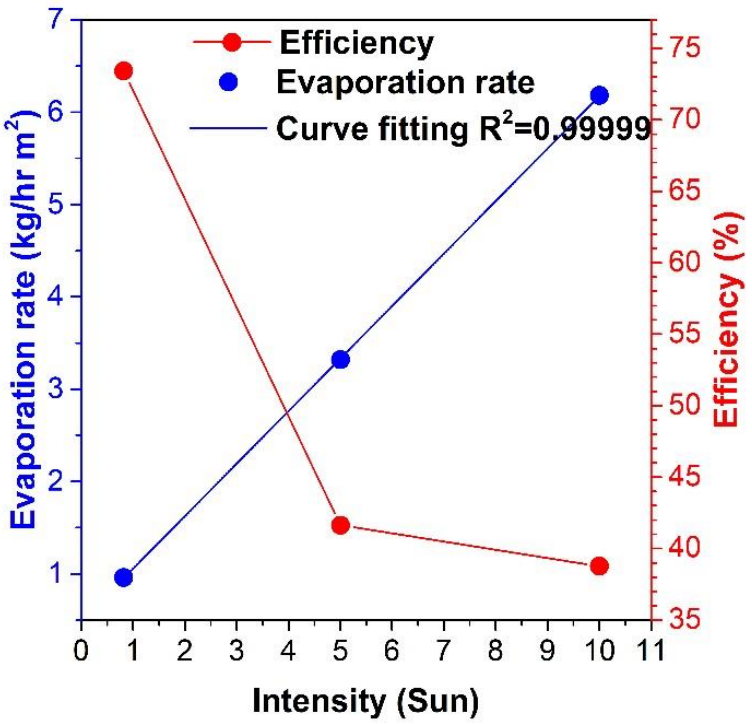

Figure 4.16 Solar evaporation rate and efficiency of GDL+PIB under different incident solar intensities.

4.5 Chapter Summary

In this chapter, the evaporation mechanism was investigated for aqueous gold nanofluid, carbon black nanofluid and carbon-based porous medium subjected to concentrated solar radiation. Experiments were conducted using a AAA-rated top class solar simulator to minimise the uncertainties accompanied with the natural solar radiation. It was found that:

- The higher the concentration of the nanoparticles and/or the higher the incident light intensity is, the more of the solar energy is absorbed in a slim volume near the air-nanofluid interface, leading to a higher interface temperature, and consequently higher evaporation rate. This trend is consistent with the Beer's law, which indicates that the absorbed radiation energy is an exponential function of the extinction coefficient, which is a function of the nanoparticles concentration, and light path length.
- The higher the concentration of the nanoparticles is, the higher ratio of the energy consumed for evaporation (latent heat) to the energy stored in a nanofluid (sensible heat) is.
- To enhance the solar evaporation rate, higher nanoparticle concentrations are required to absorb most of the solar energy in a very thin layer. This will raise many problems such as the instability of the nanoparticles, the change of the physio-thermal properties of the nanofluids, and the high cost as most of the nanoparticles are in the bulk volume and do not participate in the evaporation enhancement directly. While using a black thin porous medium to absorb the solar energy in a thin volume of the water sample and using a thermal

insulation to suppress the heat transfer from the porous medium to the bulk volume of the water sample produces steam at high rates and might considered as a better alternative.

- Moreover, this work revealed that gold nanofluids are not feasible for solar evaporation applications due to the high cost and low radiation absorbance especially for the wavelengths higher than 600 nm. While carbon black nanofluids are cheaper and more efficient than gold nanofluids.

In this chapter and the previous one, the hype of using gold nanofluids and their hybrids was proved not feasible for the solar photo-thermal conversion and steam generation due to the high cost and low performance comparing with carbon black nanofluids. The problem with these studies suggesting the gold nanofluids and their hybrids is the lack of a direct comparison with other cheap nanofluids such as carbon black at the same operating conditions. Thus, investigation the effects of seeding carbon-based nanoparticles (carbon black and carbon nanotubes) in transparent aqueous lithium bromide solutions will be presented in next chapter.

Chapter 5

H_2O-LiBr NANOSOLUTIONS

5.1 Introduction

Solar-driven absorption refrigeration technology has the potential to reduce the peak electricity demand and the global warming. The optimisation of generator and absorber performance is crucial to commercialise this technology. As reviewed in Chapter 2, H_2O-LiBr absorption refrigeration systems are mature technologies, which are driven thermally. Seeding nanoparticles in the H_2O-LiBr binary fluid is a novel idea to:

- Generate the refrigerant (steam) in the generator by directly absorbing the solar energy within the nanosolution.
- Enhance the heat and mass transfer in the absorber, reducing the overall size of the system.

Controversial results can be seen in the few studies have been conducted on H_2O-LiBr seeded with nanoparticles. Although these studies used the same experimental setup, i.e., a falling film on horizontal tubes technique, one study found that the enhancement in the heat transfer is higher than the enhancement in mass transfer. Few other studies found the reverse, i.e., the mass transfer enhancement is much higher than the heat transfer enhancement. The Brownian motion of the nanoparticles and the accompanied micro-convection was concluded as a key factor in the enhancement's mechanism. However, it is difficult to control the thickness and the surface area, which are key factors in heat and mass transfer processes, of the falling film. Therefore, constant surface area and thickness of

nanosolutions were used in this study. The steam absorption by nanosolutions and steam generation from them were investigated experimentally. Furthermore, the effect of seeding nanoparticles in the aqueous lithium bromide solutions on the transmittance, viscosity and thermal conductivity were investigated.

5.2 Nanosolutions Preparation and Characterisations

Carbon-based nanosolutions were prepared in this study because they are efficient in the photo-thermal conversion as demonstrated in Chapter 3 and 4. Also, Kang et al. [46] reported that seeding 0.1 wt.% of CNTs (25 nm in diameter and 5000 nm in length) in 55 wt.% aqueous lithium bromide solution can enhance the steam absorption rate to achieve 210%. Therefore, it is good to investigate the effect of almost the same nanoparticles type to see is there any improvement in the steam absorption if the transfer area is constant.

Carbon black (CB) nanopowder, 99.9+% purity, 42 nm average diameter, and 1.8-2.1 g/cm^3 density @ 25 ^{o}C, was purchased from Alfa Aesar. Multi-walled carbon nanotubes (MWCNTs), 6-8 walls, 70% - 80% carbon content, 10nm outer diameter, 4.5nm inner diameter, 4000nm length, and 2.1 g/cm^3 density @ 25 ^{o}C; Gum-Arab, reagent grade and Tween®80 were purchased from Sigma Aldrich. The lithium bromide, 99$^+$% anhydrous, was purchased from ACROS ORGANICS.

Firstly, different concentrations of H_2O-LiBr binary fluid were prepared by using an analytical scale of 0.1 mg resolution. The concentration was calculated as

$$[C] = \frac{m_{LiBr}}{m_{LiBr} + m_{H2O}} * 100\% \qquad 5.1$$

where m_{LiBr} is the mass of the lithium bromide powder and m_{H2O} is the mass of deionised water. Using magnetic stirrer, concentrations of 10, 20, 30, 40, 50 and 60 wt.% were prepared by dissolving pre-calculated masses of LiBr powder in pre-measured masses of water in containers with lids. Also, samples of different concentrations of Gum-Arab (GA) and Tween®80 (T80) in a binary fluid of 60 wt.% H_2O-LiBr were prepared.

To prepare the nanosolutions, the nanopowder (CB and MWCNTs) was mixed in water using a powerful mixer (Vortex-Genie® 2) for 15 min. After that, the mixture was left on a magnetic stirrer for 24 hr to assure good hydration of the nanopowder. Finally, the mixture was sonicated by using a probe sonicator (Fisher Scientific, 700 W power, and 20 kHz frequency) to form the stock nanofluids. Then, a pre-calculated mass of the LiBr powder was added to the stock nanofluids and stirred for 5 minutes and sonicated for 15 min in a bath sonicator (Fisher Scientific, 750 W power) to get on the stock nanosolutions. Different mass concentrations of the nanosolutions were prepared by diluting the stock nanosolution with H_2O-LiBr 60 wt.% solution. The stability of the nanosolutions was checked via the spectral absorbance using UV-1800 SHIMADZU spectrophotometer. The samples were stable after 24 hrs, and

before every test, the samples were placed in the bath sonicator (Fisher Scientific, 750 W power) for 15 minutes.

A UV-Vis Spectrophotometer (UV-1800, SHIMADZU) was used to measure the absorption capability of different nanosolutions. A KD2 Pro from Decagon Devices, Inc. was used to measure the thermal conductivity. The 6 cm single-needle sensor (error~5% for $0.02 \leq k \leq 2$ W/m.K) was inserted vertically in 3.5 cm diameter sample. The whole setup was placed on an optical table in an isolated room to minimise the vibration effect. Each test was repeated three times for each sample, and the r^2 was greater than 0.999 for all runs. For the dynamic viscosity measurements, an Anton Paar (Physica MCR 301) was used. Four runs were performed for each sample at room temperature (25 ^{o}C).

5.3 Steam Absorption and Generation Experimental Setup

Contrary to the falling film experiments, a constant thickness and surface area samples were used in the steam absorption measurements. This measure is to investigate the effect of the Brownian motion on the steam absorption rate of the nanosolutions by isolating the significant effect of the thickness and surface area of the interface. Figure 5.1 shows the experimental setup for the steam absorption measurements. A 12 cm Petri dish was placed on an analytical scale (0.1 mg resolution), which was connected to a PC through a LabVIEW environment to record the mass change every second. The analytical scale was placed on a heavy optical table in an isolated room to

minimise the effect of vibration. A precise measuring cylinder was used to put 35 ml of each sample in the Petri dish. The mass change of each sample, due to the steam absorption, was recorded for 500 s. The change in the room temperature and relative humidity was controlled within 1^{o}C and 2% respectively.

For the photo-thermal conversion and solar steam generation experiment, the same previous experimental setup was used in addition to a Class AAA solar simulator (ORIEL® Sol3A™) was used as a light source and a K-type thermocouple (Omega 5TC-TT-K-36-36, a precision of ±0.5 ^{o}C) was used as a temperature sensor. A Fresnel lens was used to concentrate the artificial solar energy.

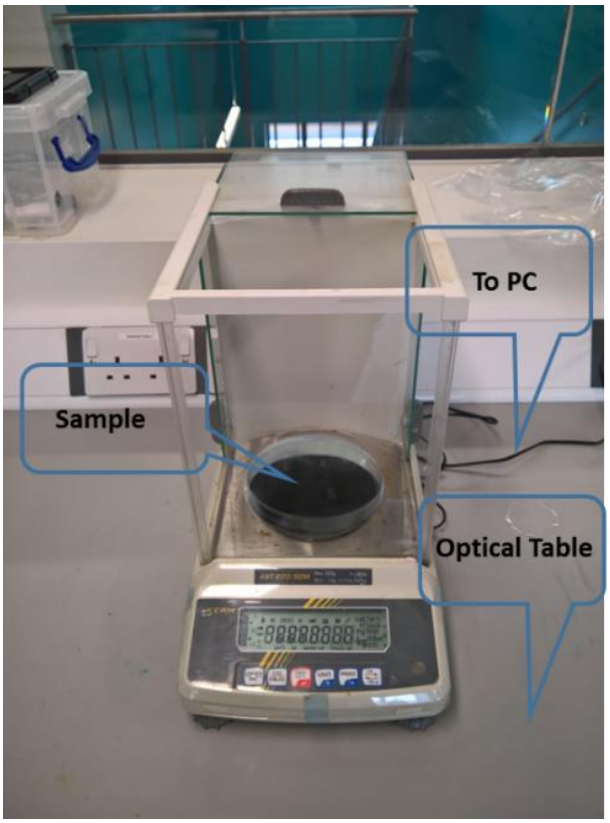

Figure 5.1 Steam absorption experimental setup.

5.4 Results and Discussions

5.4.1 Transmittance

Figure 5.2 shows the spectral transmittance (T %) of different concentrations of the nanosolutions. It is clear that aqueous lithium bromide solution is almost transparent and no significant effect of the LiBr concentration in the solution on the transparency. However, adding a low amount of carbon black nanopowder (CB) or multiwall carbon nanotubes (MWCNTs) reduces the transparency significantly. The transmittance is reduced to 0 (i.e., the samples' colour is blackish) when the concentration is 0.005 wt.% (50 mg/l ≈ 0.0025 vol.%). That means these nanosolutions can absorb the solar energy efficiently at this low concentration.

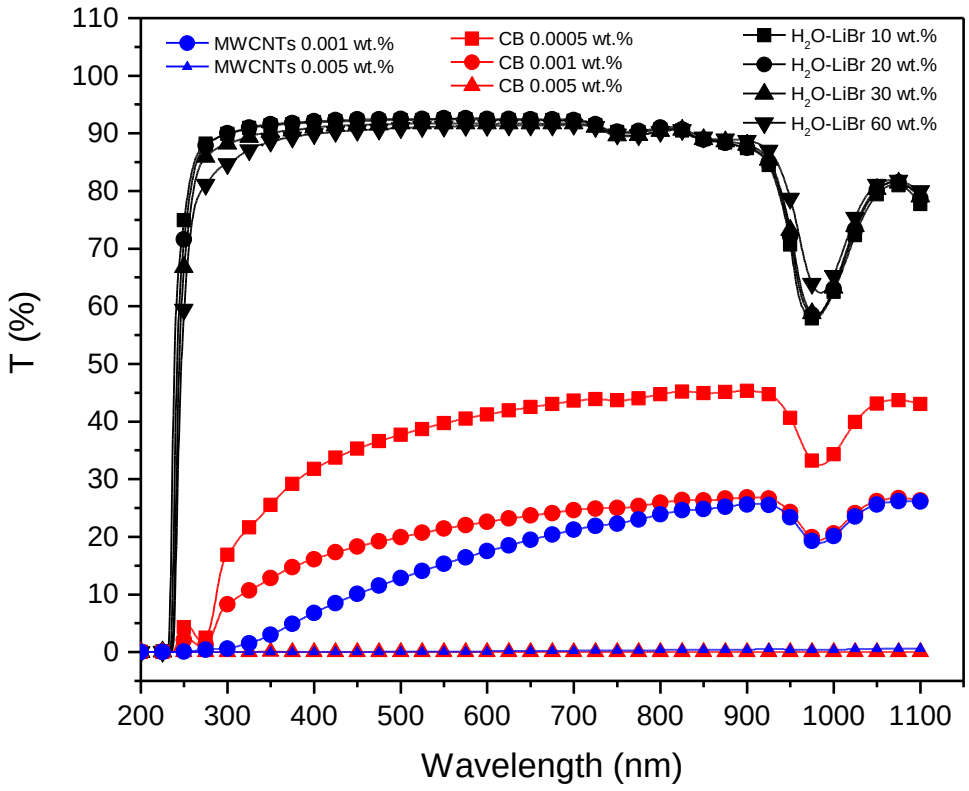

Figure 5.2 A comparison of the spectral transmittance of aqueous lithium bromide solutions without and with different nanoparticles.

5.4.2 Viscosity

Figure 5.3 shows that the dynamic viscosity of the aqueous lithium bromide solution increases nonlinearly as the solute's concentration increases. For instance, the viscosity of 60 wt.% aqueous lithium bromide solution is more than seven times higher than the viscosity of water. Good agreement is found between the results of this study with the correlations and the experimental data of Kim [34] and Wimby and Berntsson [123]. The discrepancy between this study and the correlation data is due to that the H_2O-LiBr is a very hygroscopic solution, especially at the high concentrations. Therefore, the experimental data is lower than the correlation data because of the absorbed moisture by the samples during the test. Also, it is well-known that the dynamic viscosity of the nanofluids increases as the loading of the nanoparticles and/or polymers increases. However, it is obvious, as shown in Figure 5.3 (B) and (C), that the low concentration of nanoparticles, i.e., [CB] ≤0.01 wt.% (≤100 mg/l, ≤ 0.005 vol.%), and [Gum-Arab] ≤0.1 wt.% (≤1000 mg/l) has a negligible effect on the dynamic viscosity of the nanosolutions. However, MWCNTs has a significant effect on the dynamic viscosity than CB. This difference is due to the size and the shape of the MWCNTs [124], [125].

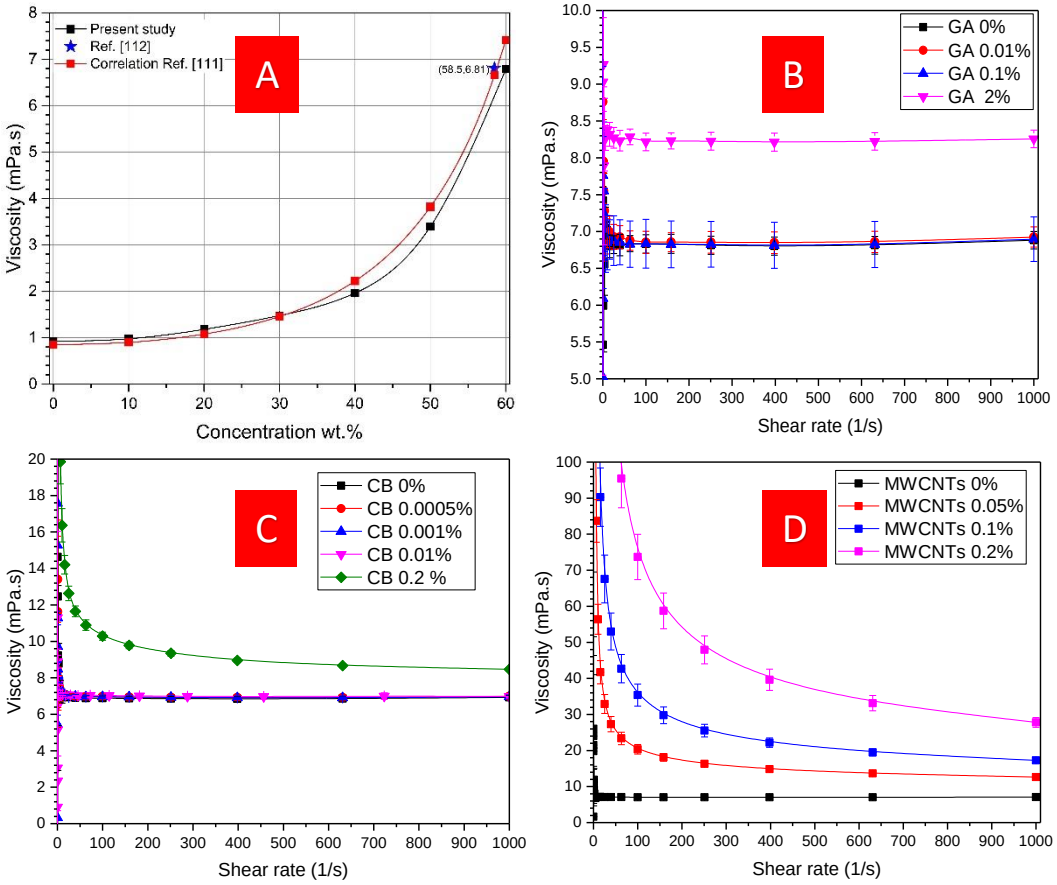

Figure 5.3: Viscosity of (A) different concentrations of aqueous lithium bromide solutions, (B) of different concentrations of GA, (C) of different concentrations of CB and (D) of different concentrations of MWCNTs to 60 wt.% aqueous lithium bromide solution.

5.4.3 Thermal conductivity

The thermal conductivity of the aqueous lithium bromide solution as a function of the solute concentration is shown in Figure 5.4 (A). The reduction of the thermal conductivity seems following a linear trend as the solution concentration increases. Good agreement is shown between the measured values of this study and the values calculated from a correlation equation presented by Wimby and Berntsson [123]. A negligible effect on the thermal conductivity can be seen in Figure 5.4 (B-D) by dissolving GA and dispersing

CB and MWCNTs in the aqueous lithium bromide 60 wt.%. The maximum enhancement of ~1.2% is achieved by 0.2 wt.% MWCNTs and an enhancement of ~0.25% by 0.05 wt.%. However, an enhancement of ~0.5% was obtained by 0.01 wt.% CB which reveals that CB can improve the thermal conductivity better than MWCNTs. This because the density of CB nanopowder and the MWCNTs are almost the same (~2 g/cm^3) and the average size of the CB is smaller than the size of MWCNTs. Consequently, more nanoparticles of CB exist in nanosolution than the MWCNTs and faster Brownian motion for the same mass concentration. However, all the results are in-between the upper and lower error limits of the device.

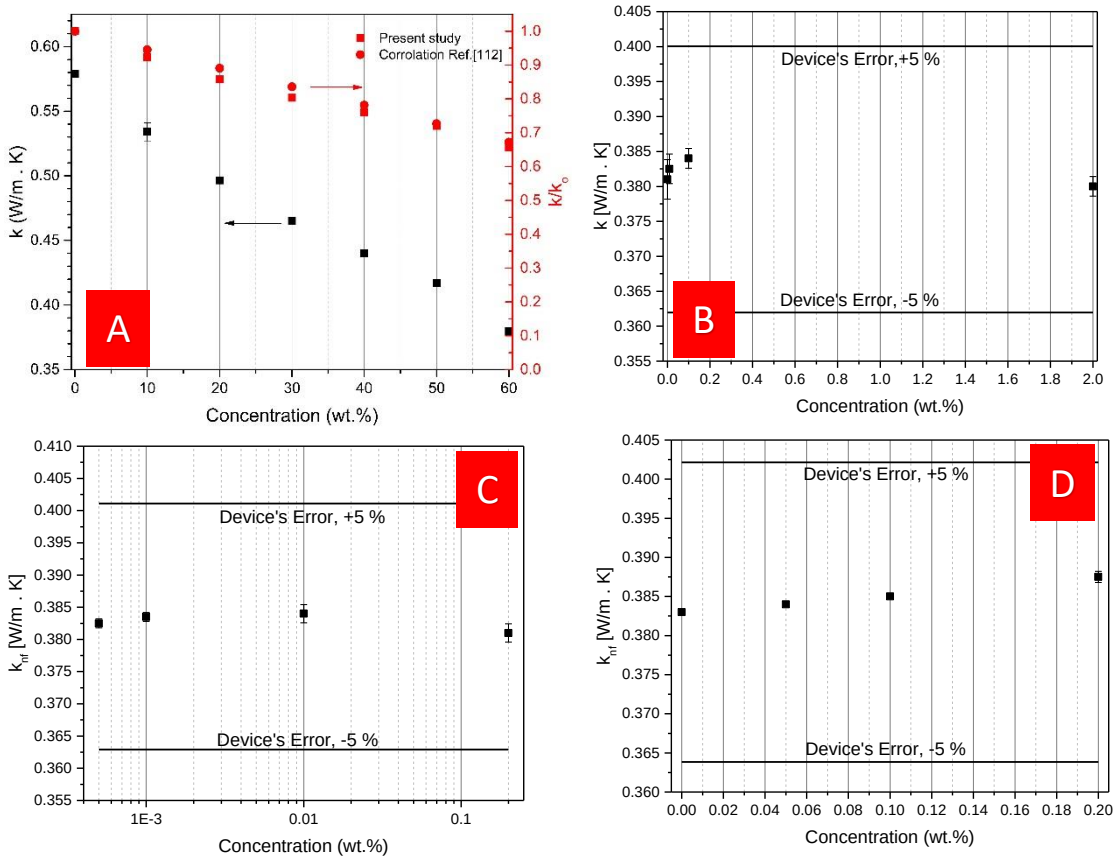

Figure 5.4 Thermal conductivity of: (A) different concentrations of aqueous lithium bromide solution, (B) different concentrations of GA, (C) different concentrations of CB and (D) different concentrations of MWCNTs in 60 wt.% aqueous lithium bromide solution.

5.4.4 Steam absorption

The effect of additives like dispersing agents, such as Tween®80 and GA, and nanoparticles, such as CB and MWCNTs, at different concentrations, which were comparable with the concentrations used by Kang et al. [46], Kim et al. [62], Lee et al. [47] and Wang et al. [50], on the steam absorption was investigated experimentally. Each set of experiments was repeated three times and the same results were obtained every time as shown in Figure 5.5.

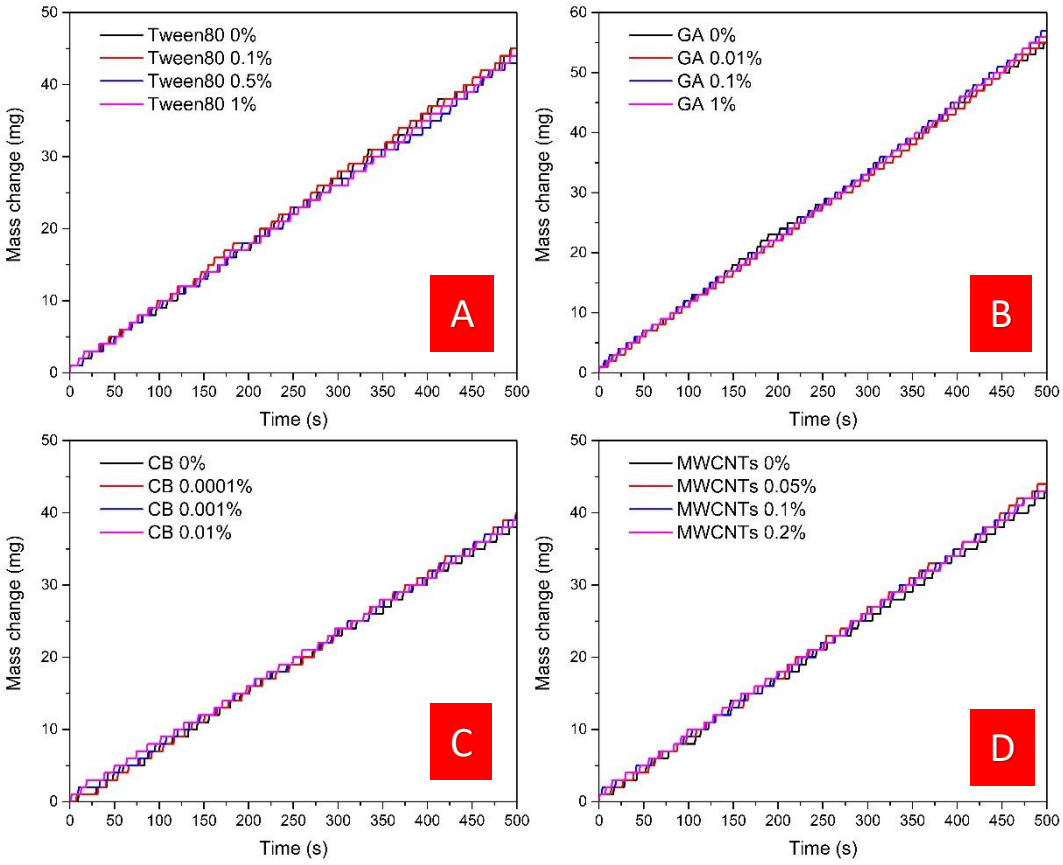

Figure 5.5 Steam absorption of different additives to 60 wt.% aqueous lithium bromide solution. (A) Tween® 80, (B) Gum-Arab, (C) Carbon black and (D) Multi-wall carbon nanotubes.

It is clear that the relationship between the samples' mass and time is linear, and there is no clear enhancement in steam absorption by adding the additives to the aqueous lithium bromide solution. These results are against the results obtained by other research groups, as shown in Table 5.1., which say that the steam absorption could be enhanced up to 210%.

Table 5.1 Performance of Nanosolutions in Falling Film Experiments

Researchers (Year)	Concentration of H2O-LiBr	NPs concentration	Dispersing agent/surfactant	Results	Reason/s
Kang et al (2008) [46]	**55 wt.%**	**0, 0.01, 0.1 wt.% of Fe (100nm),** **0, 0.01, 0.1 wt.% of CNTs (25nm,5µm)**	**GA**	**The performance of CNTs is better than Fe.** **~210% enhancement in steam absorption, while only~5% enhancement in heat transfer.**	**They believed that the NPs played a catalytic role, where the absorption rate increased in the diffusion layer near the steam/nanosolution interface, while the absorption heat didn't transfer sufficiently to the coolant through the bulk solution due to the heat and mass resistance.**
Lee et al (2009) [47]	**-**	**0, 0.01 wt.% of Al2O3**	**2E1H, GA**	**The heat transfer and absorption rate increased up to 19% and 77% respectively using 2E1H with 0.01 wt.% Al2O3. While 18% and 23% were achieved by using**	**-**

				GA with 0.01 wt.% Al2O3.	
Kim et al. (2012) [62]	**53 wt.%**	**0, 0.001, 0.005, 0.01 vol.% of SiO2 (10-20 nm)**	**150 ppm of 2E1H**	**Adding 0.005 vol.% of SiO2 without adding 2E1H increased the heat transfer and absorption rate up to 46.8% and18% respectively. While adding 2E1H reduced the enhancement to 21% and 5.5%.**	**They believed that the achieved enhancements were due to the convective characteristics of the nanoparticles such as the Brownian motion. Presence of 2E1H weakened the Brownian motion.**
Wang et al. (2018) [50]	**58 wt.%**	**0, 0.05 and 0.1 vol.% of CuO (30-50 nm)**	**GA was 5x CuO**	**Absorption rate increased as the CuO concentration increased and the solution flow rate increased.**	**They believed that the Brownian motion of the NPs and the accompanied micro-convection was the responsible factor for the absorption rate enhancement**

Although all the results in Table 5.1 show an increase in the absorption rate of the nanosolutions comparing with the base binary fluid, there are clear discrepancies among them. Kang et al. [46] showed that seeding aqueous lithium bromide with Fe or CNTs nanoparticles could enhance the steam absorption rate higher than the heat transfer. At the same mass concentration, CNTs could enhance the steam absorption rate better than Fe. While Kim et al. [62] showed that dispersing SiO_2 in aqueous lithium bromide solution could increase the heat transfer rate higher than the steam absorption rate. Also, they found that the enhancement was reduced when 2E1H was added to the nanosolution. They believed that 2E1H suppressed the Brownian motion of

the nanoparticles. However, Lee et al. [47] found that adding 2E1H with Al_2O_3 nanoparticles to an aqueous lithium bromide solution could improve the steam absorption rate significantly up to 77% at 0.01 wt.% of Al_2O_3. Brownian motion and the grazing effect of the nanoparticles were suggested as the responsible reason for the achieved enhancements.

In the falling film experiments, different factors affecting the steam absorption rate could not be controlled such as:

- The thickness of the falling film. The thicker falling film is, the higher heat and mass transfer resistances are, leading to a lower absorption rate.
- The surface area of the falling film. The larger surface area is, the higher absorption rate is.
- The existence of volatile surfactants such as 2E1H and n-octanol. The access existence of these surfactants on the interface surface area between the falling nanosolution and vapour phase causes uneven surface tension of the interface, produces Marangoni convection, which leads to good mixing in the falling film and better heat and mass transfer rates. Consequently, the absorption rate is better.

These effective factors make it difficult to judge that the enhancement was due to the Brownian motion of the nanoparticles seeded in the solution. In present work, these effective factors were controlled, where the thickness and the surface area were fixed. Moreover, volatile surfactants were not added. Also, measuring the mass change of the sample directly by using precise analytical balance made the results more reliable than that were obtained from the falling film experiments as the latter used different measuring devices such

as flow meters, thermocouples, pressure sensors, and concentration sensors. All these measuring devices increase the uncertainty of the measurements. The results of this work reveal that the significant enhancement in steam absorption achieved by previous studies on falling films cannot be due to Brownian motion and/or the grazing effect of the nanoparticles. This is can be understood because:

- Brownian motion of particles in a liquid is the result of the random collisions of the liquid molecules with these particles and between the particles themselves. This motion is time-invariant, i.e., it looks the same going forward as looks going backwards. The smaller the particle is, the probability of long jump is more likely than the short one, while the bigger particle is, the shorter jump is more likely than longer one [126]. Since these nanosolutions were prepared by the two-step method (dispersing nanopowder in solutions), these particles are more likely to be in clusters and aggregates making big particles, usually in sub-micron size, bouncing around themselves in short jumps.
- At the same low particle concentrations, the inter-distances among bigger particles (micro or sub-micron size) are longer than that among small particles (nano-size). This makes the possibility of collision among big particles much lower. This is can be demonstrated if spherical particles are assumed to be homogeneously distributed in 1-litre volume cube as shown in Figure 5.6. The average particle's diameter is d and the inter-distance between two adjacent particles in a raw or a column is L. The length of each edge of the cube is 10 cm. The mass concentration of the particles in a volume of fluid is:

$$\rho = \frac{m_{np}}{V_f} \qquad \text{[mg/l]}\ldots\ldots\ldots (1)$$

where m_{np} is the mass of the particles; V_f is the total volume ≈ the fluid volume. The volumetric concentration of the particles in a volume of fluid is:

$$\emptyset = \frac{V_{np}}{V_f} \qquad \text{[l/l]}\ldots\ldots\ldots\ldots (2)$$

where V_{np} is the solid volume of the particles.

$$V_{np} = N_{np} * \ v_{np} * 10^{-24} \qquad \text{[l]}\ldots\ldots (3)$$

where $N_{np}$is the total number of the particles;v_{np} is the average volume of one particle and $1\ nm^3 = 10^{-24} litre$.

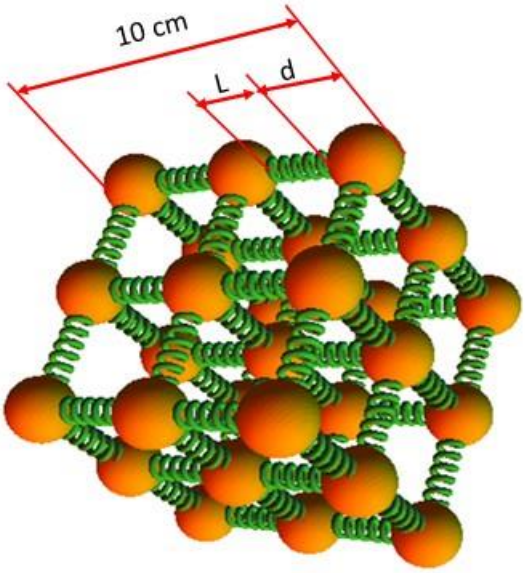

Figure 5.6 Schematic of homogeneously distributed particles in a cube of one litre.

$$v_{np} = \frac{4}{3}\pi\, r_{np}^3 \ \text{[nm]}\ldots\ldots (4)$$

The number of particles distributed on one edge is $\sqrt[3]{N_{np}}$; therefore, the edge length can be represented as:

$$0.1 * 10^9 = \sqrt[3]{N_{np}} * d_{np} + \left(\sqrt[3]{N_{np}} - 1\right)L \quad \text{[nm]}\ldots..(5)$$

$$L = \frac{10^8 - \sqrt[3]{N_{np}} * d_{np}}{\sqrt[3]{N_{np}} - 1} \approx \frac{10^8 - \sqrt[3]{N_{np}} * d_{np}}{\sqrt[3]{N_{np}}} \quad \text{[nm]}\ldots\ldots\ldots\ldots(6)$$

where L is the distance between two adjacent particles in a row or a column. The inter-distance between adjacent particles is shown in Figure 5.7. It is clear that the relationship between the inter-distance and the particle's diameter is linear with a slop significantly affected by the concentration, i.e., the lower concentration is, the higher slope is, as shown in Figure 5.7 (A). While Figure 5.7 (B) shows a nonlinear relationship between the inter-distance of adjacent particles and the concentration, especially for bigger particles.

Therefore, it is believable that the achieved enhancement in the falling film experiments was not due to the Brownian motion or the grazing effect of the nanoparticles suspended in the solution, but it was due to the accompanied surface turbulence and wettability enhancement. It is well known that addition of a proper alcoholic surfactant (such as n-octanol or 2E1H, which were used in the previous studies) to the H_2O-LiBr solution causes a vigorous surface instability (i.e., Marangoni convection), which is a result of surface tension gradient generated from heterogeneous mass concentration distribution of the surfactant on the solution's surface. This vigorous surface instability improves

the mass transfer considerably [40], [54], [55]. Also, it is known that surfactants enhance the wettability by reducing the surface tension of liquids, which consequently increase the transfer area.

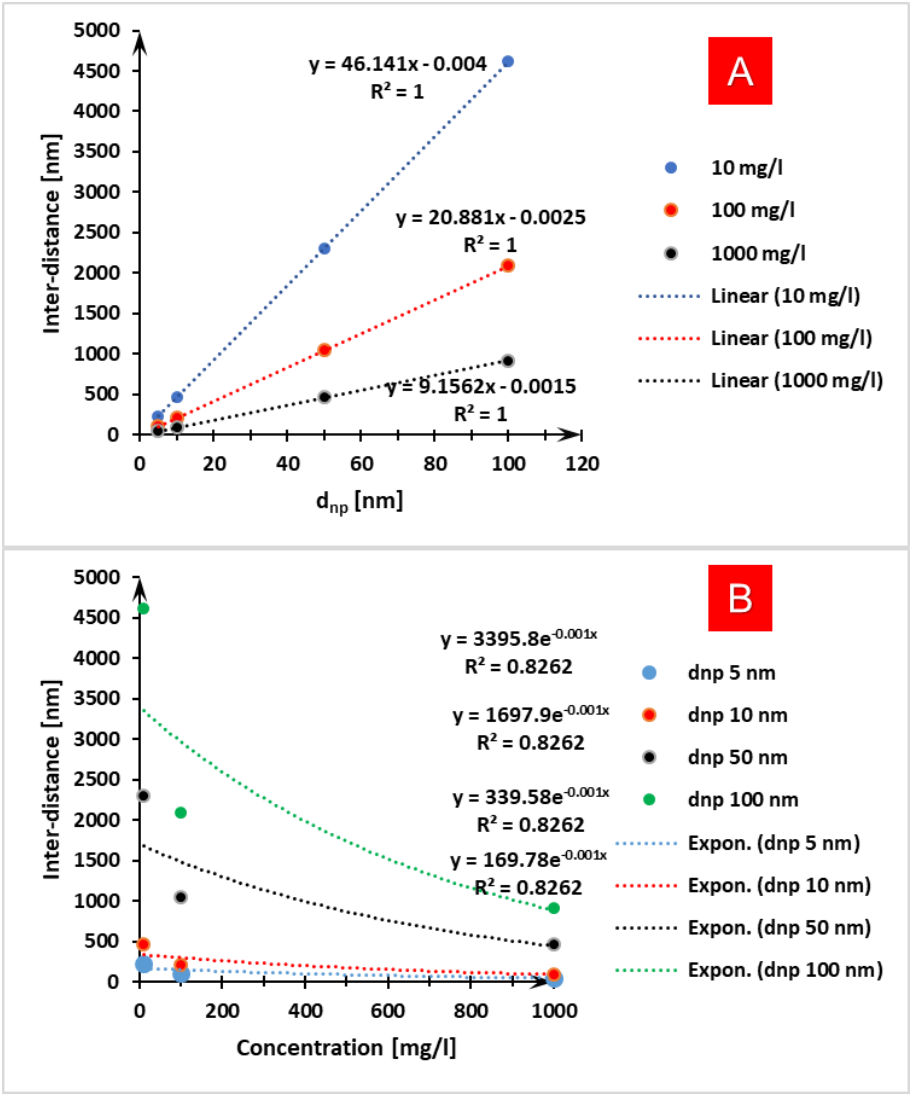

Figure 5.7 The inter-distance between two adjacent particles as a function of (A) the particle's diameter at constant colloid concentration and (B) as a function of the colloid concentration at constant particle's diameter.

5.4.5 Steam generation

The results of the photo-thermal conversion experiments of binary fluids are presented in Figure 5.8. The temperature and mass change of the aqueous LiBr solution with and without nanoparticles are shown. The first 30 min represents the heating up of the samples under solar radiation of 850 W/m^2. It is clear that both samples undergo temperature increase due to the photo-thermal conversion. However, the maximum temperature of the nanosolution (i.e., [CB] = 0.005 wt.%) is ~63 ^{o}C, while the maximum temperature of the aqueous LiBr solution (i.e., [CB] = 0 wt.%) is ~52 ^{o}C. The jump in the temperature is due to the enhancement of the light absorption of the nanosolution achieved by seeding nanoparticles, as shown in Figure 5.2.

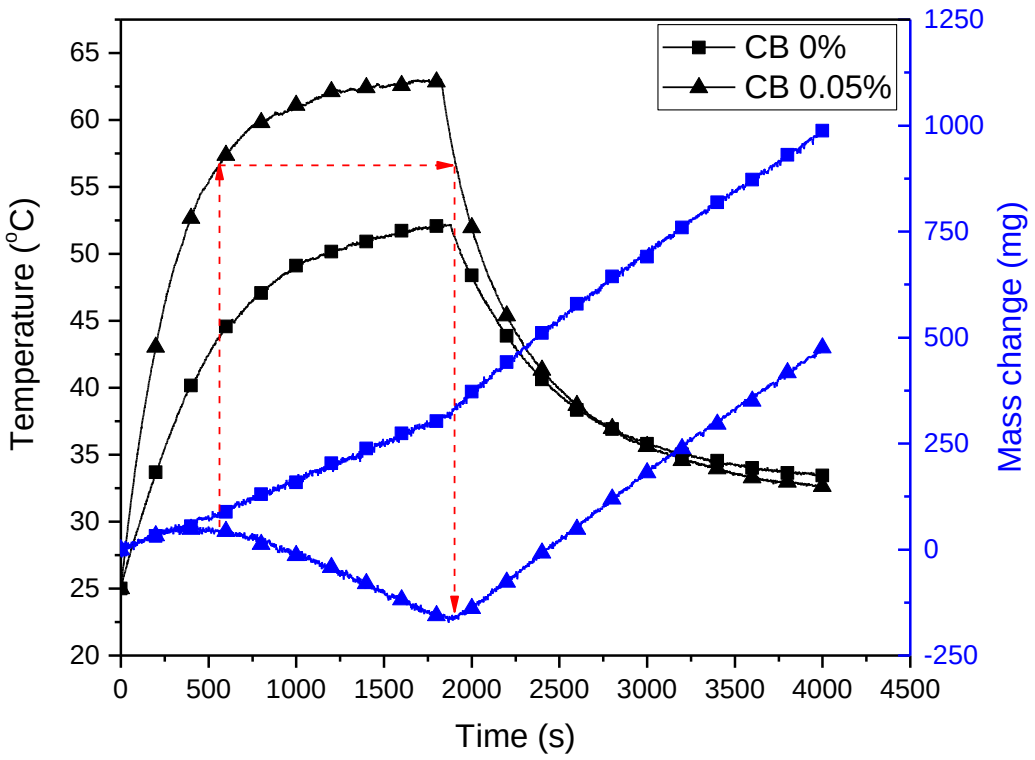

Figure 5.8 Temperature and mass change of nanosolutions at 0 wt.% and 0.005 wt.% CB. Light intensity is 850 W/m^2.

For both samples, the mass change continuously increases until time ~540 s. After that, the mass change of the nanosolution (i.e., [CB] = 0.005wt.%) starts to decrease when the temperature becomes ≥ 56.5^{o}C, which represents a threshold point. At that point, the steam generation rate is equal to the steam absorption rate. Below that point, the steam absorption rate is higher than the steam generation rate; therefore, the net mass change increases. After the threshold point, the steam generation rate is higher than the steam absorption rate; therefore, the net mass change decreases. However, the mass change of the aqueous LiBr solution (i.e., [CB] = 0 wt.%) continues in the increasing trend as it never reaches the threshold point. The second period represents the cooling down of the samples under no radiation (i.e., the solar simulator is turned off), and the samples' temperature starts to decrease to reach the steady state temperature. The mass change of both samples starts again to increase at higher rates as the nanosolution's temperature reaches the threshold temperature soon.

Different CB concentrations, namely 0, 25 mg/l (~0.0025 wt.%), 50 mg/l (~0.005 wt.%), and 100 mg/l (~0.01 wt.%) in 50 wt.% aqueous lithium bromide solution were used to investigate the photo-thermal conversion of the nanosolutions at higher solar radiation (10 Suns). Figure 5.9(A) represents the temperature rise due to the photo-thermal conversion of the nanosolutions recorded by a thermocouple positioned ~2mm under the air/nanosolution interface for 15 min. While Figure 5.9(B) shows the temporary mass reduction of the nanosolutions due to the evaporated mass of water. Figure 5.9(C) shows the steam generation rate with time. These results are similar, in trend,

to the results shown in Chapter 4. In other words, the higher the nanoparticles concentration and/or the higher the light intensity is, the higher temperature of the nanosolution near the air/nanosolution interface, which means that higher kinetic energy of the water molecules near the interface. Consequently, a higher steam generation rate is achieved.

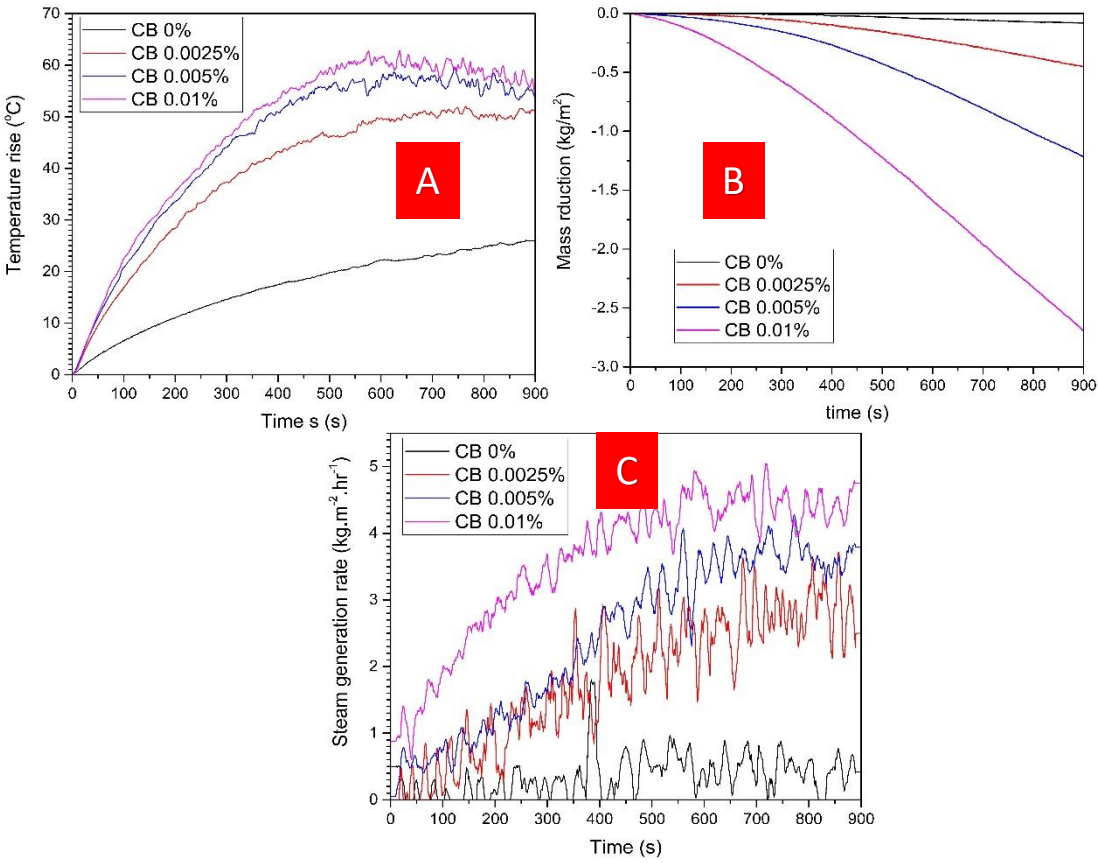

Figure 5.9 Photo-thermal conversion of different CB concentrations in 50 wt.% aqueous lithium bromide solution under 10 Suns irradiance. (A) Temperature rise of the nanosolutions, (B) mass reduction of the nanosolutions and (C) steam generation rate as function of time.

The common operating pressure and temperature of a generator in a single effect H_2O-LiBr absorption refrigeration system are 0.05-0.15 bar and 70-120^oC respectively and the COP ranges between 0.6-0.8. The generator must generate ~1.4-1.5 g/s of steam for each 1 TR (~3.5 kW) cooling effect [127], [128]. Assuming the highest COP, i.e., 0.8, the generator must be supplied with 4.375 kW of heat in order to produce 3.5 kW cooling effect by the VARS. To supply that amount of heat from the sun, 5.5 m^2 flat plate solar collectors of 80% efficiency are required to produce 1.4-1.5 g/s of steam. While ~4.5 kg/m^2 hr (1.25 g/m^2 s) can be produced by illuminating a 0.01 % CB nanosolution with 10 kW/m^2 solar radiation. In other words, 1.12-1.2 m^2 of the nanosolution is needed to be illuminated to produce a 3.5 kW cooling effect. Moreover, the steam generation rate from the nanosolutions was produced at atmospheric pressure, which is much higher than the common pressure of the generator. Therefore, it is expected that higher steam generation rates could be achieved if the illuminated nanosolution was at sub-atmospheric pressure equals to the generator pressure.

5.5 Chapter Summary

In this chapter, the effects of adding nanoparticles (CB and MWCNTs) and some dispersing agents (Tween® 80 and Gum-Arabic) to aqueous lithium bromide solutions were investigated experimentally. The main findings are:

- Dispersing a very low amount of low-cost CB nanopowder 0.005 wt.% in the aqueous lithium bromide solution reduces the transparency to zero. The solar steam generation experiment shows that the

nanosolution has the potential for use in direct solar absorption refrigeration systems.

- Within the range of the mass concentrations used in this study - which is comparable with ranges adopted in the literature - there is a negligible effect of Brownian motion on the steam absorption rate.
- Low loading of nanoparticles and dispersing agents have a negligible effect on the thermal conductivity and the dynamic viscosity of the nanosolutions. However, MWCNTs increases the dynamic viscosity higher than the CB at the same mass concentration.

Chapter 6

CONCLUSION AND FUTURE WORK

6.1 Conclusions

Vapour-compression refrigeration systems (VCRSs) consume a lot of electrical power. Using this type of refrigeration systems to overcome the extreme weather patterns (i.e., the searing summer and cold winter) adds high loads on the national grids, and makes the global warming issue even worse. While the other approach of using vapour-absorption refrigeration systems (VARSs), driven thermally from renewable energy sources such as the Sun, is more likely to solve this problem for the long term. On the other hand, the utilisation of solar energy is attractive as the peak cooling load is associated with the high solar radiation; therefore, heat captured from the Sun could provide the VARSs with the required energy totally or partially. However, solar-driven VARSs are costlier than VCRSs (~5 times higher) due to the need of generating the power locally using solar collectors, storage tank and plumbing fittings. That is in addition to the large heat exchangers (absorber, solution heat exchanger and generator) requirements due to the low heat and mass transfer characteristics of the absorption solution (aqueous lithium bromide), i.e. low thermal conductivity and specific heat capacity and high viscosity and surface tension. For that reason, improving the efficiency of the solar-driven VARSs components (namely the solar collectors, generators and absorbers) could potentially increase the overall performance of the system, as well as reduce its size and cost.

This work presents a novel concept of using direct absorptive nanofluids or nanosolutions to drive the solar VARSs and to improve the heat and mass transfer characteristics of the absorption solution. The main functions of these nanofluids or nanosolutions are to:

1- Overcome the surface limitation associated with the conventional SCs, which consist of absorptive plates that capture the solar energy and transfer it to a running fluid inside tubes. As this process is not only limited to how efficiently the solar energy is captured by these absorptive plates, but also how effectively the captured energy is transferred to the running fluid, the concept of seeding direct absorptive nanoparticles in working fluids is proposed. Due to the high surface area to volume ratio and the high light absorbance characteristics of the nanoparticles, this concept could capture the solar energy in an efficient way to desorb the refrigerant (water) in the generator.

2- Improve the low heat and mass transfer characteristics of the aqueous lithium bromide solution. Seeding nanoparticles in the aqueous lithium bromide solution can affect some physio-thermal properties such as the thermal conductivity, surface tension and wettability, and viscosity. Furthermore, some publications suggested the Brownian motion of the seeded nanoparticles as an intensive booster for steam absorption in the absorber.

In this work, the photo-thermal conversion performance of different nanofluids such as Au, Cu, Au-Cu hybrids and CB nanofluids was experimentally investigated in terms of radiation absorption, temperature change, photo-

thermal conversion efficiency, specific absorption rate, and steam generation. The main conclusions drawn from a series of experiments are listed below:

- With photo-thermal conversion enhancements of ~124% and ~50% for CB and Au nanofluids respectively, the blackish nanofluids, such as carbon-based nanofluids (CB), harvest the solar energy more efficiently than colourful nanofluids, such as Au and Cu nanofluids. This can be explained as, blackish nanofluids absorb the visible radiation spectrum completely, while colourful nanofluids transmit and/or scatter some of the visible radiation spectrum. The results of the UV-Vis spectrophotometer showed that the absorbance of the CB nanofluid was outweighing the absorbance of the Au and Cu nanofluids at the same nanoparticles concentration. Moreover, the results of the photo-thermal conversion experiments justified this point.
- Blending two or more nanofluids having a narrow absorbance bandwidth, such as Au and Cu nanofluids, extends the absorbance bandwidth of the resultant hybrid nanofluid, but reduces the absorbance value due to the dilution of the original nanofluids. This claim was proved experimentally by measuring the absorbance of a hybrid via a spectrophotometer. Moreover, the claim was proved via photo-thermal conversion experiments for different hybrids. This point is in consistency with Beer's law.
- The experiments proved that, for a fluid containing absorbing particles, the light intensity absorbed within the fluid follows an exponential decay function of the extinction coefficient and the light path length. Furthermore, the rate of change of the absorbed light is proportional to the incident light intensity and the extinction coefficient. In other words,

the higher nanoparticles concentration and/or incident light intensity is, the more light is absorbed in a thinner layer near the incident interface, leading to an obvious temperature gradient within the nanofluid. The highest temperature is near the surface of the incident light on the nanofluid. This temperature gradient is a key cause for the discrepancy in the photo-thermal conversion efficiency seen in the literature.

- In addition to the higher photo-thermal conversion efficiency of CB nanofluids, Au nanofluids are not feasible for a solar steam generation since the cost of producing 1g/s steam is ~300 times higher than the steam generation by CB nanofluids at the same nanoparticles mass concentrations.
- For a solar steam generation, this study showed that using black, thin porous media and a thermal isolating board is more efficient than nanofluids. The black porous medium can absorb the solar energy in a micro-size thin layer, and the thermal isolating board suppresses the heat conduction to the bulk fluid effectively.

Also, the effect of the seeding CB and MWCNTs, in addition to the use of non-volatile dispersing agents (GA and Tween®80), on the steam absorption capability of the aqueous lithium bromide solution was experimentally investigated. In this study, the constant mass transfer surface area and thickness of the samples were adopted to avoid the uncertainties of the surface area and thickness values accompanied by the falling film experiments. Moreover, the direct measurement of the samples' mass using a precise analytical balance was adopted to avoid the uncertainties in the calculation of the steam absorption rates by using different measuring devices

(pressure sensor, thermocouples, flow meters, and concentration measuring devices). Although this work used comparable nanoparticle concentrations with previous studies, the results of this work showed negligible change in the steam absorption rate as a function to the additives (nanoparticles and dispersing agents) concentration, which are against the findings published by other research groups suggesting that Brownian motion could enhance the steam absorption rate up to 210%. We explained this discrepancy as follows:

Although the Brownian motion exists as the nanoparticles exist in a fluid, which is due to the uneven momentum transfer during the collisions between the fluid's molecules and the particles and between the particles themselves, the intensity of this motion is dependent on the size and the concentration of these particles. The bigger and fewer nanoparticles are, the longer inter-distances among nanoparticles are, and time-invariant Brownian motion with short jumps is. Therefore, it is believable that the Brownian motion and the grazing effect of these low concentrations and relatively big nanoparticles seeded in the aqueous lithium bromide solution have negligible effects on the steam absorption rate. It is concluded that, the enhancement in the mass transfer seen in the literature is not due to the Brownian motion of the nanoparticles, but it is due to the enhancement in the wettability and Marangoni convection since these literature studies used 2E1H and/or n-octanol, which their generation for vigorous surface instability (Marangoni effect) is proven.

The thermal conductivity and dynamic viscosity of different nanosolutions were also examined, and the main results are:

- The experiments showed negligible change in the thermal conductivity of the nanosolutions using CB nanopowder and MWCNTs at concentrations reached 0.2 wt.%. Moreover, adding a dispersing agent such as Gum-Arabic has also a negligible effect on the thermal conductivity.
- Effect of MWCNTs on the viscosity of the nanoslution is higher than the effect of the CB nanopowder at the same concentration.

In summary, using cheap CB nanofluids can fulfil scenario #1 mentioned in Chapter 1, i.e., harvesting the solar energy and converting it into thermal energy. The thermal energy is stored in a thermal storage tank to utilise it later in driving the generator to produce the required steam generation rate. Furthermore, seeding cheap CB nanopowder in aqueous lithium bromide can fulfil a part of scenario #2. In other words, the nanosolution is pumped from the absorber (A) through the solution heat exchanger (SHX) to pass through a direct absorption solar collector. In the direct absorption solar collector, the solar energy is harvested and converted into heat directly by the nanoparticles, increasing the temperature of the nanosolution to the required temperature. Then, the hot nanosolution is sprayed on to the tubes bundle in the generator to generate the refrigerant vapour (steam) from the falling film. The generated refrigerant vapour passes through the condenser to complete the cycle of refrigeration as described in the subsections 1.1.1 and 1.1.2. Although the experimental results of this work show negligible change in the steam absorption rate by seeding nanoparticles in aqueous lithium bromide solutions (it is believable that the low concentration and the big size of the nanoparticles are responsible for the negligible enhancement in the refrigerant vapour absorption), the concept of using direct absorptive nanofluids to drive

solar VARSs is still viable. Feasible direct absorptive nanofluids (such as CB nanofluids) can absorb the solar energy directly and efficiently, converting it to thermal energy to desorb the refrigerant (steam) in the generator. This technique can be used in the rural areas far away from electricity supply grids, and even in the cities to relief the grids from the high loads resulting from using electric VCRSs and to save the earth from extra GHG.

6.2 Future Work

The direct absorptive nanofluids were proposed to improve the performance of the solar-driven VARSs. These nanofluids were examined in terms of the direct solar absorption, steam generation and absorption, and thermo-physical properties (thermal conductivity and viscosity). Although the very low concentration of carbon-based nanoparticles can absorb most the solar energy, these low concentrations have negligible improving effects on the steam absorption and the thermal conductivity. Therefore, the following recommendations are to explore the feasibility of using nanofluids in solar-driven VARSs more deeply:

1. It is believable that, the low nanoparticle concentrations are responsible for the unchanged thermal conductivity and mass transfer as the communication between the nanoparticles (collisions) is poor due to the long inter-distance among the big particles and the weak Brownian motion. Therefore, the synthesis of nanofluids with high volumetric concentrations of very small nanoparticles (<10 nm), such as carbon dots, can overcome this problem. Investigating the radiative absorptivity, thermal conductivity, heat transfer coefficient and the

viscosity is preferable. Blending suitable nanofluids might be a good choice to prepare a hybrid has the preferable physio-thermal properties, such as high radiation absorptivity, high thermal conductivity and high heat transfer coefficient.

2. It was noticed that the long-term stability of the nanosolutions is a problematic matter, especially for high nanoparticle concentrations. Therefore, intensive knowledge in the aggregation mechanisms and stabilisation measures is crucial to synthesize stable nanosolutions. To the best of our knowledge, the nano-emulsions technique is really interesting to produce stable nanofluids among one-step methods.
3. It is well known that crystallisation, which is one of the drawbacks of H_2O-LiBr-based VARSs, can be initiated when LiBr concentration becomes high and the temperature becomes low enough in the absorber. Big crystals can block the nozzles or the dripping orifices in the absorber.

   During this project, it was noticed that adding nanoparticles to lithium bromide solution can prevent the generation of big lithium bromide crystals at low temperatures, where samples of aqueous lithium bromide with and without nanoparticles were put in a fridge over a night and the result was a very clear sedimentation for the big LiBr crystals in the aqueous lithium bromide solution without nanoparticles, while no clear sedimentation of big crystals was seen in case of aqueous lithium bromide solution seeded with nanoparticles as shown clearly in Figure 6.1. This interesting experiment was repeated many times with different nanoparticle and the result was the same. The preliminary result of the differential scanning calorimeter showed that crystallisation happens at

higher temperatures in the nanoparticles seeded solutions than the temperature of the pure solution. A hypothesis was suggested to explain this finding as follows:

Adding nanoparticles to the aqueous lithium bromide solution offers a huge number of nucleation sites, which leads to producing a thin layer of LiBr crystals around the nanoparticles. The complexes of nanoparticles and the LiBr layers are small enough to be suspended in the solution. However, this hypothesis needs to a proof. Intensive knowledge in nucleation and crystallisation mechanics are required. This finding is a positive gain from the seeding nanoparticles in the absorption solution.

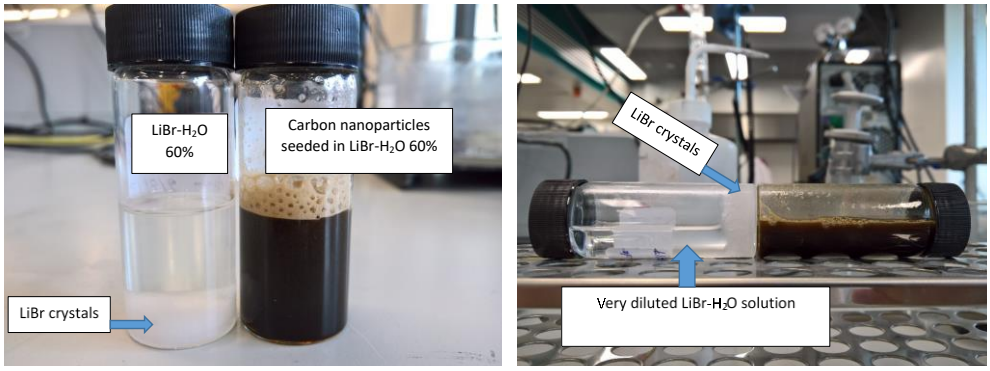

Figure 6.1 Nanoparticles' effect on the size of LiBr crytals.

List of References

[1] G. F. HUNDY, A. R. TROTT, and T. C. WELCH, *REFRIGERATION, AIR CONDITIONING AND HEAT PUMPS*, 5th ed. Butterworth-Heinemann, 2016.

[2] H. W. I. Stanford, *HVAC Water Chillers and Cooling Towers: Fundamentals, Application, and Operation*, 2nd ed. Taylor & Francis Group, LLC, 2012.

[3] K. E. Herold, R. Rademacher, and S. A.Klein, *Absorbtion Chillers and Heat Pumps*, 2nd ed. Taylor & Francis Group, LLC, 2016.

[4] W. P. Jones, “Vapour absorption refrigeration,” in *Air conditioning engineering*, 5th ed., pp. 399–410.

[5] A. Ghafoor and A. Munir, “Worldwide overview of solar thermal cooling technologies,” *Renew. Sustain. Energy Rev.*, vol. 43, pp. 763–774, 2015.

[6] H.-T. Pao and C.-M. Tsai, “CO2 emissions, energy consumption and economic growth in BRIC countries,” *Energy Policy*, vol. 38, no. 12, pp. 7850–7860, Dec. 2010.

[7] W. E. E. Alnaser and N. W. W. Alnaser, “The status of renewable energy in the GCC countries,” *Renew. Sustain. Energy Rev.*, vol. 15, no. 6, pp. 3074–3098, 2011.

[8] C. Li *et al.*, “Interaction between urban microclimate and electric air-conditioning energy consumption during high temperature season,”

Appl. Energy, vol. 117, no. June, pp. 149–156, Mar. 2014.

[9] G. Wilkenfeld, “A national demand management strategy for small airconditioners: the role of the National Appliance and Equipment Energy Efficiency Program (NAEEEP),” *Sydney, NSW Georg. Wilkenfeld Assoc. Natl. Appl. Equip. Energy Effic. Comm. Aust. Greenh. Off.*, 2004.

[10] T. N. T. Lam, K. K. W. Wan, S. L. Wong, and J. C. Lam, “Impact of climate change on commercial sector air conditioning energy consumption in subtropical Hong Kong,” *Appl. Energy*, vol. 87, no. 7, pp. 2321–2327, 2010.

[11] U.S. Energy Information Administration, “International Energy Outlook 2017 Overview,” 2017.

[12] I. Sarbu, “A review on substitution strategy of non-ecological refrigerants from vapour compression-based refrigeration, air-conditioning and heat pump systems,” *Int. J. Refrig.*, vol. 46, pp. 123–141, 2014.

[13] United Nations, Department of Economic and Social Affairs, Population Division, “The impact of population momentum on future population growth,” 2017. [Online]. Available: http://www.un.org/en/development/desa/population/publications/pdf/popfacts/PopFacts_2017-4.pdf. [Accessed: 30-Mar-2018].

[14] United Nations, Department of Economic and Social Affairs, Statistics Division, “Energy Statistics Yearbook,” 2015. [Online]. Available: https://unstats.un.org/unsD/energy/yearbook/default.htm. [Accessed: 31-Mar-2018].

[15] International Energy Agency, “World Energy Outlook,” 2017. [Online]. Available: https://www.iea.org/weo2017/. [Accessed: 02-Apr-2018].

[16] U.S. Energy Information Administration, “Energy-related CO2 emissions,” in *International Energy Outlook 2016*, 2016, pp. 139–148.

[17] United Nations, “Sustainable Development Goals.” [Online]. Available: http://www.un.org/sustainabledevelopment/climate-change-2/. [Accessed: 02-Apr-2018].

[18] United States Environmental Protection Agency, “Greenhouse Gas Emissions.” [Online]. Available: https://www.epa.gov/ghgemissions/overview-greenhouse-gases. [Accessed: 01-Apr-2018].

[19] International Energy Agency IEA, *Solar Energy Perspectives*. 2011.

[20] Z. Y. Xu, R. Z. Wang, and H. B. Wang, “Experimental evaluation of a variable effect LiBr-water absorption chiller designed for high-efficient solar cooling system,” *Int. J. Refrig.*, 2015.

[21] Absotherm Services, “Yazaki-Over 30 Years of Pioneering Absorption.” [Online]. Available: http://www.absothermservices.com/sitecontrol/pdf/Yazaki_Brochure.pdf. [Accessed: 04-Apr-2018].

[22] Maya-Yazaki, “Yazaki Water Fired Absorption chiller series S cutaway.” [Online]. Available: http://www.maya-airconditioning.com/eng/index.html. [Accessed: 27-Jul-2018].

[23] R. Heyd, “Nanofluids for Heat Transfer,” in *Two Phase Flow, Phase Change and Numerical Modeling*, A. Ahsan, Ed. In Tech, 2011.

[24] T. Elen V, “Nanofluids for Heat Transfer – Potential and Engineering Strategies,” in *Two Phase Flow, Phase Change and Numerical Modeling*, A. Ahsan, Ed. Institution of Chemical Engineers, 2011.

[25] T. P. Otanicar, P. E. Phelan, R. S. Prasher, G. Rosengarten, and R. A. Taylor, “Nanofluid-based direct absorption solar collector,” *J. Renew. Sustain. Energy*, vol. 2, no. 3, p. 033102, May 2010.

[26] M. Al Juma, “Solar absorption cycle for cooling/refrigeration,” Cardiff University, 2014.

[27] Bureau International des Expositions (BIE), “Expo 1878 Paris: The revelation of Sun Power.” [Online]. Available: https://www.bie-paris.org/site/en/blog/entry/expo-1878-paris-the-revelation-of-sun-power. [Accessed: 06-May-2018].

[28] S. A. Kalogirou, “Solar Space Heating and Cooling,” in *Solar Energy Engineering*, 2009, pp. 315–389.

[29] K. E. Herold, “Design challenges in absorption chillers,” *Mech. Eng.*, vol. 117, no. 10, p. 80, 1995.

[30] M. A. Hammad and M. S. Audi, “Performance of a solar LiBr-water absorption refrigeration system,” *Renew. Energy*, vol. 2, no. 3, pp. 275–282, 1992.

[31] M. Hammad and Y. Zurigat, “Performance of a second generation solar cooling unit,” *Sol. Energy*, vol. 62, no. 2, pp. 79–84, 1998.

[32] H. E. Zinian and Z. Ning, “A solar absorption air-conditioning plant using heat-pipe evacuated tubular collectors,” in *Proceedings of ISES Solar World Congress on CD-ROM, Jerusalem, Israel*, 1999.

[33] D. S. Kim and C. A. Infante Ferreira, “Solar refrigeration options - a state-of-the-art review,” *Int. J. Refrig.*, vol. 31, no. 1, pp. 3–15, 2008.

[34] D. S. Kim, “Solar absorption cooling,” Korea University, 2007.

[35] R. Nasr Isfahani and S. Moghaddam, “Absorption characteristics of lithium bromide (LiBr) solution constrained by superhydrophobic nanofibrous structures,” *Int. J. Heat Mass Transf.*, vol. 63, pp. 82–90, 2013.

[36] R. Nasr Isfahani, K. Sampath, and S. Moghaddam, “Nanofibrous membrane-based absorption refrigeration system,” *Int. J. Refrig.*, vol. 36, no. 8, pp. 2297–2307, 2013.

[37] S. A. Klein and D. T. Reindl, “Solar refrigeration,” *ASHRAE J.*, vol. 47, no. 9, p. S26, 2005.

[38] J. D. Killion and S. Garimella, “A Review of Experimental Investigations of Absorption of Water Vapor in Liquid Films Falling Over Horizontal Tubes,” *HVAC&R Res.*, vol. 9, no. 2, pp. 37–41, 2003.

[39] C. Amaris, M. Bourouis, M. Vallès, D. Salavera, and A. Coronas, “Thermophysical Properties and Heat and Mass Transfer of New Working Fluids in Plate Heat Exchangers for Absorption Refrigeration Systems,” *Heat Transf. Eng.*, vol. 36, no. 4, pp. 388–395, 2014.

[40] A. De Lucas, M. Donate, and J. F. Rodríguez, “Applying surfactants to improve the absorption capacity of mixtures of lithium bromide and formates in absorption refrigeration coolers,” *Int. J. Refrig.*, vol. 31, no. 6, pp. 1073–1080, 2008.

[41] L. Weng, W. Song, D. J. Jacobs, and G. D. Elliott, “Molecular insights

into water vapor absorption by aqueous lithium bromide and lithium bromide/sodium formate solutions," *Appl. Therm. Eng.*, vol. 102, pp. 125–133, 2016.

[42] S. B. Riffat, S. E. James, and C. W. Wong, "Experimental analysis of the absorption and desorption rates of HCOOK/H2O and LiBr/H2O," *Int. J. Energy Res.*, vol. 22, no. 12, pp. 1099–1103, 1998.

[43] M. Donate, L. Rodriguez, A. De Lucas, and J. F. Rodr??guez, "Thermodynamic evaluation of new absorbent mixtures of lithium bromide and organic salts for absorption refrigeration machines," *Int. J. Refrig.*, vol. 29, no. 1, pp. 30–35, 2006.

[44] M. Mortazavi, R. Nasr Isfahani, S. Bigham, and S. Moghaddam, "Absorption characteristics of falling film LiBr (lithium bromide) solution over a finned structure," *Energy*, vol. 87, pp. 270–278, 2015.

[45] R. Nasr Isfahani, A. Fazeli, S. Bigham, and S. Moghaddam, "Physics of lithium bromide (LiBr) solution dewatering through vapor venting membranes," *Int. J. Multiph. Flow*, vol. 58, pp. 27–38, 2014.

[46] Y. T. Kang, H. J. Kim, and K. Il Lee, "Heat and mass transfer enhancement of nanosolutions for H2O/LiBr falling film absorption process," *Int. J. Refrig.*, vol. 31, no. 5, pp. 850–856, Aug. 2008.

[47] J. K. Lee, H. Kim, H. K. Myung, J. Koo, and Y. T. Kang, "The Effect of Additives and Nanoparticles on Falling Film Absorption Performance of Nanosolutions (H2O/LiBr + Nanoparticles)," *J. Nanosci. Nanotechnol.*, vol. 9, no. 12, pp. 7456–7460, 2009.

[48] J. K. Lee, J. Koo, H. Hong, and Y. T. Kang, "The effects of

nanoparticles on absorption heat and mass transfer performance in NH3/H2O nanosolutions," *Int. J. Refrig.*, vol. 33, no. 2, pp. 269–275, 2010.

[49] A. Sözen *et al.*, "Improving the thermal performance of diffusion absorption refrigeration system with alumina nanofluids: An experimental study," *Int. J. Refrig.*, vol. 44, pp. 73–80, 2014.

[50] G. Wang, Q. Zhang, M. Zeng, R. Xu, G. Xie, and W. Chu, "Investigation on Mass Transfer Characteristics of the Falling Film Absorption of LiBr Aqueous Solution Added with Nanoparticles," *Int. J. Refrig.*, 2018.

[51] L. Yang, K. Du, S. Bao, and Y. Wu, "Investigations of selection of nanofluid applied to the ammonia absorption refrigeration system," *Int. J. Refrig.*, vol. 35, no. 8, pp. 2248–2260, 2012.

[52] R. Gulati *et al.*, "Enhancing the efficiency of absorption refrigeration cycle by 'seeding' nanoparticles directly in the working fluid," *Int. J. Environ. Stud.*, vol. 70, no. 5, pp. 808–823, 2013.

[53] S. J. Hong, E. Hihara, and C. Dang, "Novel absorption refrigeration system with a hollow fiber membrane- based generator," *Int. J. Refrig.*, vol. 67, pp. 418–432, 2016.

[54] S. Kulankara and K. E. Herold, "Surface tension of aqueous lithium bromide with heat / mass transfer enhancement additives : the effect of additive vapor transport Tension superficielle du bromure de lithium en pre d ' additifs augmentant le transfert de chaleur et de masse : ´ mentaire," vol. 25, pp. 383–389, 2002.

[55] C. Wenlong, C. Zeshao, A. Akisawa, P. Hu, and T. Kashiwagi, “Theoretical and experimental study on surface tension and dynamic surface tension of aqueous lithium bromide and water with additive,” *Sci. China (Series E)*, vol. 46, no. 2, 2003.

[56] V. E. Nakoryakov, N. I. Grigoryeva, N. S. Bufetov, and R. A. Dekhtyar, “Heat and mass transfer intensification at steam absorption by surfactant additives,” *Int. J. Heat Mass Transf.*, vol. 51, no. 21–22, pp. 5175–5181, 2008.

[57] H. Daiguji, E. Hihara, and T. Saito, “Mechanism of absorption enhancement by surfactant,” *Int. J. Heat Mass Transf.*, vol. 40, no. 8, pp. 1743–1752, 1997.

[58] Y. T. Kang and J.-K. Kim, “Comparisons of Mechanical and Chemical Treatments and Nano Technologies for Absorption Applications,” *HVAC&R Res.*, vol. 12, no. December, pp. 807–819, 2006.

[59] S. U. S. Choi and J. A. Eastman, “ENHANCING THERMAL CONDUCTIVITY OF FLUIDS WITH NANOPARTICLES,” *ASME International Mechanical Engineering Congress & Exposition*, 1995. [Online]. Available: http://www.osti.gov/scitech/biblio/196525/.

[60] C. Pang, J. W. Lee, and Y. T. Kang, “Review on combined heat and mass transfer characteristics in nanofluids,” *Int. J. Therm. Sci.*, vol. 87, pp. 49–67, Jan. 2015.

[61] S. S. Ashrafmansouri and M. Nasr Esfahany, “Mass transfer in nanofluids: A review,” *Int. J. Therm. Sci.*, vol. 82, no. 1, pp. 84–90, 2014.

[62] H. Kim, J. Jeong, and Y. T. Kang, “Heat and mass transfer enhancement for falling film absorption process by SiO2 nanosolutions,” *Int. J. Refrig.*, vol. 35, no. 3, pp. 645–651, 2012.

[63] A. Behfar, Z. Shen, J. Lau, and Y. Yu, “Heat and mass transfer enhancement potential on falling film absorbers for water-LiBr mixtures via a literature review (RP-1462),” *HVAC&R Res.*, vol. 20, no. 5, pp. 570–580, 2014.

[64] P. Phelan, T. Otanicar, R. Taylor, and H. Tyagi, “Trends and Opportunities in Direct-Absorption Solar Thermal Collectors,” *J. Therm. Sci. Eng. Appl.*, vol. 5, no. 2, p. 21003, 2013.

[65] NanoComposix, “UV/VIS/IR SPECTROSCOPY ANALYSIS OF NANOPARTICLES,” 2012. [Online]. Available: http://cdn.shopify.com/s/files/1/0257/8237/files/nanoComposix_Guidelines_for_UV-vis_Analysis.pdf?13692. [Accessed: 04-Jul-2018].

[66] H. K. Gupta, G. Das Agrawal, and J. Mathur, “An experimental investigation of a low temperature Al2O3-H2O nanofluid based direct absorption solar collector,” *Sol. Energy*, vol. 118, pp. 390–396, 2015.

[67] Z. Deng *et al.*, “The emergence of solar thermal utilization: solar-driven steam generation,” *J. Mater. Chem. A*, vol. 5, no. 17, pp. 7691–7709, 2017.

[68] A. Lenert and E. N. Wang, “Optimization of nanofluid volumetric receivers for solar thermal energy conversion,” *Sol. Energy*, vol. 86, no. 1, pp. 253–265, 2012.

[69] J. E. Minardi and H. N. Chuang, “Performance of a ‘black’ liquid flat-

plate solar collector," *Sol. Energy*, vol. 17, no. 3, pp. 179–183, 1975.

[70] N. Arai, Y. Itaya, and M. Hasatani, "Development of a 'volume heat-trap' type solar collector using a fine-particle semitransparent liquid suspension (FPSS) as a heat vehicle and heat storage medium Unsteady, one-dimensional heat transfer in a horizontal FPSS layer heated by thermal radiatio," *Sol. Energy*, vol. 32, no. 1, pp. 49–56, 1984.

[71] R. Bertocchi, J. Karni, and A. Kribus, "Experimental evaluation of a non-isothermal high temperature solar particle receiver," *Energy*, vol. 29, no. 5, pp. 687–700, 2004.

[72] T. P. Otanicar, P. E. Phelan, and J. S. Golden, "Optical properties of liquids for direct absorption solar thermal energy systems," *Sol. Energy*, vol. 83, no. 7, pp. 969–977, 2009.

[73] E. Sani *et al.*, "Carbon nanohorns-based nanofluids as direct sunlight absorbers," *Opt. Express*, vol. 18, no. 5, pp. 5179–5187, 2010.

[74] E. Sani *et al.*, "Potential of carbon nanohorn-based suspensions for solar thermal collectors," *Sol. Energy Mater. Sol. Cells*, vol. 95, no. 11, pp. 2994–3000, 2011.

[75] L. Mercatelli *et al.*, "Absorption and scattering properties of carbon nanohorn-based nanofluids for direct sunlight absorbers," *Nanoscale Res. Lett.*, vol. 6, no. 1, p. 282, 2011.

[76] R. A. Taylor, P. E. Phelan, T. P. Otanicar, R. Adrian, and R. Prasher, "Nanofluid optical property characterization: towards efficient direct absorption solar collectors.," *Nanoscale Res. Lett.*, vol. 6, no. 1, p.

225, 2011.

[77] H. Zhang, H.-J. J. Chen, X. Du, and D. Wen, “Photothermal conversion characteristics of gold nanoparticle dispersions,” *Sol. Energy*, vol. 100, pp. 141–147, 2014.

[78] C. A. Gueymard, “The sun’s total and spectral irradiance for solar energy applications and solar radiation models,” *Sol. Energy*, vol. 76, no. 4, pp. 423–453, 2004.

[79] E. P. Bandarra Filho, O. S. H. Mendoza, C. L. L. Beicker, A. Menezes, and D. Wen, “Experimental investigation of a silver nanoparticle-based direct absorption solar thermal system,” *Energy Convers. Manag.*, vol. 84, pp. 261–267, 2014.

[80] J. Jeon, S. Park, and B. J. Lee, “Analysis on the performance of a flat-plate volumetric solar collector using blended plasmonic nanofluid,” *Sol. Energy*, vol. 132, pp. 247–256, 2016.

[81] J. R. Cole and N. J. Halas, “Optimized plasmonic nanoparticle distributions for solar spectrum harvesting,” *Appl. Phys. Lett.*, vol. 89, no. 15, pp. 2004–2007, 2006.

[82] B. J. Lee, K. Park, T. Walsh, and L. Xu, “Radiative Heat Transfer Analysis in Plasmonic Nanofluids for Direct Solar Thermal Absorption,” *J. Sol. Energy Eng.*, vol. 134, no. May 2012, pp. 1–6, 2012.

[83] J. Jeon, S. Park, and B. J. Lee, “Optical property of blended plasmonic nanofluid based on gold nanorods,” *Opt. Express*, vol. 22, no. S4, p. A1101, 2014.

[84] Q. He, S. Wang, S. Zeng, and Z. Zheng, “Experimental investigation

on photothermal properties of nanofluids for direct absorption solar thermal energy systems," *Energy Convers. Manag.*, vol. 73, pp. 150–157, 2013.

[85] M. Chen, Y. He, J. Zhu, Y. Shuai, B. Jiang, and Y. Huang, "An experimental investigation on sunlight absorption characteristics of silver nanofluids," *Sol. Energy*, vol. 115, pp. 85–94, 2015.

[86] T. Yousefi, F. Veysi, E. Shojaeizadeh, and S. Zinadini, "An experimental investigation on the effect of Al 2 O 3–H 2 O nanofluid on the efficiency of flat-plate solar collectors," *Renew. Energy*, vol. 39, no. 1, pp. 293–298, 2012.

[87] J. Qu, M. Tian, X. Han, R. Zhang, and Q. Wang, "Photo-thermal conversion characteristics of MWCNT-H2O nanofluids for direct solar thermal energy absorption applications," *Appl. Therm. Eng.*, vol. 124, pp. 486–493, 2017.

[88] H. Jin, G. Lin, L. Bai, A. Zeiny, D. Wen, and D. W. Haichuan Jin, Guiping Lin, Lizhan Bai, Aimen Zeiny, "Steam generation in a nanoparticle-based solar receiver," *Nano Energy*, vol. 28, no. August, pp. 397–406, 2016.

[89] H. Jin, G. Lin, L. Bai, M. Amjad, E. P. Bandarra Filho, and D. Wen, "Photothermal conversion efficiency of nanofluids: An experimental and numerical study," *Sol. Energy*, vol. 139, pp. 278–289, 2016.

[90] A. Polman, "Solar steam nanobubbles," *ACS Nano*, vol. 7, no. 1, pp. 15–18, 2013.

[91] O. Neumann, A. S. Urban, J. Day, S. Lal, P. Nordlander, and N. J.

Halas, “Solar Vapor Generation Enabled by Nanoparticles,” *ACS Nano*, vol. 7, no. 1, pp. 42–49, Jan. 2012.

[92] O. Neumann *et al.*, “Compact solar autoclave based on steam generation using broadband light-harvesting nanoparticles,” *Proc Natl Acad Sci U S A*, vol. 110, no. 29, pp. 11677–11681, 2013.

[93] P. Phelan, R. Taylor, R. Adrian, R. Prasher, and T. Otanicar, “Light-Induced Energy Conversion in Liquid Nanoparticle Suspensions,” in *Nanoparticle Heat Transfer and Fluid Flow*, W. J. Minkowycz, E. M. Sparrow, and J. P. Abraham, Eds. CRC(Taylor & Francis), 2012, pp. 123–142.

[94] S. V. Boriskina, H. Ghasemi, and G. Chen, “Plasmonic materials for energy: From physics to applications,” *Mater. Today*, vol. 16, no. 10, pp. 375–386, 2013.

[95] G. Baffou, J. Polleux, H. Rigneault, and S. Monneret, “Super-heating and micro-bubble generation around plasmonic nanoparticles under cw illumination,” *J. Phys. Chem. C*, vol. 118, no. 9, pp. 4890–4898, 2014.

[96] O. Neumann *et al.*, “Nanoparticle-mediated, light-induced phase separations,” *Nano Lett.*, vol. 15, no. 12, pp. 7880–7885, 2015.

[97] Z. Fang *et al.*, “Evolution of light-induced vapor generation at a liquid-immersed metallic nanoparticle,” *Nano Lett.*, vol. 13, no. 4, pp. 1736–1742, Apr. 2013.

[98] M. Amjad *et al.*, “Volumetric solar heating and steam generation via gold nanofluids,” *Appl. Energy*, vol. 206, no. March, pp. 393–400, Nov.

2017.

[99] Y. Fu *et al.*, “Investigation on enhancing effects of Au nanoparticles on solar steam generation in graphene oxide nanofluids,” *Appl. Therm. Eng.*, vol. 114, pp. 961–968, 2017.

[100] L. Zhou *et al.*, “Self-assembly of highly efficient, broadband plasmonic absorbers for solar steam generation,” *Sci. Adv.*, vol. 2, no. 4, pp. e1501227–e1501227, Apr. 2016.

[101] K. Bae, G. Kang, S. K. Cho, W. Park, K. Kim, and W. J. Padilla, “Flexible thin-film black gold membranes with ultrabroadband plasmonic nanofocusing for efficient solar vapour generation.,” *Nat. Commun.*, vol. 6, p. 10103, 2015.

[102] P. Atkins and J. de Paula, “Optical Spectroscopy and Photobiology,” in *Physical Chemistry for the Life Sciences*, 2nd ed., Oxford University Press, 2006.

[103] P. Atkins, J. de Paula, and R. Friedman, “Electronic Spectroscopy,” in *Quanta, Matter, and Change: A molecular approach to physical chemistry*, W. H. Freeman and Company, 2009.

[104] V. Khullar *et al.*, “Solar Energy Harvesting Using Nanofluids-Based Concentrating Solar Collector,” *J. Nanotechnol. Eng. Med.*, vol. 3, no. 3, p. 031003, 2013.

[105] H.-J. Chen and D. Wen, “Ultrasonic-aided fabrication of gold nanofluids.,” *Nanoscale Res. Lett.*, vol. 6, no. 1, p. 198, 2011.

[106] R. R. Retamal Marín, F. Babick, and M. Stintz, “Ultrasonic dispersion of nanostructured materials with probe sonication − practical aspects

of sample preparation," *Powder Technol.*, vol. 318, pp. 451–458, 2017.

[107] T. F. Tadros, *An Introduction to Surfactants*. Berlin: De Gruyter, 2014.

[108] S. Abbott, *Surfactant Science : Principles and Practice*. 2015.

[109] A. Kusters and M. Smith, "Ultrasonic fragmentation powders," *Chem. Eng.*, vol. 48, no. 24, pp. 4119–4127, 1993.

[110] M. A. Montenegro, M. L. Boiero, L. Valle, and C. D. Borsarelli, "Gum Arabic: More Than an Edible Emulsifier," in *Products and Applications of Biopolymers*, C. J. R. Verbeek, Ed. InTech, 2012.

[111] W. Baomin, H. Yu, S. Kai, and Z. Tingting, "The Use of Anionic Gum Arabic as a Dispersant for Multi-Walled Carbon Nanotubes in an Aqueous Solution," *Nanosci. Nanotechnol.*, vol. 12, no. 6, pp. 4664–4669, 2012.

[112] A. Indhuja, K. S. Suganthi, S. Manikandan, and K. S. Rajan, "Viscosity and thermal conductivity of dispersions of gum arabic capped MWCNT in water: Influence of MWCNT concentration and temperature," *J. Taiwan Inst. Chem. Eng.*, vol. 44, no. 3, pp. 474–479, 2013.

[113] S. Boncel, A. Zniszczoł, M. Pawlyta, K. Labisz, and G. Dzido, "Heat transfer nanofluid based on curly ultra-long multi-wall carbon nanotubes," *Heat Mass Transf. und Stoffuebertragung*, vol. 54, no. 2, pp. 333–339, 2018.

[114] R. Bandyopadhyaya, E. Nativ-Roth, O. Regev, and R. Yerushalmi-Rozen, "Stabilization of Individual Carbon Nanotubes in Aqueous Solutions," *Nano Lett.*, vol. 2, no. 1, pp. 25–28, 2002.

[115] X. Huang, Y. Kakuda, and W. Cui, "Hydrocolloids in emulsions:

particle size distribution and interfacial activity," *Food Hydrocoll.*, vol. 15, no. 4–6, pp. 533–542, Jul. 2001.

[116] Malvern Instrument limited, "What is zeta potential?" [Online]. Available: c:%5CProgram Files (x86)%5CMalvern Instruments%5CZetasizer Software%5CHelp%5CContent%5CIntroduction%5CWhat_is_Zeta_potential.htm. [Accessed: 23-Apr-2018].

[117] Z. Haddad, C. Abid, H. F. Oztop, and A. Mataoui, "A review on how the researchers prepare their nanofluids," *Int. J. Therm. Sci.*, vol. 76, pp. 168–189, 2014.

[118] A. Ghadimi, R. Saidur, and H. S. C. Metselaar, "A review of nanofluid stability properties and characterization in stationary conditions," *Int. J. Heat Mass Transf.*, vol. 54, no. 17–18, pp. 4051–4068, 2011.

[119] P. Keblinski, D. G. Cahill, A. Bodapati, C. R. Sullivan, and T. A. Taton, "Limits of localized heating by electromagnetically excited nanoparticles," *J. Appl. Phys.*, vol. 100, no. 5, pp. 11–16, 2006.

[120] S. Zhou and R. Ni, "Measurement of the specific heat capacity of water-based Al~ 2O~ 3 nanofluid," *Appl. Phys. Lett.*, vol. 92, no. 9, p. 93123, 2008.

[121] H. Zhang, H.-J. Chen, X. Du, G. Lin, and D. Wen, "Dependence of Photothermal Conversion Characteristics on Different Nanoparticle Dispersions," *J. Nanosci. Nanotechnol.*, vol. 15, no. 4, pp. 3055–3060, 2015.

[122] W. M. Rohsenow, J. P. Hartnett, and Y. I. Cho, *Handbook of Heat*

Transfer, 3rd ed. McGraw-Hill, 1998.

[123] J. M. Wimby and T. S. Berntsson, “Viscosity and density of aqueous solutions of lithium bromide, lithium chloride, zinc bromide, calcium chloride and lithium nitrate. 1. Single salt solutions,” *J. Chem. Eng. Data*, vol. 39, no. 1, pp. 68–72, 1994.

[124] P. C. Mishra, S. Mukherjee, S. K. Nayak, and A. Panda, “A brief review on viscosity of nanofluids,” *Int. Nano Lett.*, vol. 4, no. 4, pp. 109–120, 2014.

[125] J. Jeong, C. Li, Y. Kwon, J. Lee, S. H. Kim, and R. Yun, “Particle shape effect on the viscosity and thermal conductivity of ZnO nanofluids,” *Int. J. Refrig.*, vol. 36, no. 8, pp. 2233–2241, 2013.

[126] S. Turner, “Brownian motion & Brownian motors.” [Online]. Available: https://www.youtube.com/watch?v=LqVeBxtZbj0. [Accessed: 01-Aug-2018].

[127] A. Sayigh, Ed., *Solar Air Conditioning and Refrigeration*. 1992.

[128] W. P. Jones, “Vapour Absorption Refrigeration,” in *Air Conditioning Engineering*, 2001, pp. 399–410.